INCLUSIVE PRODUCTION CROSS SECTIONS FOR PROTON–LIKE PARTICLES FROM 0.8 GeV/n La + La COLLISIONS

By

Yves Michel Xavier Marie Dardenne

A DISSERTATION

Submitted to
Michigan State University
in partial fulfillment of the requirements
for the Degree of

DOCTOR OF PHILOSOPHY

Department of Chemistry

1992

ABSTRACT

INCLUSIVE PRODUCTION CROSS SECTIONS FOR PROTON–LIKE PARTICLES FROM 0.8 GeV/n La + La COLLISIONS

By

Yves Michel Xavier Marie Dardenne

There is a discrepancy between a variety of theoretical models (VUU, BUU, Cascade, QMD, and others) and experimental results in the inclusive production cross sections of proton–like particles (^{1}H, ^{2}H, ^{3}H, ^{3}He, and ^{4}He) at 20° polar lab angle for 0.76 GeV/n La + La collisions. The goal of this work is to check the previous experimental results. This was done using a small acceptance magnetic spectrometer. The 20° cross sections were determined by measuring the back angles, and using kinematic transformations. This was done in order to make the measurements as independent as possible from the previously measured cross sections. Cross sections have been determined at 60° and 40° from 0.25 GeV/c to 2.0 GeV/c, and the 20° cross sections from 0.9 GeV/c to 1.5 GeV/c.

The original experimental results were confirmed. At large polar angles the theory agrees with the data; however, even after taking into account the energy loss of the beam, the discrepancy at small polar angles is still present, although it is greatly reduced.

DEDICATION

In the name of all who have worked with the Vax 750 Janus computer, I wish to dedicate this thesis to that valiant computer. It gave its life in the line of duty.

ACKNOWLEDGEMENTS

There is a slew of folks that deserve my gratitude for their help. I will try to enumerate them as best as I can, if there is an omission it is purely due to my lack of memory and I apologize.

I would like to thank Jim Bistirlich, Roy Bossingham, and Aaron Chacon, for they have brunted the major amount of my questions and inquiries. Without the many useful discussions and appropriate ridicule at silly questions, I would have had a rather nasty time finishing this thesis.

I thank my committee members, Dr A.Galonsky, Dr K.Hunt, Dr M.Kanatzidis, Dr W.McHarris, and Dr J.Rasmussen. These people are forced to wade through this thesis, and this is no easy task. Two of the above mentioned folks, Dr W.McHarris and Dr J.Rasmussen were in charge of guiding me, and this is also not an easy task. I thank them for their continual support.

In order to perform the experiment for this thesis, several weeks of extensive work to get ready are required. Once the experiments is going a 24 hour watch must be maintained for several days. The following folks pulled 8–10 hour shifts during those weeks and days (in alphabetical order), Jim Bistirlich, Roy Bossingham, Helmet Bossy, Tom Case, Aaron Chacon, Ken Crowe, John Rasmussen, Adnan Shihad-eldin, and Mark Stoyer.

I wish to thank Dr Ken Crowe and Dr John Rasmussen for allowing me to work with their group here at LBL.

In order to perform the experiment, the back scintillators had to be rebuilt from scratch. Two people went out of their way to help me rebuild the back array, Don Jordan and Corry Lee. These two are very thorough and meticulous, I thank them

for their help. I also have to thank them for teaching me the game of cribbage which I am now addicted to.

Throughout my thesis quite a variety of people have financially supported me and I am grateful for this. They are (in alphabetical order) Associated Western Universities Inc, whose director is Norman Orava, K. Crowe, W. McHarris, and J. Rasmussen.

Other people I would like to acknowledge for various thing are Wade Olivier and Wen–tse Chou for their patience in my initial training; Jack Miller for a couple of very useful discussions; the EOS group, here at LBL, for allowing me to use their computing facilities.

A few folks have read through the very first drafts of my thesis, and these very patient people have my gratitude for their useful comments. These folks are (in alphabetical order) D. Armstrong, R. Bossingham, A. Chacon, W. McHarris, J. Rasmussen, and C. Tull.

My mother and brother have had a lot to do with what I have become, and I thank them for all the support that was given through the many many years.

I want to thank my wife for her love and affection, which I never met an equal.

Finally, I would like to thank the tax payers for financing this experiment through their generous forced contributions we call taxes.

Contents

List of Tables

List of Figures

Chapter I

Introduction

People have been trying to study the properties of nuclear matter for a long time (see for example [Naga81]). Even the basics of nuclear matter, such as at what densities nuclear matter is a gas, a fluid, or a solid are not well known . What is the entropy of these phases? Are these the only phases possible? (Water has at least four different forms of ice.) Also at what temperatures do these phases occur? How is temperature defined for nuclear matter?

The purpose of experiments such as this one is to decipher the equation of state of nuclear matter. The "equation of state" refers to the properties of nuclear matter such as the relationship between density and temperature. These properties can be determined by colliding heavy nuclei and, depending on the energy at which these collisions occur, states of various density and temperature are produced.

This deciphering of the equation of state is being performed in many laboratories around the world simultaneously on both experimental and theoretical fronts. Quite a variety of theoretical models have been proposed to date. One way to test them is by comparison with experimental results. If the theoretical model is capable of reproducing the experimental data, it means that the physics that is occurring during these heavy-ion nuclear collisions is understood. However, if there are discrepancies,

then in all likelihood it means that some physics is going on which is not being accounted for. Such discrepancies are usually where new things are discovered.

At present various theoretical models (such as Cascade, VUU, BUU, RVU, and QMD) agree rather well with one another but disagree with experimental results [Aich89]. The discrepancies involve the production cross sections of proton–like (p–like) particles at different lab angles as a function of momentum for 0.8 GeV/n La on La collisions. Proton–like particles refers to ^{1}H, ^{2}H, ^{3}H, ^{3}He, and ^{4}He, which are the predominant fragments emerging from the above collisions. Production cross sections as a function of angle and momentum refer to the phase–space distribution of p–like particles with specific angle and momentum. An easier way to think of these cross sections is as the probability of producing p–like particles having a specific angle and momentum in the lab frame. Figure I.1 shows the comparison and the discrepancy between the theoretical calculations and the experimental results. The data (solid dots) were obtained by Hayashi *et al* [Haya88], and the theory curves come from several sources [Aich89].

The discrepancies are most notable for the top curve (20°). The figure is drawn on a log scale, so we are looking at discrepancies up to a factors of two. It is important to resolve them because some of these models are being used to calculate effects that occur at the few percent level. If they have such large problems predicting something basic like inclusive cross sections, then their other predictions very likely will be in serious error. The fact that such a variety of theoretical models, all with varying assumptions, agree is significant. As a result, some people thought that the problem might lie in the experimental data. Thus, the primary motivation for the present research is to check on the accuracy of the previous experimental work.

Some of the above theories do not incorporate coalescence into their models. In these cases the final products are free nucleons, and no complex nuclei such as deu-

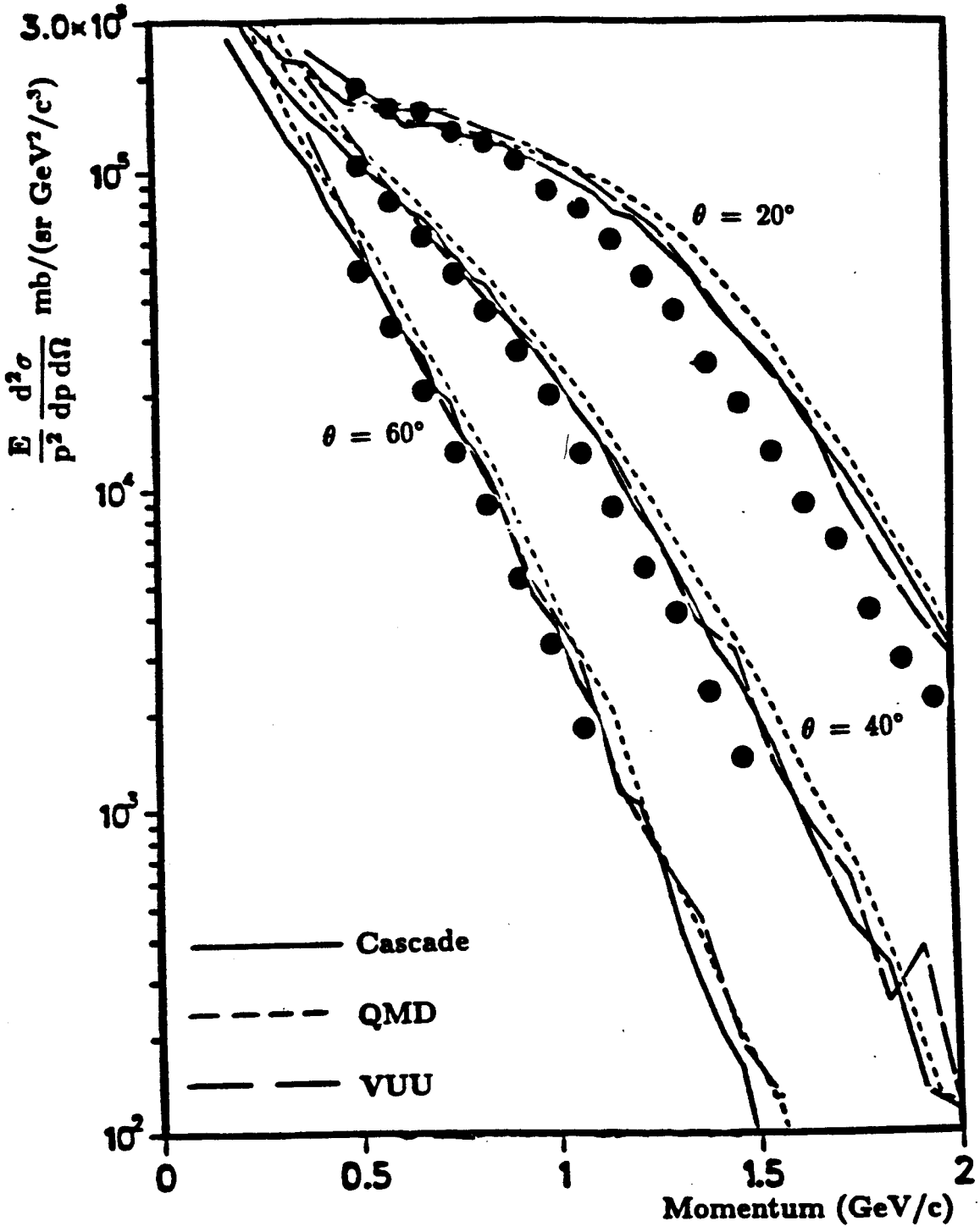

Figure I.1: Comparison of theoretical models with experimental data for invariant cross sections of p–like particles at three polar angles for 0.8 GeV/n La on La collisions.

terium, tritium, and so on. In order to be able to compare the various theories with experimental results, one has to sum over all the protons produced, regardless of whether they are free or combined in complex nuclei. Actually, one should also take into account heavier fragments such as lithium, but the probability of producing such heavy fragments is so small that the final result is not significantly affected by ignoring their existence. Details of the calculation of the p–like cross sections are presented in Chapters II and VI.

Chapter II

Theory

A Introduction

This chapter contains a brief introduction to some of the models used in Figure I.1. However, calculation of p–like cross section is slightly convoluted because the models in question are mostly interested in things such as charge flow from nuclear collisions. Thus, any coalescence effects are ignored. This means that the number of protons produced according to one of these models is larger than the number of free protons produced during the real collisions, because in the real collisions the fragments such as helium will contain bound protons, which in the theoretical model are produced as free protons.

An introduction to the coalescence model is needed in order to understand why the effects of coalescence can be ignored on the energy scale of this experiment.

B Basic Coalescence Model

The coalescence model predicts that, when two nucleons (protons and neutrons) come within a coalescence radius (p_o), they will bind into more complex fragments, such as deuterons, tritium, and so on. The coalescence radius is a function of the relative momentum of the nucleons. This means that if the momentum difference between,

for example, a proton and a neutron is small enough, they will be able to coalesce into some complex nucleus, namely a deuteron.

It has been observed ([Jaca85], [Lema79], [Gutb76], [Butl63], [Schw63]) that there is a scaling law between the proton cross sections and the composite fragment cross sections. This relationship is

$$E_A \left[\frac{d^3\sigma_A}{dp_A^3}\right] = C_A \left[E_p \left(\frac{d^3\sigma_p}{dp_p^3}\right)\right]^A, \tag{II.1}$$

where $E\left[\frac{d^3\sigma}{dp^3}\right]$ is the Lorentz invariant cross section. Whether the subscript is A or p refers to whether the cross section is that of a composite fragment of mass number A or simply for protons. C_A is an empirical scaling factor.

From the scaling factor one can calculate the coalescence radius [Jaca85] to be

$$p_o^3 = \left(\frac{3m\sigma_o}{4\pi}\right)\left(C_A \left[\frac{Z_t + Z_p}{N_t + N_p}\right]^N A^2\, N!\, Z!\right)^{\frac{1}{A-1}}, \tag{II.2}$$

where N, N_t, and N_p are the fragment, target, and projectile neutron numbers, respectively; Z, Z_t, and Z_p are the fragment, target, and projectile proton numbers; m is the nucleon rest mass, and σ_o is the geometric reaction cross section with r_o = 1.2 fm, this being the radius of a nucleon. There are more refinements which have been added, such as taking into account the spin of the particles and also predicting source sizes.

An average value for p_o seems to be around 150 MeV/c, where c is the speed of light. The process of a proton and a neutron coalescing into a deuteron with a final momentum of 1 GeV will have a 7% effect on the initial momentum. This will be an isotropic effect, so the overall charge flow will not be effected, which is the reason some of the theoretical models which are going to be reviewed do not consider

coalescence effects.

There is a good review article on microscopic models by G. Bertsch and S. Das Gupta [Bert88]. A large portion of the following discussion on these models is drawn from this article. Another thing which should be mentioned is that all of the following models use Monte Carlo simulations (Appendix A).

C Cascade Model

The first of these models and perhaps the most intuitive is the Cascade model. It was the first strictly microscopic model, meaning that it treats each nucleon in the nucleus separately. In the model each nucleus is a collection of nucleons within a sphere. This early model contained no nucleon–nucleon interactions, meaning that no fermi momentum could be assigned to the individual nucleons. In a real nucleus, in the ground state the nucleons inside the nucleus have momentum. If any of this momentum were assigned to any of the nucleons, the nucleus would just break apart, because there is no nucleon–nucleon interaction to hold it together.

The purpose of the Cascade model is mainly to specify the position and time of particle collisions. This is done by dividing the collision into small time intervals of δt, which is chosen so that the probability of more than one interactions is small; a $\delta t = 0.5$ fm/c (1.67×10^{-24} sec) is often used, where c is the speed of light.

Using Monte Carlo simulations (Appendix A), one can determine whether two particles will collide. If there is a collision, the Monte Carlo simulation chooses the impact parameter. It can choose whether the collision is elastic or inelastic. With an inelastic collision there is a possibility of producing $\Delta(1232)$ particles, which will decay into pions (π) and baryons. The angle of scattering and the final momentum are Monte Carlo decisions. In order to obtain results which will look like the data,

one needs to propagate many of these interactions through each δt simultaneously. Small volumes can be defined, and after each δt step the density of particles in these volumes can be calculated. Variables such as entropy and temperature can also be pulled out. This model was reasonably good at predicting cross sections to within a factor of 2–3.

D Cascade Model with Mean Field

One of the deeper improvements made to the Cascade model was to add a mean field, which is a potential term which will be explained in the next few paragraphs. This is where theories such as Boltzmann–Uehling–Uhlenbeck (BUU), Vlasov–Uehling–Uhlenbeck (VUU), Relativistic–Vlasov–Uehling (RVU), and Quantum Molecular Dynamic (QMD) arise [Aich89]. They all use the same general equation:

$$\begin{aligned}\frac{\partial f}{\partial t} + v\cdot\nabla_r f - \nabla_r U\cdot\nabla_p f \;=\; & -\frac{1}{(2\pi)^6}\int d^3p_2\, d^3p_{2'}\, d\Omega\, \frac{d\sigma}{d\Omega}\, v_{12} \\ & \times [f_1 f_2(1-f_{1'})(1-f_{2'}) - f_{1'}f_{2'}(1-f_1)(1-f_2)] \\ & \times (2\pi)^3\,\delta^3(p + p_2 - p_{1'} - p_{2'})\ . \qquad \text{(II.3)}\end{aligned}$$

Here $f(r,p,t)$ is the function which describes the position and momentum of the individual particle as time progresses.

The left side of equation II.3 when set equal to 0 is called the Vlasov equation. It can be derived starting from creation and annihilation operators [Bert88]. The left side of equation II.3 is the semiclassical version of the time–dependent Schrodinger equation with a potential term added (U); thus, this part of the equation takes into account the propagation of the particle. The potential term is density dependent; its functional form is

$$U(\rho) = A\left(\frac{\rho}{\rho_o}\right) + B\left(\frac{\rho}{\rho_o}\right)^{\alpha}\ , \qquad \text{(II.4)}$$

where ρ_o is the normal nuclear density, ρ is the density at the time of sampling, and A, B, and α are adjustable parameters. A and B are attractive and repulsive terms, respectively, and α is related to the compressibility of nuclear matter. A high value of α (e.g., 2) is considered a hard collision, meaning that the matter is incompressible, while a low value of α (e.g., 1) is a soft collision.

Various theories have differing values for A, B, and α. However, the potential curve as a function of ρ/ρ_o is well known from nucleon–nucleus scattering experiments for low values of ρ/ρ_o (0.5–1). This means that, no matter what values are chosen for A, B, and α, the resulting curve has to follow at least the beginning of the potential curve. These theories really start to diverge from one another at ρ/ρ_o of 1.5. In this experiment, densities higher than 1.5 times that of nuclear densities are not reached [Jian91], so the differing values of A, B, and α in the individual theories do not really effect the results.

The right side of equation II.3 is called the collision integral. This part of the equation takes into account the interactions in a collision. f_1, f_2, $f_{1'}$, and $f_{2'}$ are the states of two particles before and after the collision: before the collision the two particles are described by f_1 and f_2, and afterward by $f_{1'}$ and $f_{2'}$. The cross sections for going from f_1 to $f_{1'}$ and f_2 to $f_{2'}$ in a collision are described by the $d\Omega \frac{d\sigma}{d\Omega} v_{12}$ term. These cross sections are model–dependent; this is a variable which changes depending on the theory. Finally, the $(1 - f)$ terms take into account Pauli blocking: in a collision some states are going to be occupied, so these states will not be available for other particles.

One of the above mentioned models does differ from all the other models in one thing: QMD has coalescence built into it. When all the particles have been propagated through the δt intervals, it tests for clumps of nucleons which under the right conditions (spin, momentum, etc.) could coalesce, so this model does produce com-

plex nuclei.

This roughly describes the general equation used by the various models. The interesting thing to notice is that even with all the various assumptions each of these models has, they seem to agree rather well among themselves when predicting inclusive production cross sections (Figure I.1) at these energies.

E Cross Section Predictions

As can be seen, there is no inherent coalescence built into the above mentioned models, except for QMD. Thus, if one wishes to perform a comparison between theory and experiment, a middle ground must be found, so, the cross section is calculated using

$$E\,\frac{d^3\sigma_{inc}}{dp^3} = \sum_i^n Z_i\,A_i^2\,E_i\,\frac{d^3\sigma_i}{dp_i^3}\ , \qquad \text{(II.5)}$$

where σ_{inc} is the inclusive p–like production cross section, Z and A are the fragment charge and mass number, and $E\,\frac{d^3\sigma}{dp^3}$ is the Lorentz invariant cross section. The advantage of defining the cross section this way is that it is independent of the frame for which one is calculating it. Finally, the whole thing is summed over all fragment types. In this experiment the heaviest fragment dealt with is ^{4}He. It is not completely obvious as to how equation II.5 takes into account all protons. (The Z and A^2 are required because we are measuring p–like particles.) This is more extensively discussed in Chapter VI.

Chapter III

Experiment

A Introduction

The experiment consisted of 0.757 GeV/n ^{139}La on ^{nat}La collisions. The experiment was done using the Bevalac accelerator at the Lawrence Berkeley Laboratory (LBL). The beam rate was about 10^7 particles per spill with one spill every six seconds. The lanthanum target used was 0.5 gm/cm^2 thick, and the experiment ran for approximately 96 hours.

The purpose of this experiment was to determine the inclusive production cross sections for proton–like particles which come out of such collisions at various angles. It was especially important to make this measurement at 20° polar lab angle because this is where the largest discrepancy lies between theory and the previous experiment (Figure I.1).

Since the object was to measure the number of particles of various types, it was necessary to design a spectrometer which would be able to distinguish the particles from one another and also measure the momentum of each particle. The five particles that are of importance are protons (^{1}H), deuterons (^{2}H), tritium (^{3}H), helium 3 (^{3}He) and alphas (^{4}He), since the contribution of Li and heavier elements to the cross sections are expected to be negligible. In order to separate particle types, four pieces

of data are needed: rate of energy loss, rigidity, time of flight, and path length. First, an explanation of each of these is necessary:

- Rate of energy loss $\Rightarrow$ The energy the particle loses per unit thickness in a plastic scintillator.
- Rigidity $\Rightarrow$ An inverse measure of the deflection of a charged particle when traversing a magnetic field:

$$R = \frac{\gamma m v}{Z} = \frac{p}{Z} , \qquad \text{(III.1)}$$

where m is the mass of the particle, Z its charge, v its velocity, and $\gamma = 1/\sqrt{1 - \frac{v^2}{c^2}}$. A high velocity particle will have a high rigidity and will not bend much in a magnetic field.

- Path length $\Rightarrow$ The length of the path of the particle through the spectrometer.

- Time of flight (TOF) $\Rightarrow$ The time it took to traverse the path length.

How do these four values help to distinguish the particles from one another? Equation III.1 can be simplified; because of the small acceptance of the spectrometer, the path lengths of most particles are nearly equal. Thus, equation III.1 can be approximated as $R \propto 1/TOF$. Therefore, plotting R vs TOF (Figure III.1) gives a plot which separates particles by their m/Z values (Figure III.1 has been produced using a Monte Carlo simulation, as explained in Appendix A). In this way all the particles can be distinguished, except for ^{2}H and ^{4}He, since their m/Z is effectively the same. Also shown in Figure III.1 are positively charged pions. These particles do not enter into the calculation of the cross sections, but they will be detected in the experiment; thus, they were also simulated.

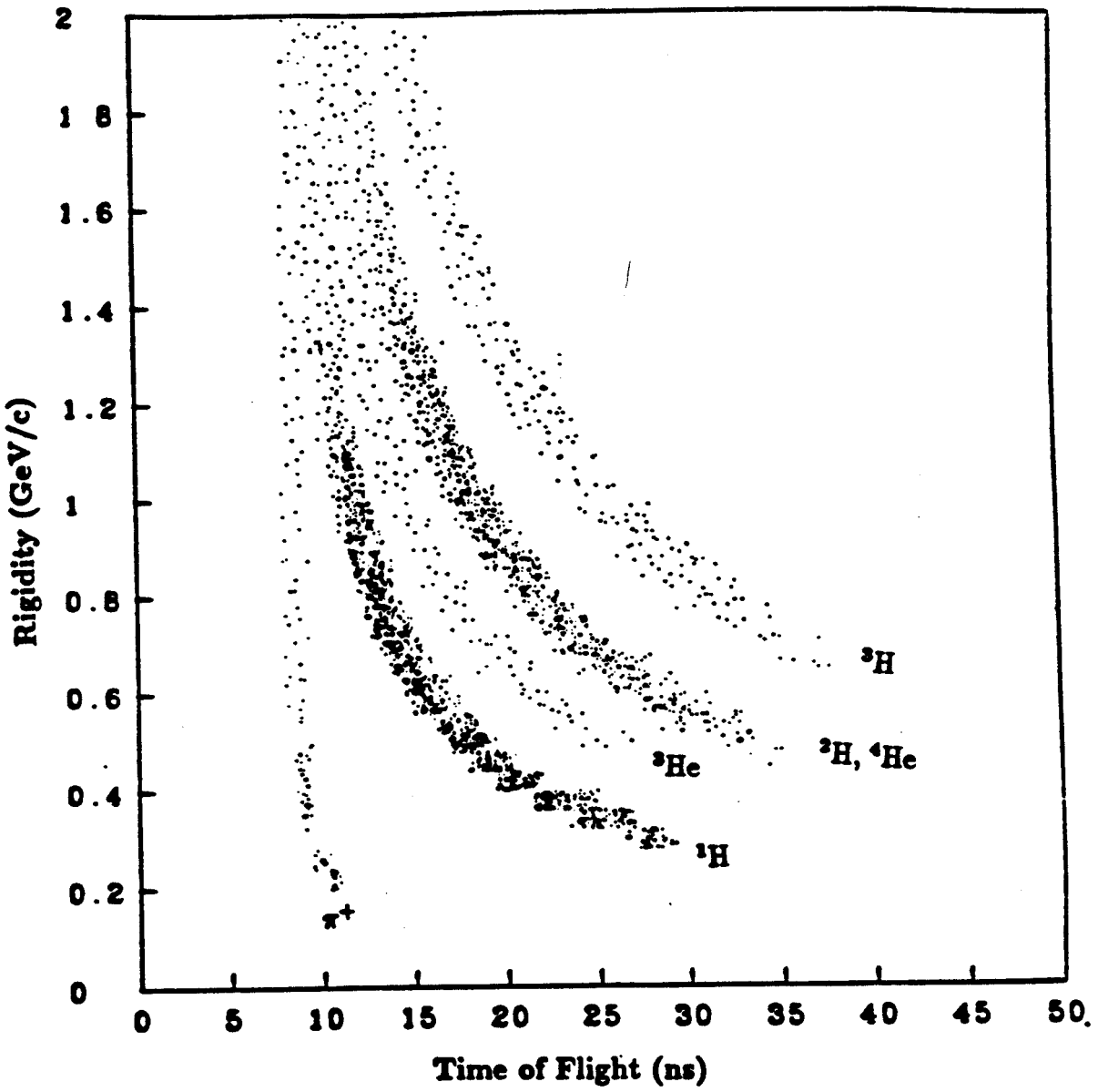

Figure III.1: Monte Carlo data showing the separation of particles obtained by plotting rigidity vs time of flight.

Energy loss is then used to separate ^{2}H and ^{4}He. The Bethe–Bloch equation ([Part92], [Fano63]) describes quantitatively the energy loss of relativistic particles as they pass through a material,

$$\frac{dE}{dx} = \frac{DZ_{med}}{A_{med}} \left(\frac{Z}{\beta}\right)^2 \left[ln\left(\frac{2m_e\gamma^2\beta^2c^2}{I}\right) - \beta^2 - \frac{\delta}{2}\right]. \qquad \text{(III.2)}$$

The equation has quite a few terms; however, the factor of interest is

$$\frac{dE}{dx} \propto \left(\frac{Z}{\beta}\right)^2. \qquad \text{(III.3)}$$

Here dE/dx is energy loss per unit length, Z is the charge, and β is v/c. Combining equations III.1 and III.3,

$$\frac{dE}{dx} \propto \left(\frac{m}{R}\right)^2. \qquad \text{(III.4)}$$

This means that a plot of dE/dx vs. R (Figure III.2) (again this figure was produced using Monte Carlo data) would produce a separation caused by the mass difference between various particles. As can be seen in Figure III.2, ^{2}H and ^{4}He are well separated; however, ^{3}H and ^{3}He have almost equal masses and are not well separated. Again, pions are also detected and simulated.

Using a combination of Figures III.1 and III.2, it should be possible to separate all five particle types.

The goal is thus to design a spectrometer which will allow the determination of three variables (time of flight, rigidity, and energy loss). To this end the Janus spectrometer was set up (Figure III.3).

B Spectrometer

As each part of the spectrometer is described, its purpose will be explained. All the parts which will be mentioned can be found in Figure III.3.

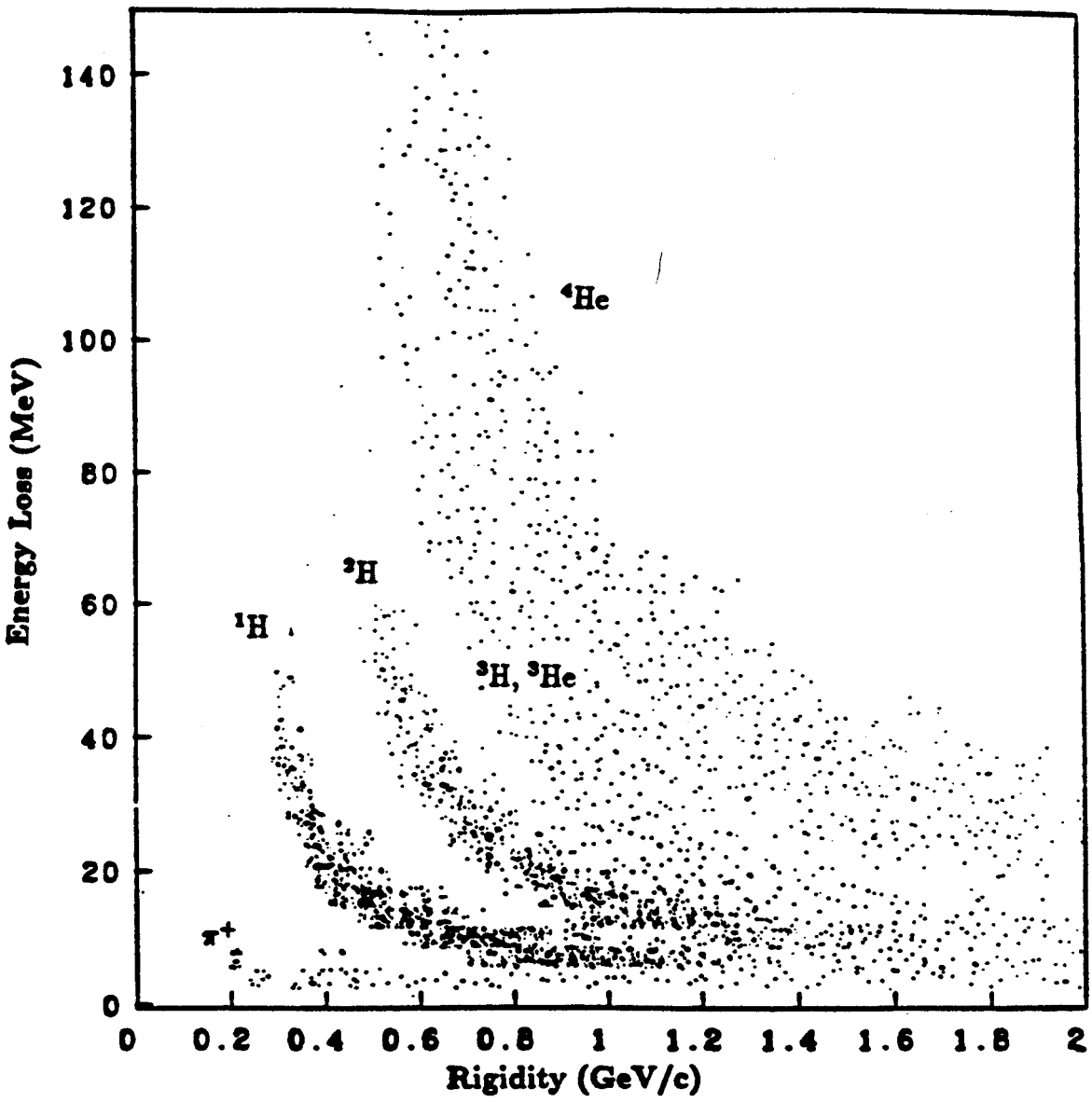

Figure III.2: Monte Carlo data showing the separation of particles obtained by plotting energy loss vs rigidity.

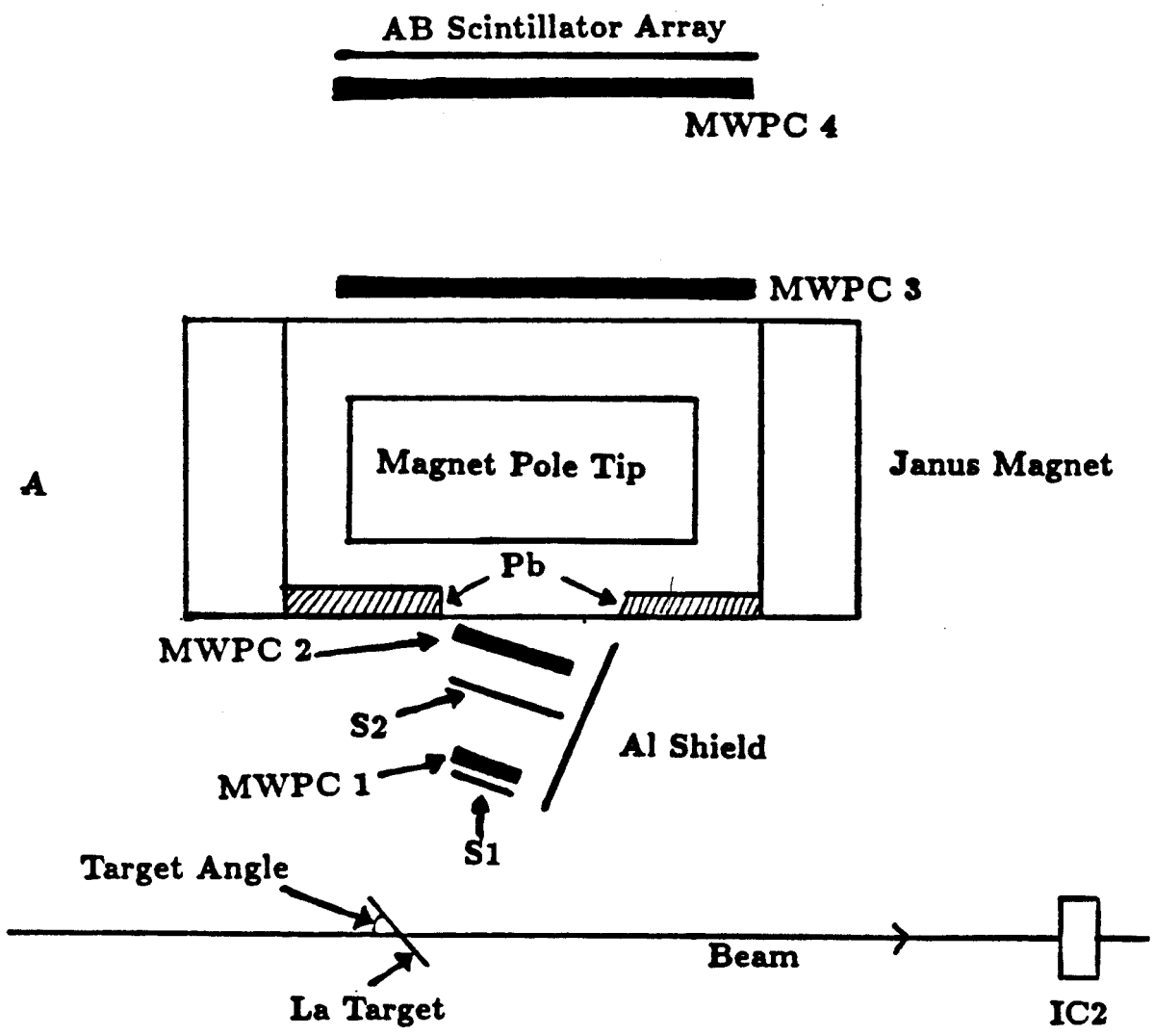

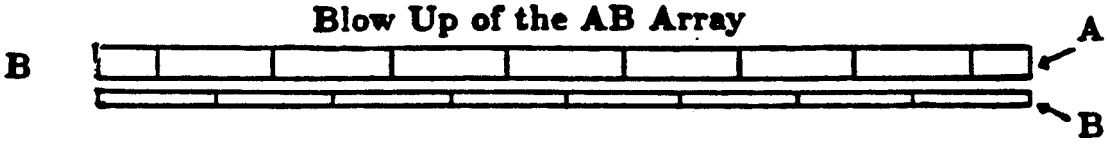

Figure III.3: A) The Janus spectrometer. B) Blow-up of the AB scintillating array.

1 The Janus Magnet

The Janus magnet is a dipole magnet with a pole–tip size of 167.6 cm by 55.9 cm and a pole gap of 21.4 cm. During the experiment the magnetic field was set at 7 kG. The deflection that is observed, due to the charged particle crossing the field, is related to the momentum of the particle. The quantitative determination of rigidity will be described later.

2 Scintillation Counters

In Figure III.3 there are quite a few scintillators. Nearest the target are S1 and S2, and behind the magnet the AB array, all with various purposes. Because they have different purposes, the sizes of the scintillators are important. The scintillators are made of a plastic commercially called NE 102A.

S1 is 1.5 mm thick, 15.2 cm high, and 30.6 cm wide. S2 is 1.5 mm thick, 20 cm high, and 56.1 cm wide. Both S1 and S2 were equipped with XP2020 photomultiplier tubes, which have high count–rate capabilities. S1 and S2 each can handle up to 10^6 events per second.

The A part of the AB array comes in two widths, 25.4 cm and 12.7 cm (see the blow up of the AB array in Figure III.3B), with seven of the first width and two of the second. The narrow A scintillators were placed at each edge of the array in order to create a staggering between the A and the B scintillators. The A and B thickness are 0.64 cm and 0.32 cm, respectively. The B scintillators are all 25.4 cm wide. Both the A and the B scintillators are 31.1 cm high.

The time of flight is the time it takes for the particle to travel from S1 or S2 to the AB array. Thus, as soon as a signal is seen in S1 and S2, a clock is started; when a signal is seen at the AB scintillators, that clock is stopped. The digitized value that

is obtained from this is provided by a time–to–digital converter (TDC). The TDC is an electronic module (LeCroy 2228A) which accumulates a constant current onto a capacitor. The charge on the capacitor will be proportional to the length of time it was left to charge. Thus, the charge that is recorded from the TDC is proportional to time. Each AB scintillator segment has its own TDC module.

The AB array has two functions: The first, just mentioned, is to stop the TDC clock. The second is to measure the energy loss of a particle as it passes through the A array, this being the reason the A array is so thick. The signal that is observed comes from an analog–to–digital converter (ADC). The ADC is an electronic module (LeCroy 2249A), and it also works using a capacitor, which accumulates the current which comes from the photomultiplier tubes. The current from the phototubes is related to the light output produced from the particle that passed through the scintillating plastic. This, in turn, is related to the energy loss in the scintillator. The energy loss in the scintillator has to be in a correct range. If the energy loss is too low then the electrons are not exited to the correct energy levels and the deexcitation is thermal, but if there is too much energy loss, the deexcitation occurs through the breakdown of molecular bonds in the plastic.

S1 and S2 are used primarily to produce a start on the TDC. Since this will be accomplished with a signal of almost any size above the noise level, it is to our advantage to make both of these scintillators very thin, minimizing scattering and energy loss.

3 Multiwire Proportional Chambers (MWPC)

The dimensions and details of the three–plane wire chambers (from now on abbreviated MWPC) are as follows: MWPC 1 has an area of 30.5 cm by 15.25 cm. Its first plane is angled at 45°, the second plane at 90° (vertical), and the third at 0°

(horizontal). MWPC 2 is 57.6 cm by 19.2 cm, with planes 1 through 3 strung at 0°, 90°, and −45°, respectively. MWPC 3 and 4 are identical, 200 cm by 25 cm with their planes are strung at −30°, 90°, and 30°. In every plane the separation between the wires is 0.2 cm. Each sense wire plane is separated from the next by a high-voltage wire plane; the separation is 0.7 cm. The gas mixture in the wire chambers goes by the name "magic gas," which consists of 70% argon, 25% isobutane, 4.5% freon, and 0.5% methyal. Wire chambers 1, 3, and 4 were read out by an LBL system, while wire chamber 2 was read out by a LeCroy PCOS3 system.

The purpose of these wire chambers is to obtain information on the position of a particle when it crosses their planes. When a particle crosses through one of the wire chambers, it will ionize the gas and create a current in a small clump of wires in each of the first, second, and third planes. Because of the angle at which each plane is strung, the intersection of all three wires forms a triangle, the center of which can be taken as the point at which the particle went through the wire chamber (Figure III.4).

The position of the particle could have been determined just as well by just using two wires; so, why the third wire plane? The problem that occurs is when two particles cross through the wire chamber simultaneously. Assume that there were only two planes and that two particles crossed this wire chamber (Figure III.5). It is ambiguous as to where the two particles crossed the wire chamber; did they go through points 1 and 3 or 2 and 4? Now compare this with the situation in which the wire chamber has three wire planes (Figure III.6). The third wire plane makes it clear that the two particles crossed at positions 1 and 3.

The positions that all four wire chambers provide will allow the determination of rigidity, path length, and certain cuts on the data which will help in the determination of the quality of the track reconstruction. These items will be explained further in

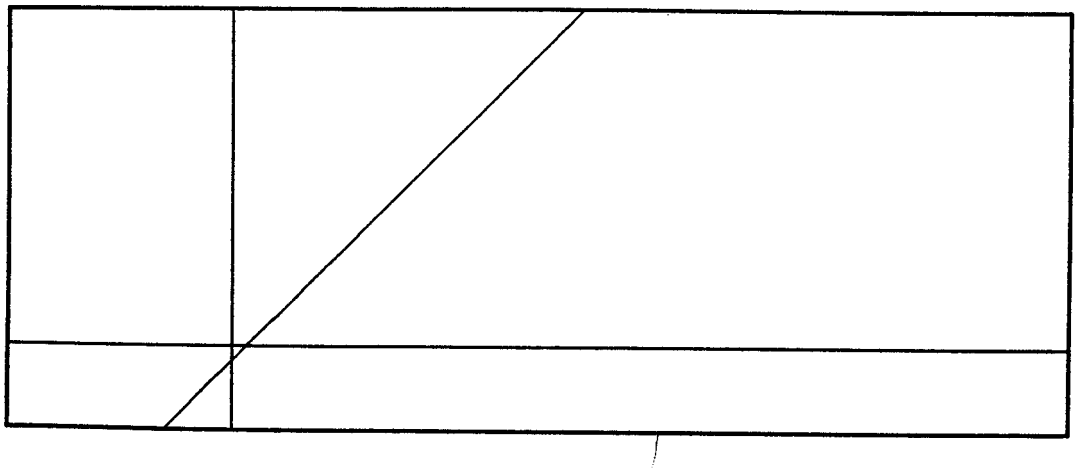

Figure III.4: A wire firing in each plane forms a triangle showing where a particle has crossed the MWPC.

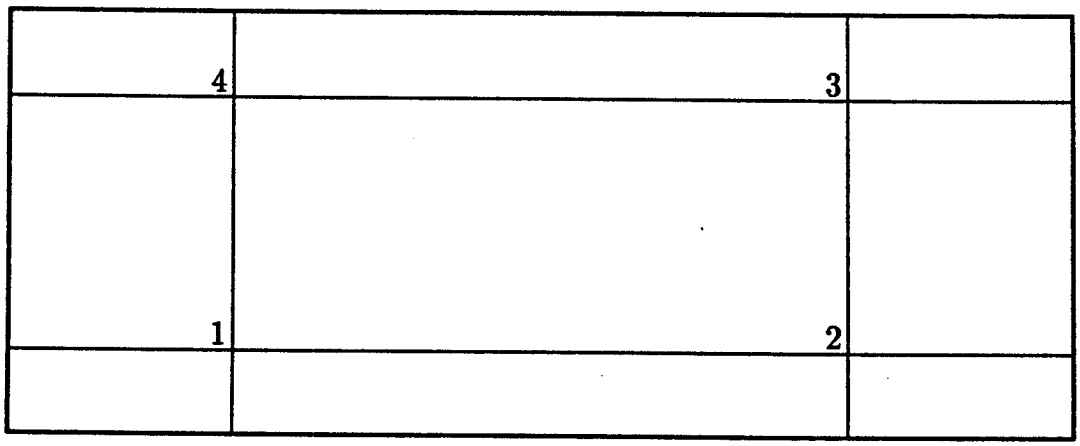

Figure III.5: The ambiguity in the positions at which two particles traverse a wire chamber with only two planes of wires.

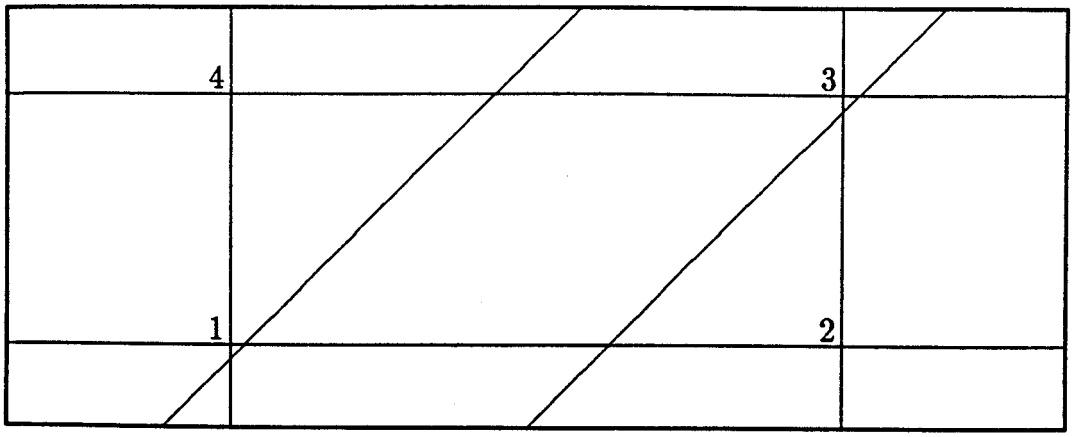

Figure III.6: The third wire plane localizes the positions of the two particle tracks.

Chapter IV.

4 Beam Monitor

To measure the cross section it is necessary to know the number of beam ions which hit the target. The beam intensity was measured using an ionization chamber (IC2), which has been used before [Zajc82]. The current from the ion chamber was read by a current integrator with a pulsed output counted by a scaler, which is proportional to the number of incident beam ions. The proportionality constant was determined by calibrating the ion chamber using a La beam of known intensity. The calibration has an error of 0.9%.

C Target Position and Spectrometer Angle

There is an interesting problem with the goal stated at the beginning of this chapter. Because of the physical constraints of the Janus spectrometer it was not possible to

place the magnet in such a position as to measure the particles coming off at 20°, which was the main goal of this experiment.

An important thing to keep in mind is that whether the angle is 20° in the target frame or the projectile frame makes no difference at all, the physics is the same. This results from the fact that the collision is a symmetric one, i.e., the projectile and the target nuclei are identical. The explanation of the measurement at 20° is going to be centered around Figure III.7. Keep in mind that this figure is just a visual representation of the Lorentz transformations.

The first thing which needs to be explained is rapidity, usually designated Y and plotted on the horizontal axis of Figure III.7. Rapidity is a variable which is used instead of velocity due to its simple additivity under Lorentz transformations. If one wishes to transform from one moving frame to another, one can just add or subtract the rapidities of each of these frames. (This is not the case for velocities, because of relativistic effects.) The equation for rapidity is

$$Y = 0.5\, ln\left[\frac{E + p_{||}c}{E - p_{||}c}\right] = tanh^{-1}\beta_{||} , \qquad \text{(III.5)}$$

where E is total energy, $p_{||}$ is the parallel component of momentum, and $\beta_{||}$ is the parallel component of β. The vertical axis of Figure III.7 is the perpendicular momentum divided by the mass of the particle. There are two thicknesses of lines in this figure. The thick lines correspond to the projectile frame, and the thin lines to the target frame.

As a start, consider the target frame (the thin lines). The lines going upward, with angles indicated at the top of them, are lines of constant lab angle, which are curved because the parallel component of the momentum has relativistic transformations. The lines perpendicular to these lines are lines of constant momentum, which are also curved because of relativistic effects. Now, consider the projectile frame (the

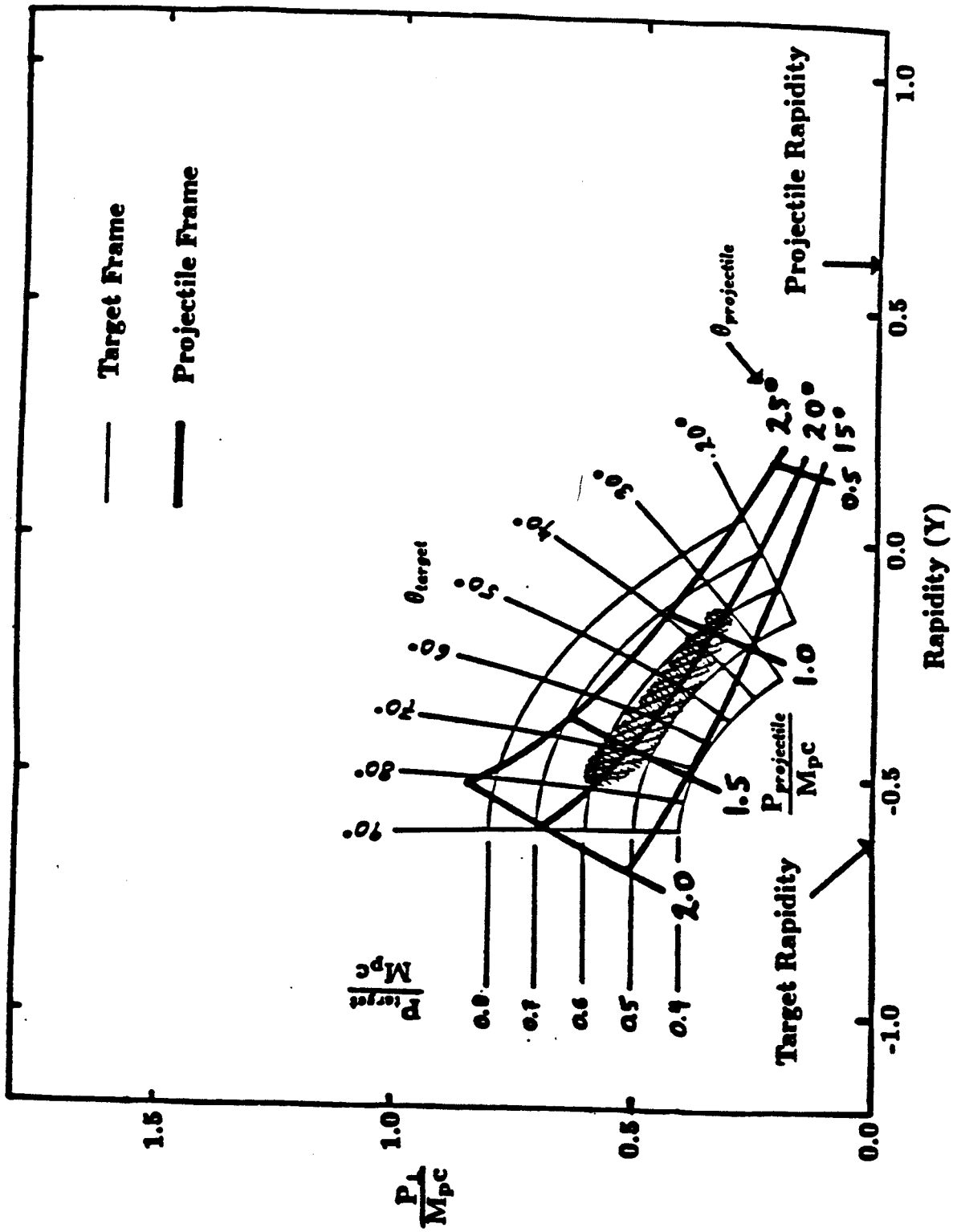

Figure III.7: Projectile to target frame transformation

thick lines). This grid has the same interpretation as the grid in the target frame. As can be seen, in the projectile frame the area of discrepancy between theory and experiment (the shaded area) at 20° is equivalent to a specific momentum and angular range in the target frame. These ranges, in the target frame, are physically possible to measure using the Janus spectrometer.

Figure III.8 shows the various combinations of magnet rotation and target position used in order to cover the momentum and angular range which are to be transposed to the 20° measurement. The first magnet–target configuration in Figure III.8 covers an angular range from 50° to 80°; roughly, the middle angle of this configuration is 65° and from now on this configuration will be referred to as the 65° configuration. The second configuration in this figure covers an angular range from 37° to 54°, its middle angle is 45°, and it will be referred to as the 45° configuration. Finally, the third configuration covers an angular range from 29° to 44°, its middle angle is 35°, and it will be referred to as the 35° configuration. These three configurations cover the range needed in Figure III.7.

By collecting data at three magnet–target configurations (Figure III.8) and using the appropriate Lorentz transformation, the p–like cross sections at 20° could be obtained.

D Trigger and Data Acquisition

A nuclear reaction will produce a multitude of fragments, which in turn will produce a very large number of electrical signals as they pass through the spectrometer. If all the signals were to be written to the computer directly, the computer disk or magnetic tape would fill up relatively fast, not to mention that the data analysis would be more complicated. It is therefore essential to set up a trigger. The trigger

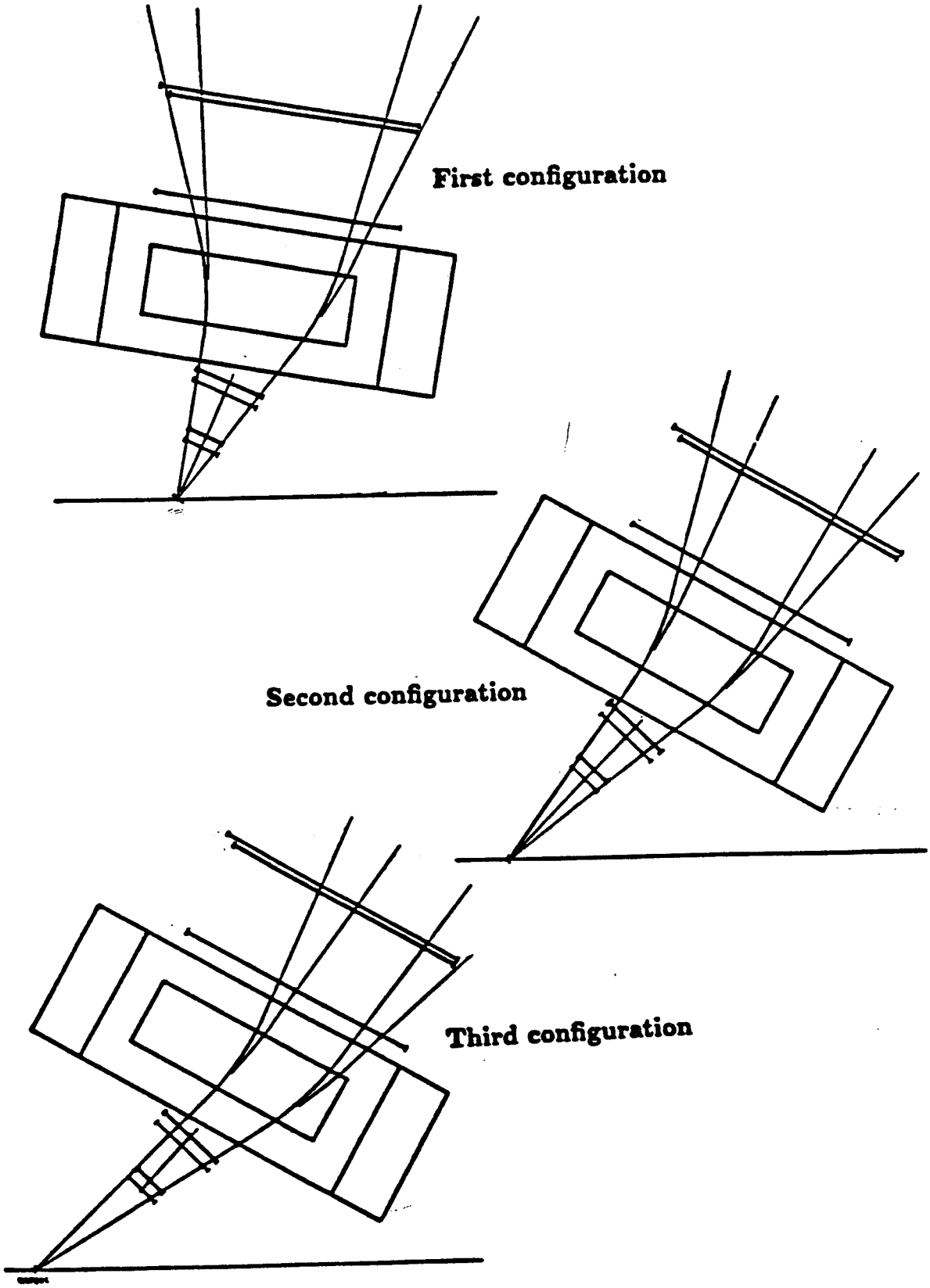

Figure III.8: Various rotations and angle positions used to cover a greater range of momentum.

is a set of conditions, which in our case is a specific sequence of electrical signals. If these conditions are met, then whatever caused the signals will be considered to be a candidate event. All of the electrical signals from this candidate are stored on magnetic tape. The conditions of the trigger will, of course, depend on what one is trying to measure. In this experiment, anything which might be a particle should be considered a candidate. Therefore, the conditions for our trigger were

$$Trigger = S * \Pi * FO\,. \tag{III.6}$$

This equation means that a simultaneous signal must be observed from each of the three components. Looking back at Figure III.3, the components correspond to the following:

$$\begin{array}{rcl} S & \Longrightarrow & S1 * S2 \text{ coincidence} \\ \Pi & \Longrightarrow & \text{signal from the } AB \text{ array} \\ FO & \Longrightarrow & \text{A signal from each of the four wire chambers} \end{array} \tag{III.7}$$

If there was a simultaneous signal from each of the above, it is likely that a particle went through the spectrometer, and the signals were then stored on magnetic tape. The data acquisition was done using a VAX-11/750, and the software used for the data acquisition was the Los Alamos Q system [Harr81].

A little bit more discussion is needed on the Fast Out (FO) electronics. Because it was not possible to reconstruct a track from the wire-chamber signals before the next set of events arrive, the Fast Out (FO) electronics were set up. The FO will fire if a set of conditions have been met by the four MWPC's. It was required that one out of three planes gave a signal for the MWPC1, three out of three for MWPC2, and two out of three for both MWPC3 and MWPC4. There is an additional requirement that all of these signals have to fall within a time gate. Again, because there is not a lot of time available, it is not possible to check if it is the incoming particle which caused

the signal. This means that the FO will fire if it receives any signals from the four wire chambers. This has repercussions for the overall efficiency of the experiment, which will be discussed in Chapter V.

E Master Gate and Run Gate Scalers

Obviously, in the electronics and in the data aquisition there is going to be some dead time. This dead time needs to be taken into account in one form or another, which is what the master gate and "run gate" are about.

There are scalers associated with both of these gates, such as the beam counter mentioned above. A scaler is nothing more then a counter. If a scaler is run gated, it means that it will accept signals continuously while the run is in progress regardless of any dead time. On the other hand if a scaler is "master gated", it will only accept signals under a specific set of conditions. The conditions are RUN, BEAM, and NOT BUSY, where RUN means that there is a run in progress, BEAM means that there is a spill coming from the Bevatron, and NOT BUSY means that the computer is free. Taking as an example the scalers for the beam monitor, the run–gated beam–counter scaler will tell us how many beam ions have gone through the target, while the master–gated beam–counter scaler will tell us how many beam ions have gone through the target during the live time of the computer. Similar scalers were set up for time, the run–gated time tells us the amount of time for the run, while the master–gate time tells us the amount of live time for the run.

When looking at beam rates (Chapter V) and calculating the final cross section (Chapter VI), whether the scaler used is run gated or master gated is very important.

F Summary

For a quick overview of the spectrometer, refer back to Figure III.3. The S1 and S2 scintillators serve to start a TDC when a particle passes through them. The AB scintillators have two purposes, to stop the TDC and to measure the energy loss of the particle. The wire chamber will give the location of the track as it goes through the spectrometer and will eventually reveal the momentum of the particle. Finally, and most importantly, the magnet, wire chambers, and scintillators are rotated to two angles and the target is placed at three positions in order to measure the appropriate momentum and angular ranges needed to obtain the 20° cross sections.

Chapter IV

Data Analysis

A Introduction

This chapter will deal with the various steps which were followed to obtain the cross sections. The following flow chart shows each major step which was performed in the analysis.

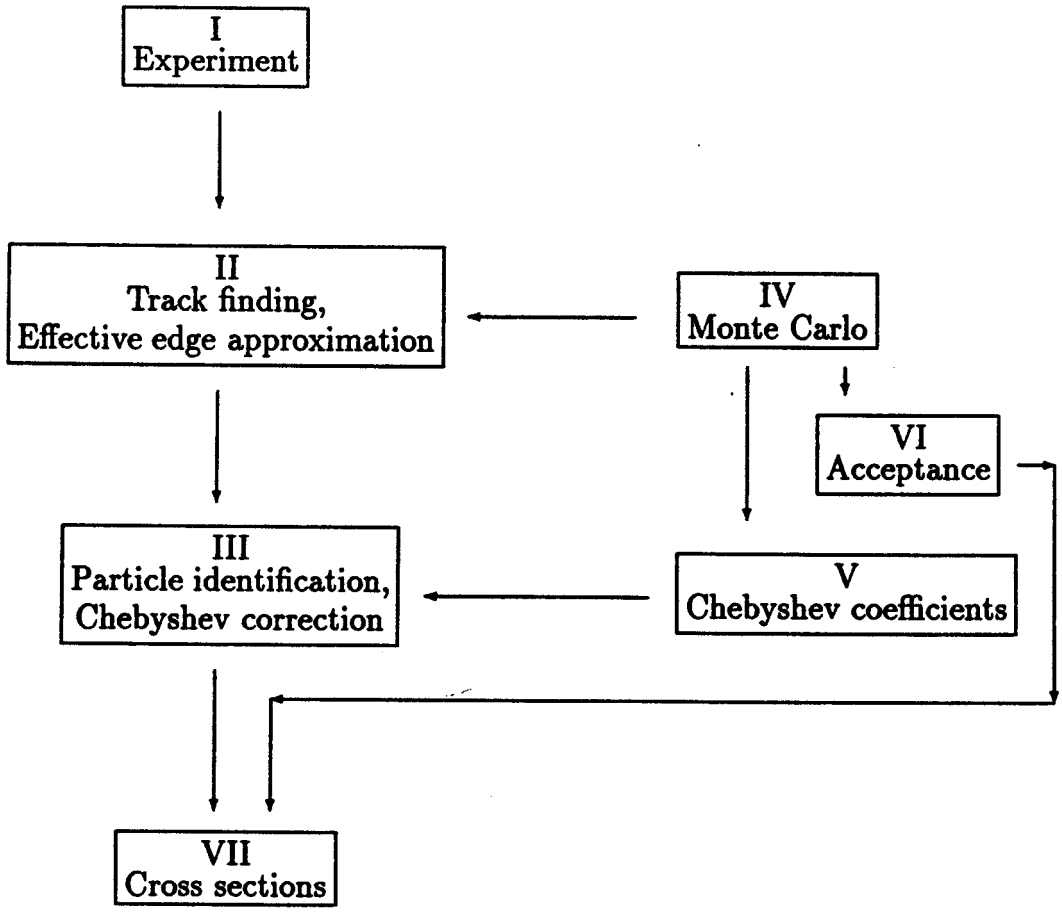

The following sections and subsections explain each part of this flow chart.

B Track Finding

This section corresponds to box II on the flow chart and deals with how tracks were reconstructed from the raw data. It is conceptually easy to think of how a track is reconstructed. From each wire chamber there is a point (or a hit) in space; from the points in MWPC 1 and MWPC 2 an in–going line into the magnet can be constructed, and from the points in MWPC 3 and MWPC 4 an out–going line can also be formed. All that is left is to construct the curvature that occurs in the magnetic field and match that curvature to the in– and out–going lines. When this is done, a track has been reconstructed. MWPC 1 will typically have up to 10 or more hits per event due to its proximity to the target. MWPC 2 will have many fewer hits because it is relatively removed from the target; however, even if it has only two hits, there are 20 possible combinations (10 in MWPC 1 times 2 in MWPC 2) to form in–going tracks. If there are only two hits in each of MWPC 3 and 4, that means there are four possible out–going tracks. Thus, there are 80 possible (20 in–going times 4 out–going) combinations of hits through the spectrometer in this example. Obviously not 80 particles have traversed the spectrometer. The problem is to get rid of the candidate tracks that are formed using the wrong matching of hits.

The next subsections will deal with the problem of matching in–going hits with out–going hits to form a track. Four parameters will be used to do the matching: target trace back, ΔR, $\Delta Z3$, and $\Delta Z4$. All of these parameters are calculated using an effective edge approximation. "Effective edge approximation" means that it is assumed that the magnetic field is constant up to a sharp edge and is zero beyond

this edge. While this is not strictly true, after a certain point the field is so weak that the approximation is not a bad one for this experiment. The accuracy of the approximation will be examined a little later.

1 Survey of the Spectrometer

Before continuing the discussion about the various parameters, it is important to know the position of the multiwire proportional chambers so that the positions of the hits can be determined.

After the experiment the spectrometer was surveyed: the position of each piece of the spectrometer was measured three times, each measurement on a different day. Also, during the experiment itself, some of the runs had the magnetic field turned off, meaning that any particle passing through the spectrometer was going through in a straight line. Thus, it is easy to predict which wires in MWPC 3 and 4 should fire if the positions of the hits in wire chambers 1 and 2 are known. The agreement between the prediction and the real hits indicated the amount by which the position of each wire chamber had to be corrected in order for the predictions and real hits to match. The correction amounted to a change of a few millimeters for each of the wire chambers.

2 Target Trace Back (TTB)

The easiest parameter to explain is the target trace back (TTB). From the survey of the spectrometer, the positions of MWPC 1, MWPC 2, and the target are known very precisely (± 0.2 cm). To make life simple let's imagine that there were only two hits in MWPC 1 and only one hit in MWPC 2. This gives two possible combinations of in-going tracks (Figure IV.1). Since the only reactions which are of interest originate in the target, the particles (or tracks) that are being sought should come from the target.

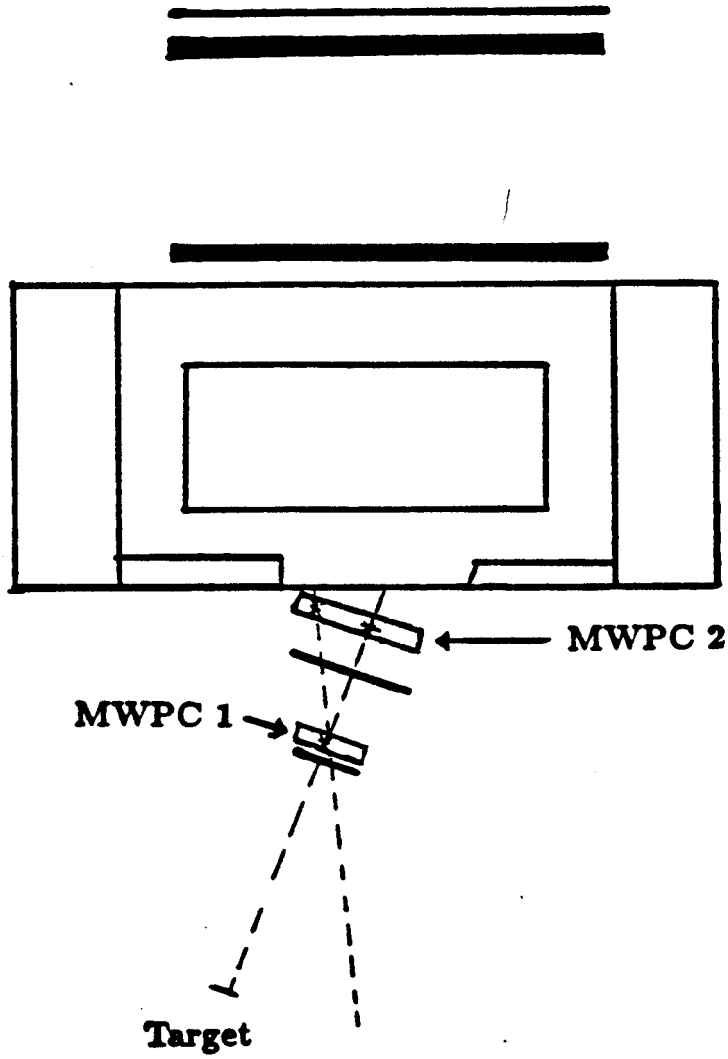

Figure IV.1: Possible tracks leading back to the target.

In Figure IV.1 only one of the two possible tracks leads back to the target; therefore, the combination which formed the other track can be discarded. Figure IV.2 shows the target trace back from a set of real data. There exist a multitude of particles which do not lead back to the center of the target. These are real particles which may have been produced from a variety of places such as beam air interaction, beam lead interaction, and beam beam–pipe interaction, or these may be particles which were produced in the beam–target interaction but scattered either in the air, scintillators, or even the wire chambers. The particles which did not come from the beam target interaction will be taken into account by subtracting out the background.

Not all our problems are solved, because of the fact that when many hits are close to one another, several of the combinations could lead back to the target. Thus, more criteria are required.

3 ΔR Cut

The next parameter is ΔR, which partly helps in choosing the right combination of hits to reconstruct a track. When a charged particle moves through the magnetic field, it will follow a circular arc. For a real track, the in–going and out–going lines are tangent to the arc at the effective edges of the field (Figure IV.3). Therefore, perpendiculars (R1 and R2 in Figure IV.3) to the in– and out–going lines at the effective edges should be along the radii of the circular arc, and the intersection point of R1 and R2 will be the center of the circle. Using the slopes of R1 and R2, plus the points at the effective edges, an equation for each line (R1 and R2) can be obtained. Then the position of the center of the arc can be calculated by solving the two equations for their intersection point. Knowing the coordinates of this point allows the calculation of the lengths of both R1 and R2. For a real track R1 should

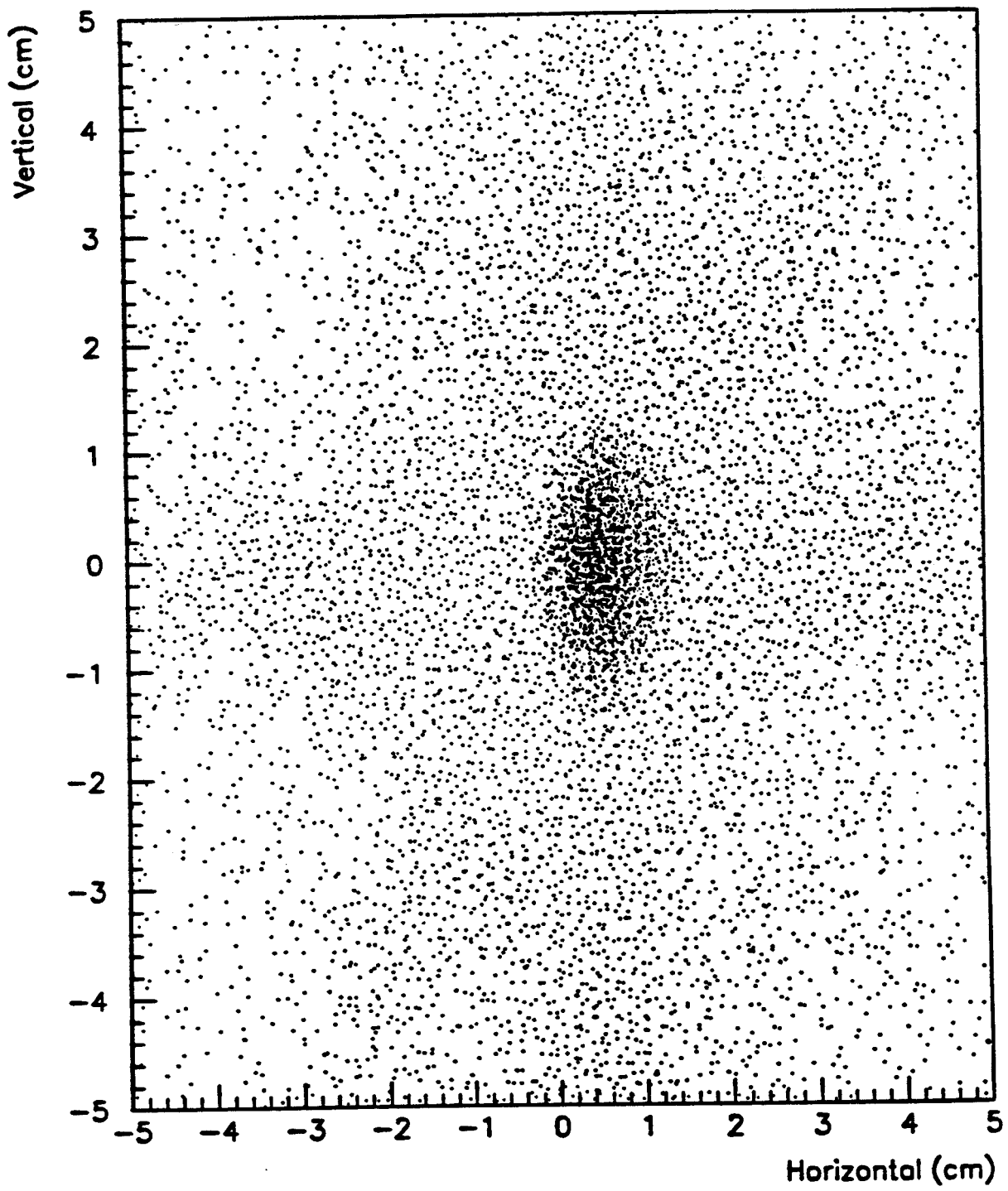

Figure IV.2: Target trace back from the real data.

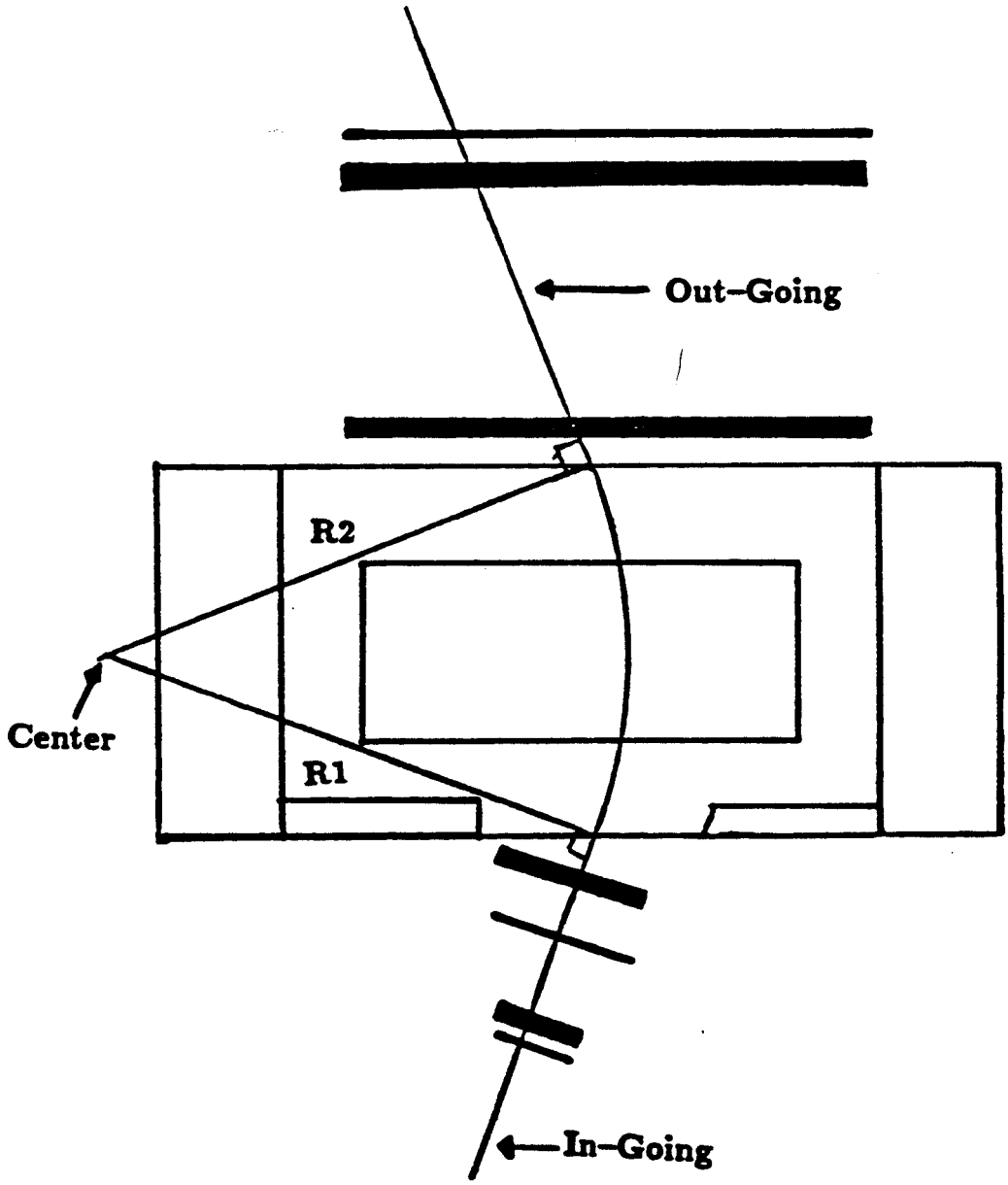

Figure IV.3: Construction of ΔR.

be essentially the same length as R2. ΔR is a measure of this:

$$\Delta R = \frac{R1}{R2} - 1. \tag{IV.1}$$

If the match between the incoming and out–going lines is a good one, ΔR will be close to zero; however, if the match is bad, ΔR will either be a large positive number or close to -1. ΔR is then multiplied by 100 in order to convert it into percent. Figure IV.4 shows two possible matchings and the ΔR which would result from each.

For a real track,

$$\Delta R = \frac{R1}{R2} - 1 \approx 0 \tag{IV.2}$$

For a false track,

$$\Delta R = \frac{R1}{R3} - 1 \text{ is a large positive number or close to } -1. \tag{IV.3}$$

It is obvious that the combination of R1 and R2 is better.

Figure IV.5 shows the ΔR distribution which is obtained from an experimental run. There seems to be a very large background, resulting from all the wrong combinations of hits which are considered to be tracks. This background will disappear once the χ^2 restriction is applied (explained in subsection 5 below)

Now there are two parameters which can be used in the track determination. However, there still is another problem: ΔR is calculated as if the track had no vertical component, which is seldom true. The up and down directions of the in–coming track into Janus are restricted by the target trace back, since the track is required to lead back to the target (Figure IV.2), After the magnet there is no parameter available to judge the up and down motion of the out–going track. This is where $\Delta Z3$ and $\Delta Z4$ come into play.

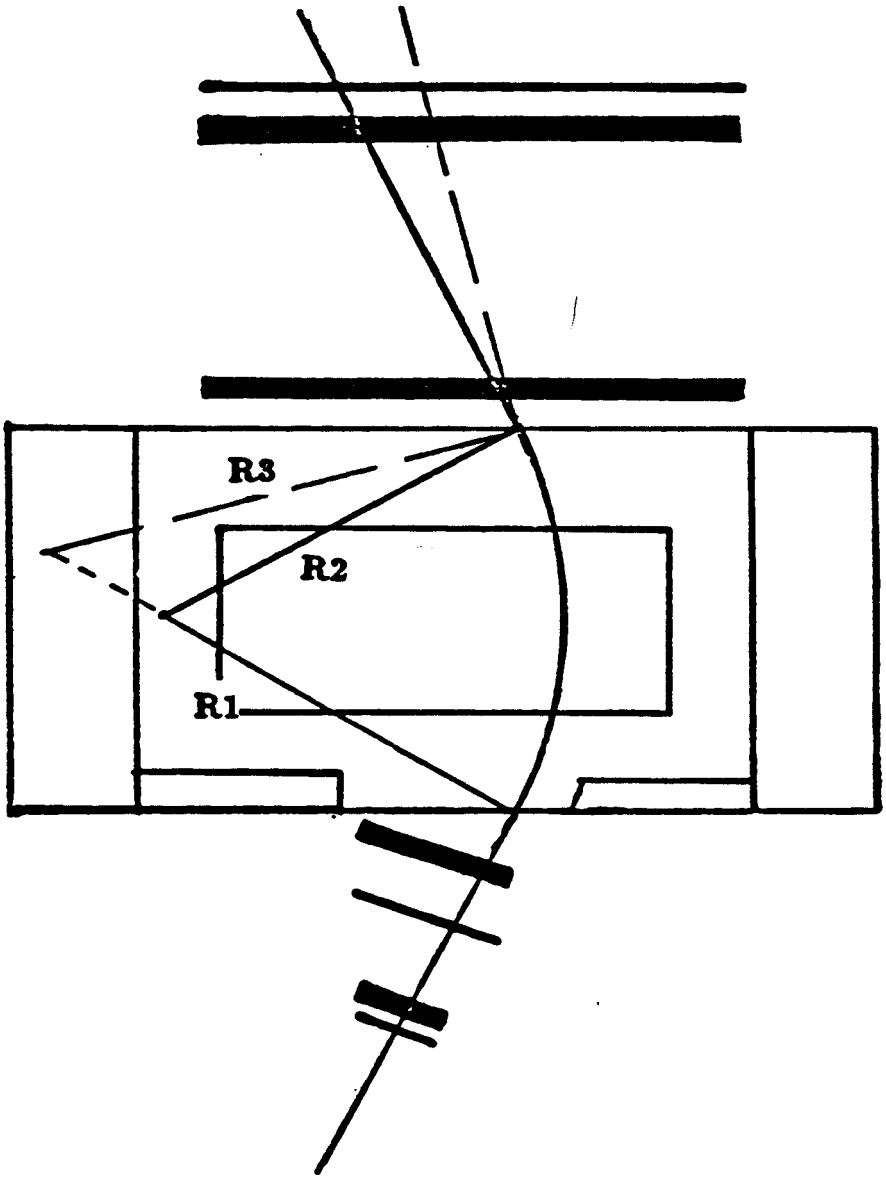

Figure IV.4: Comparison of two matches to form ΔR.

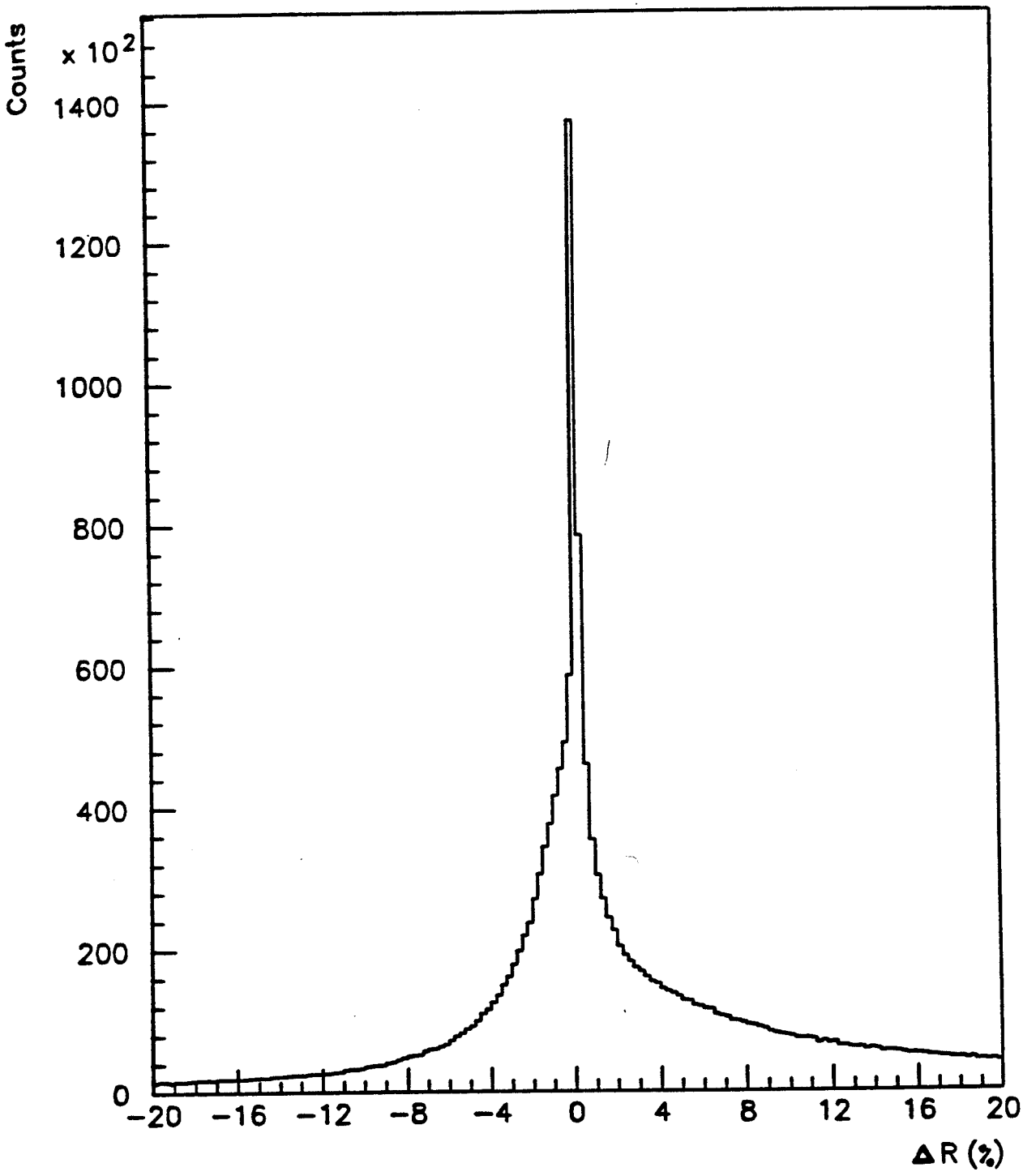

Figure IV.5: ΔR, in %

4 $\Delta Z3$ and $\Delta Z4$ Cuts

The field lines at the edge of the magnet are bowed outwards, and this focuses charged particles vertically. This effect can best be described by looking at Figure IV.6. Part A shows the B_X and B_Y components of the field; outside of the magnet the field has a B_X component. Part B shows a top view, the shaded area is where a particle will feel the B_X component of the field. Part C shows the result of the interaction with the B_X component. This is called vertical focusing. The extent of the focusing has to do with the particle's momentum and the field strength. A quantitative derivation of the amount of focusing can be done [Banf68]. Knowing the extent of the focusing, one can calculate the height at which the particle will hit MWPC 3 and 4. This is where $\Delta Z3$ and $\Delta Z4$ come into play. These two parameters are defined as follows:

$$\begin{aligned} \Delta Z3 &= Z3(calc) - Z3(expt) \\ \Delta Z4 &= Z4(calc) - Z4(expt) \end{aligned} \qquad \text{(IV.4)}$$

$\Delta Z3$ and $\Delta Z4$ are the differences between the calculated height and the experimental height in MWPC 3 and 4. Again, if the matching of hits is a good one, the differences $\Delta Z3$ and $\Delta Z4$ will be close to zero.

Figure IV.7 and IV.8 show the $\Delta Z3$ and $\Delta Z4$ distributions, which are obtained from an experimental run. Again, both the $\Delta Z3$ and $\Delta Z4$ plots contain high backgrounds, resulting from to the wrong combination of hits into tracks. This background also disappears once the χ^2 restriction is applied. As can be seen, $\Delta Z3$ and $\Delta Z4$ are useful parameters.

It should be mentioned that $\Delta Z3$ and $\Delta Z4$ are coupled. Figure IV.9 demonstrates that when the prediction for $\Delta Z3$ is bad, so is the prediction for $\Delta Z4$, and vice versa. This fact becomes important when calculating the value of the χ^2.

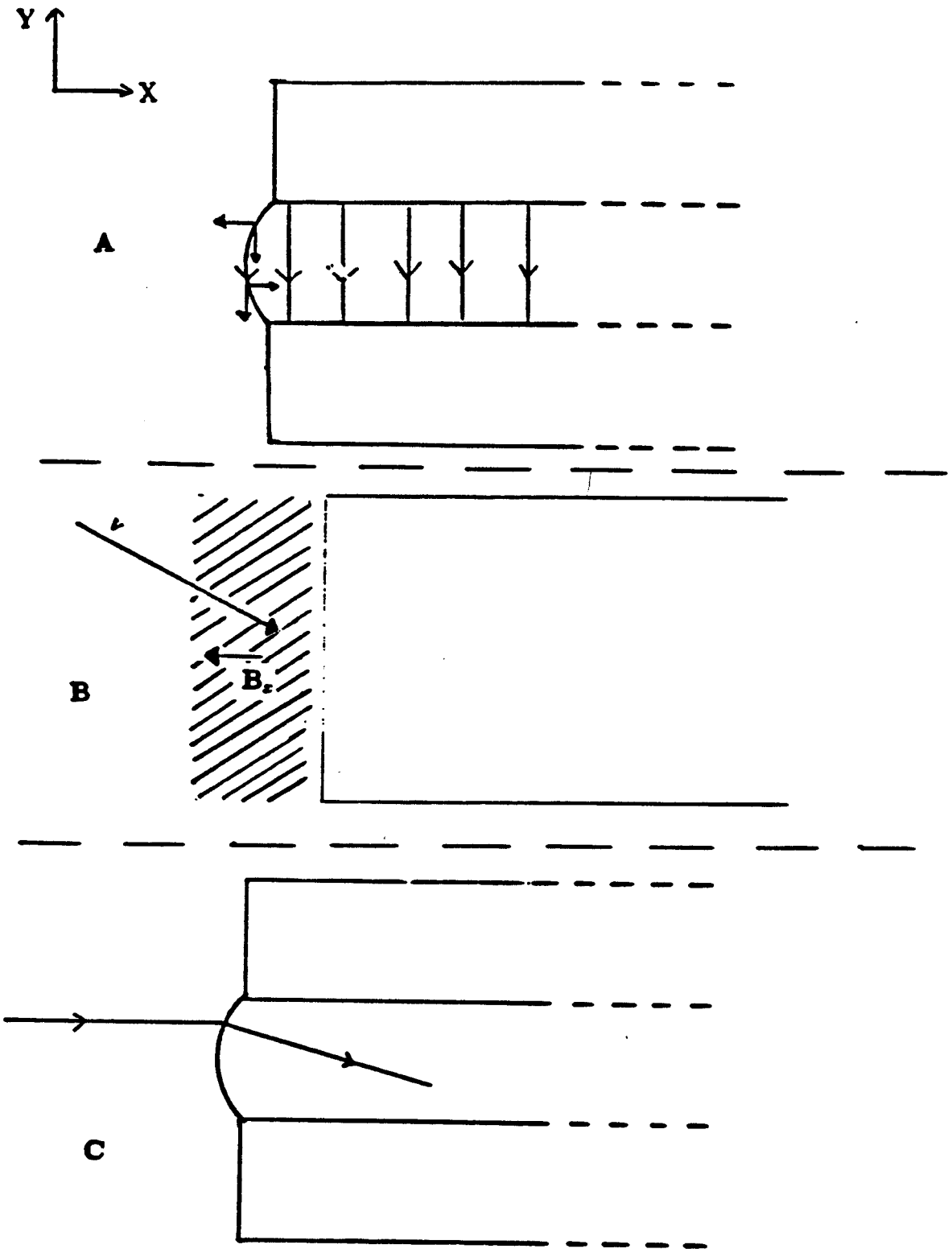

Figure IV.6: A) The X and Y components of the magnetic field, B) A top view of the magnet, the shaded area is were there is an X component to the field, and C) The effect on a particle as it crosses this part of the field (vertical focusing).

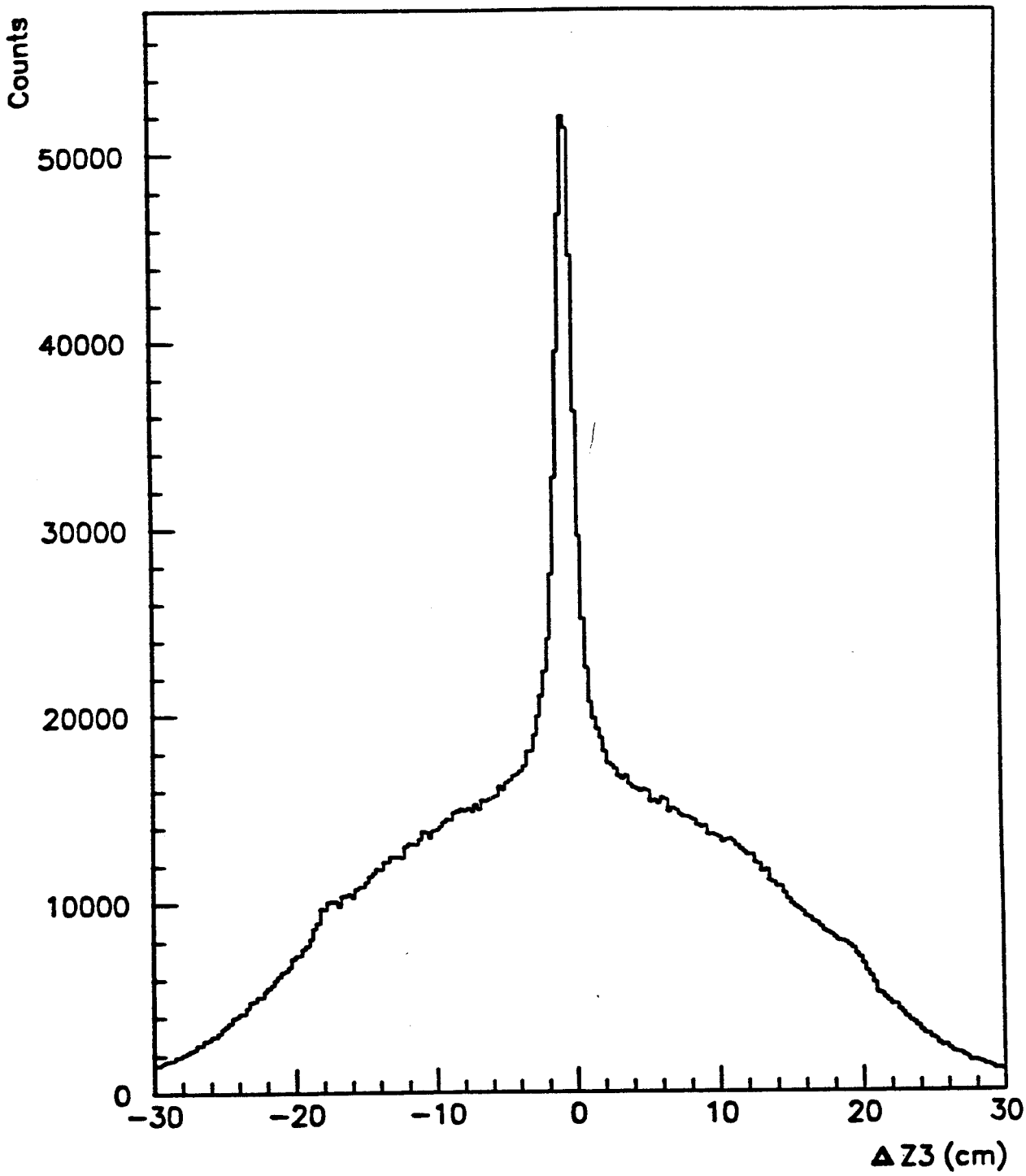

Figure IV.7: $\Delta Z3$ in cm

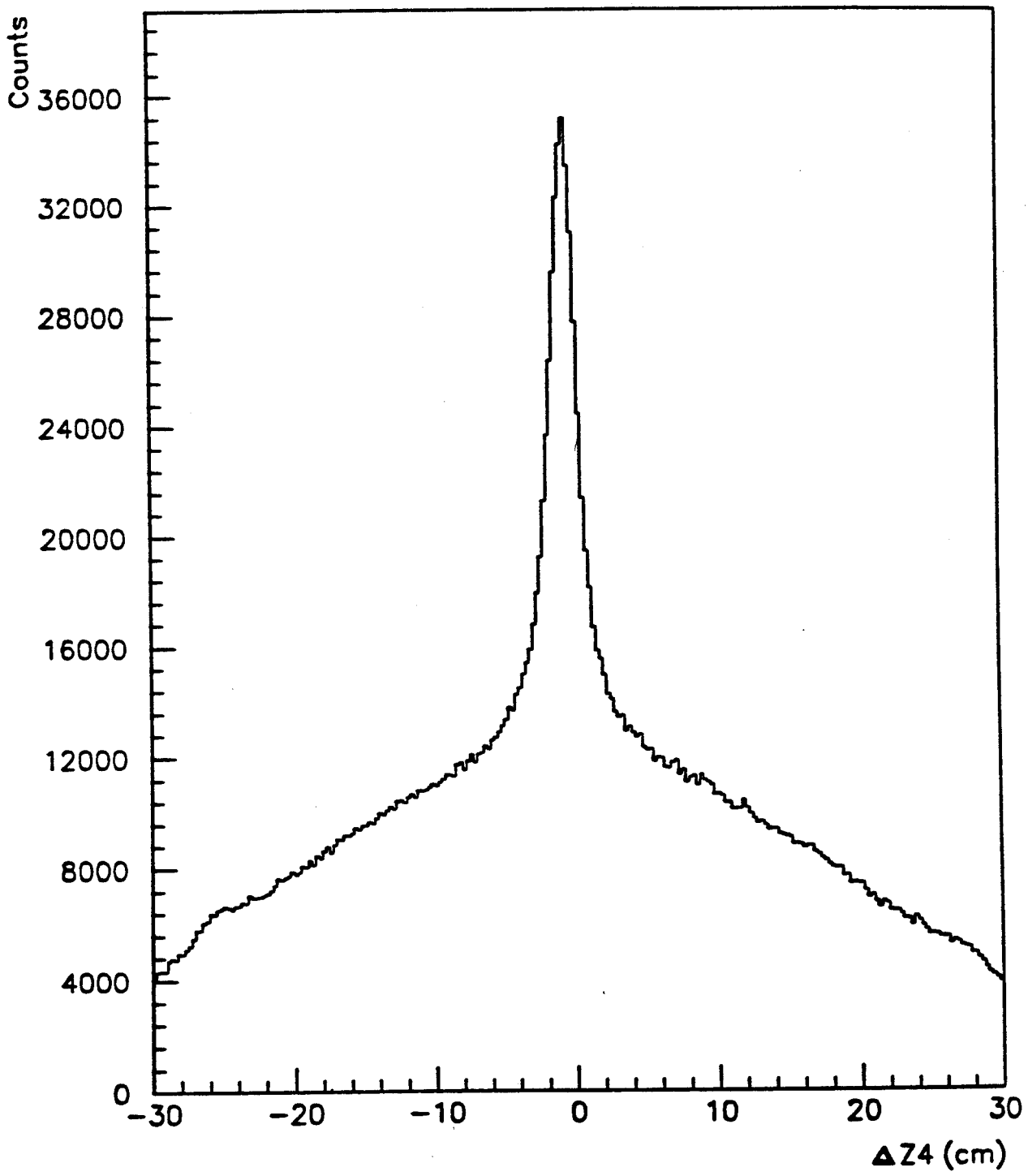

Figure IV.8: $\Delta Z4$ in cm

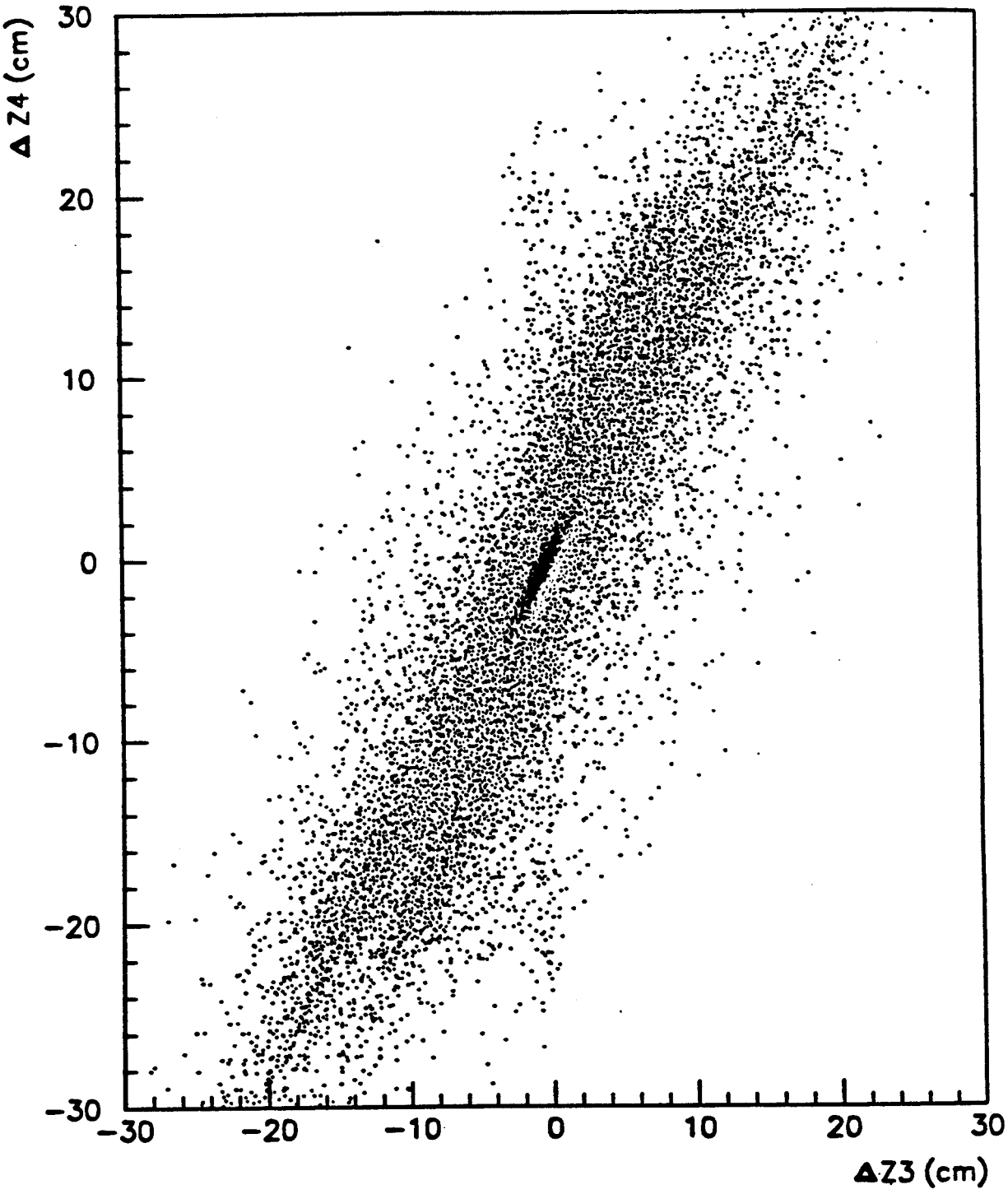

Figure IV.9: $\Delta Z3$ vs $\Delta Z4$, showing the correlation between them.

There are now four parameters which can be used in selecting the matching of hits to form a track (TTB, ΔR, $\Delta Z3$, and $\Delta Z4$). As can be seen from Figures IV.1, IV.5, IV.7, and IV.8, these are all useful quantities which can be used in track reconstruction. However, because of the approximations involved, a track may have a good TTB and ΔR but a bad $\Delta Z3$ and $\Delta Z4$; thus, the question arises as to how to pick the best combination of all four test parameters simultaneously.

5 χ^2 Test

A χ^2 method was used to minimize five parameters (five instead of four because the target trace back has X and Y components). χ^2 is defined as

$$\chi^2 = \sum_{i=1}^{n} w_i \left(\frac{x_i - X_i}{\sigma_i}\right)^2, \qquad \text{(IV.5)}$$

where x_i are the five parameters for a specific combination of hits, X_i is the average value of each parameter, σ_i is the standard deviation of each parameter, and w_i is the weight attached to each parameter. The smallest χ^2 then results from the most likely correct combination of hits to form a track. Table IV.1 shows the average, the standard deviation, and the weight used for each of the parameters for this χ^2 calculation. The X and Y directions refers to the X and Y coordinates of the target trace back. The entries in the table for these two values are an example from an experimental run. (The beam spot moved from run to run, so the values for these two parameters differed, depending on which run was being analyzed.) The reason $\Delta Z3$ and $\Delta Z4$ are not weighted equally with the other parameters is because they are correlated (Figure IV.9). It should also be noted that the average values (X_i) for ΔR, $\Delta Z3$, and $\Delta Z4$ are not centered at zero. This will be discussed later.

There is still one other problem. When two particles go through the spectrometer, there will be two hits in each wire chamber and, therefore, sixteen possible combi-

Parameters	X_i	σ_i	w_i
Y direction	0.42	0.69	1.0
X direction	-0.42	0.87	1.0
ΔR	0.25	0.30	1.0
$\Delta Z3$	0.50	1.11	0.5
$\Delta Z4$	0.75	2.03	0.5

Table IV.1: The average value, standard deviation, and weight of each parameter used in the calculation of χ^2.

nations accompanied by sixteen χ^2 values. The lowest χ^2 value will determine the combination of hits which forms the first track. Now the question becomes how to pick the best combination out of the remaining fifteen to form the second track. Intuitively, one would pick the second smallest χ^2 value. There is a problem with this, being that the second smallest χ^2 value represents a combination of four hits, some of which may have been used by the first track. As an example, see Figure IV.10. In this figure only three tracks have been drawn out of the possible sixteen, and each track has a χ^2 value associated with it. Imagine that the smallest χ^2 value was associated with track 1, the second smallest with track 2, and the largest χ^2 with track 3. The smallest χ^2 value would then represent the first chosen track, and if the next smallest χ^2 value were to be used as the determining factor for the second track, track 2 would be chosen as the correct combination of hits. However, it is very unlikely that two tracks will share two hits, so the wrong combination of hits would be chosen for the second track.

To solve this problem an additional condition has been added. The correct combination of hits chosen comes from the next smallest χ^2 value which does not share any hits from the first track.

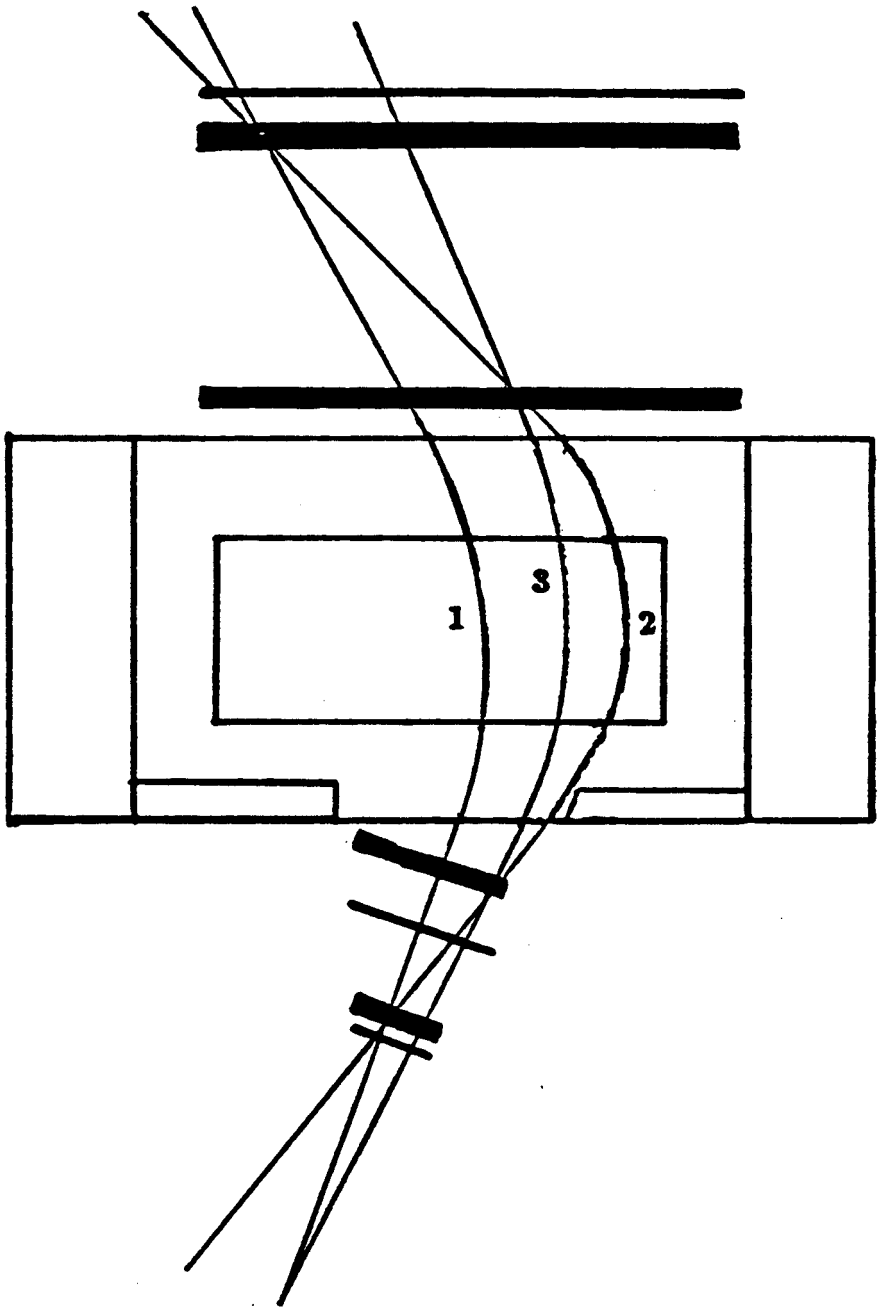

Figure IV.10: χ^2 values calculated from various hit combinations.

It is possible, however very unlikely, to have three particles going through the spectrometer; again, the third track is found by using the next lowest χ^2 value which does not share any hits with the previous two tracks. Out of some 22,000 tracks three track events were recorded only 25 times(0.1%), and all the third tracks had χ^2 values in the 2×10^6 and above range. This points to the fact that the combination of hits which form the third χ^2 values were unlikely candidates, so all third tracks were thrown away.

The χ^2 values can now be compared for all the possible combinations and for only the chosen combinations (Figure IV.11). As can be seen, much of the background disappears. This background corresponds to all the tracks formed from bad combinations of hits.

Now that the choosing of tracks based on the χ^2 values has been implemented, let's take a look back at the corrected ΔR, $\Delta Z3$ and $\Delta Z4$ plots (Figures IV.12, IV.13, and IV.14). As can be seen, all the tracks which were formed from the wrong matches have been removed. It is also more noticeable that all three of the parameters are not centered exactly on zero. It was noticed during the analysis that a 1.7 mm offset in MWPC 2 caused a 2 cm offset in $\Delta Z3$. It is very likely that a combination of very small offsets in the relative position of the wire chambers are responsible for these parameters not being centered on zero. The zero field data used to determine the position of each of the wire chambers (this chapter, section B, subsection 1) is limited in precision because of the wire spacing (2 mm) in each wire plane. Another possibility for the offset in $\Delta Z3$, and $\Delta Z4$ is parallax in the wire chambers.

One further requirement used once the track had been found was that the correct AB scintillator had to have produced a signal. If this was not the case, that track was thrown away. About 0.05% of found tracks were thrown away due to this restriction.

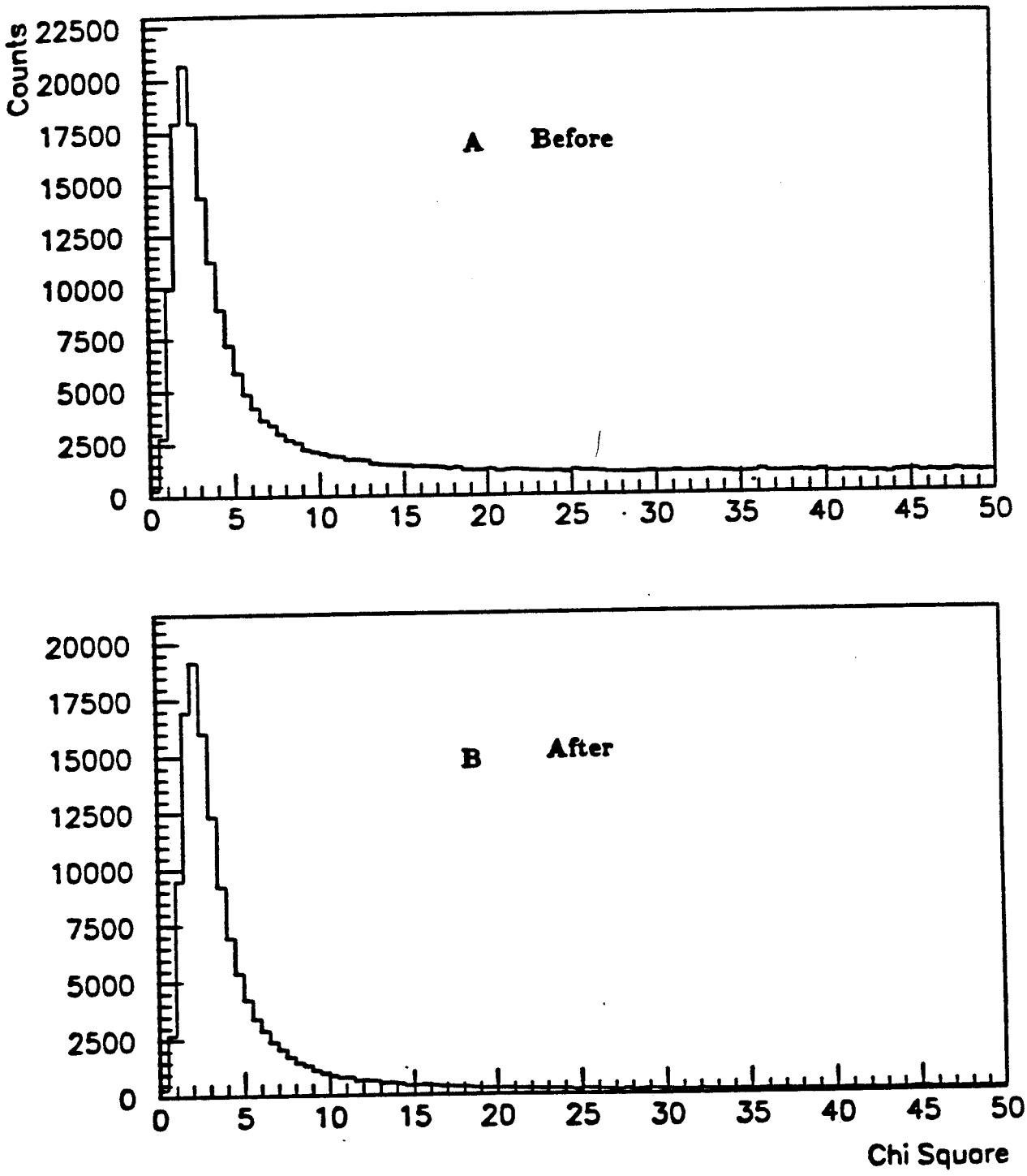

Figure IV.11: A) The χ^2 values for all the possible combinations of wire chamber hits. B) he χ^2 values for only the chosen combinations of wire chamber hits.

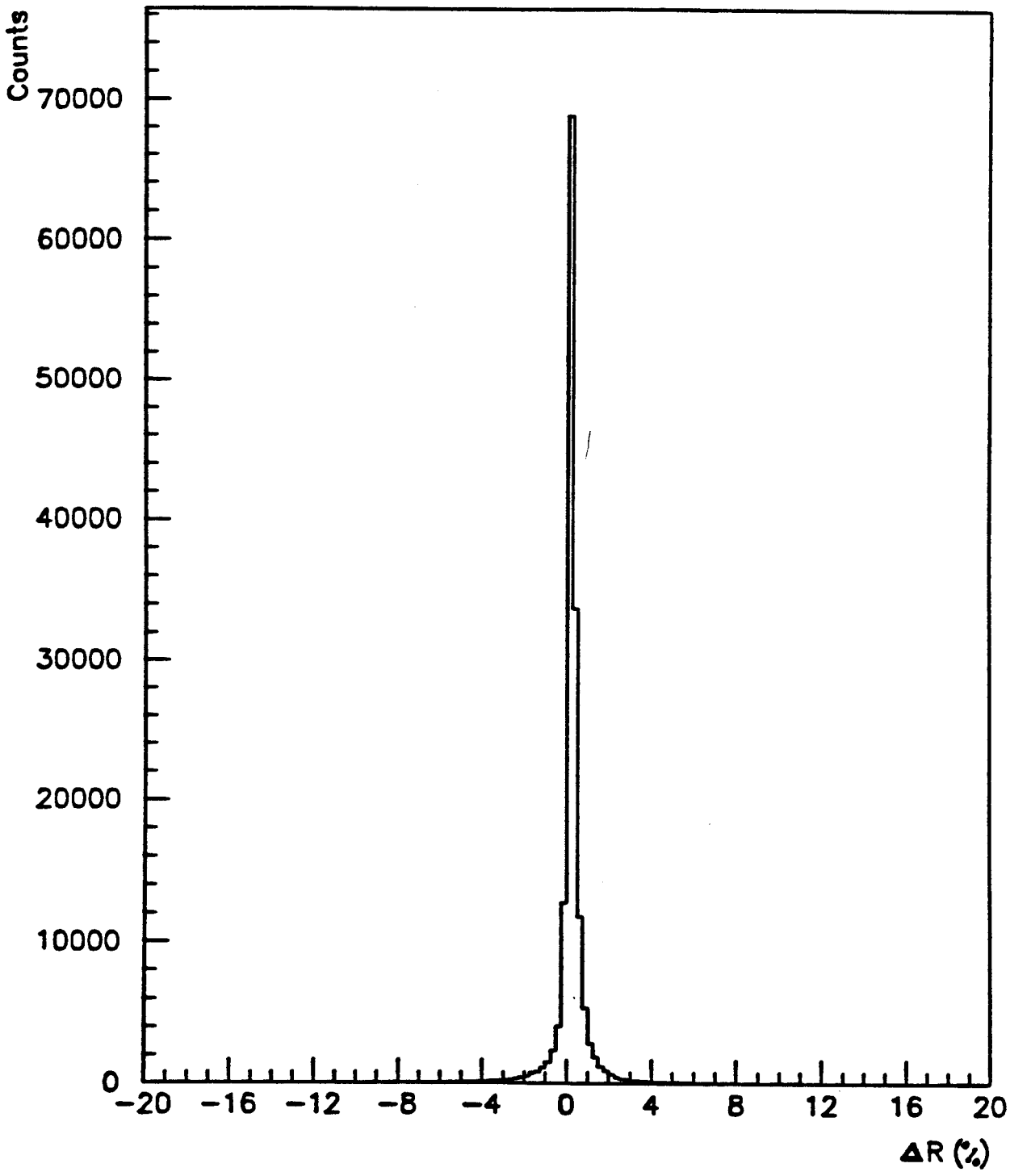

Figure IV.12: ΔR after the χ^2 test.

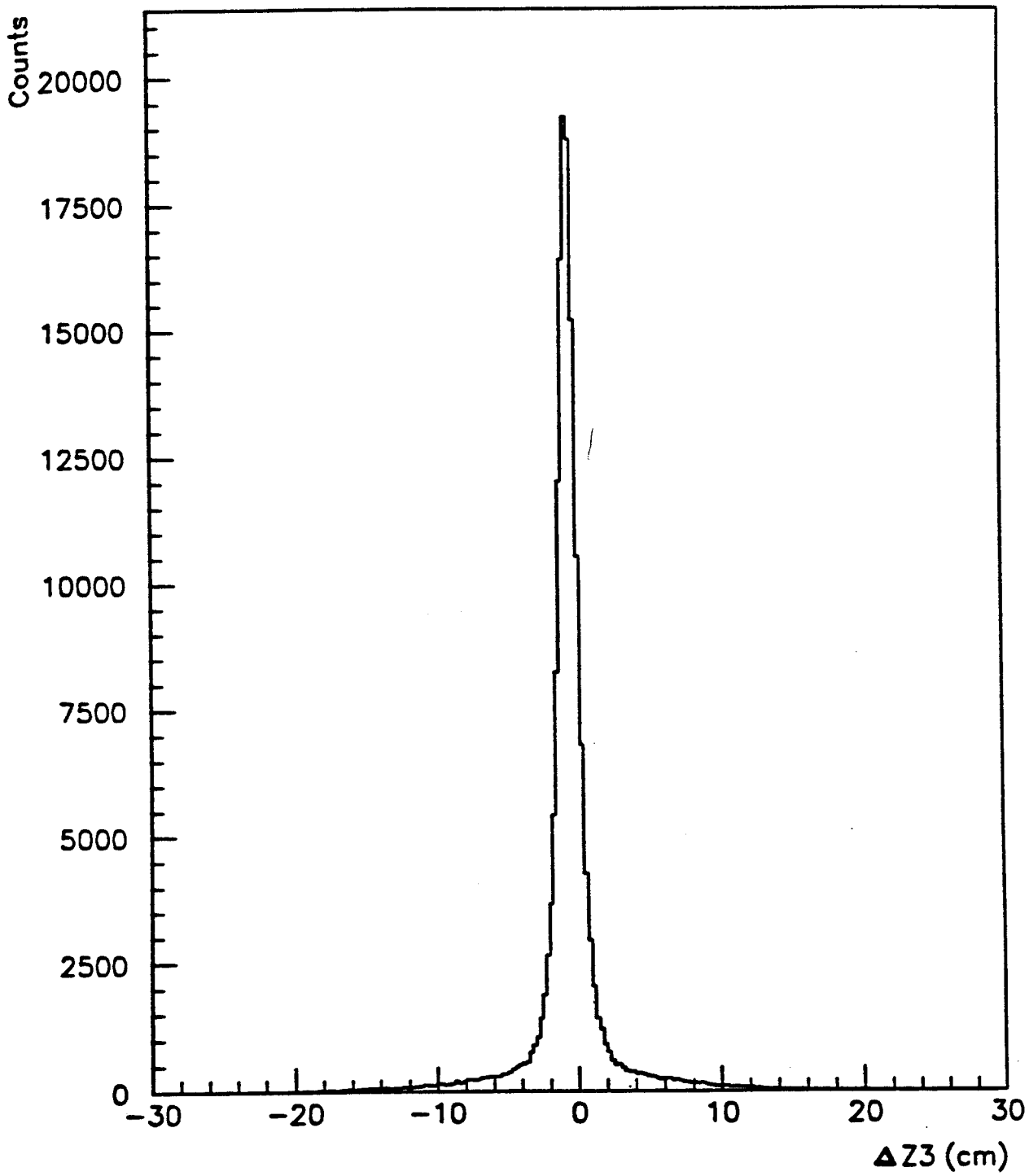

Figure IV.13: $\Delta Z3$ after the χ^2 test.

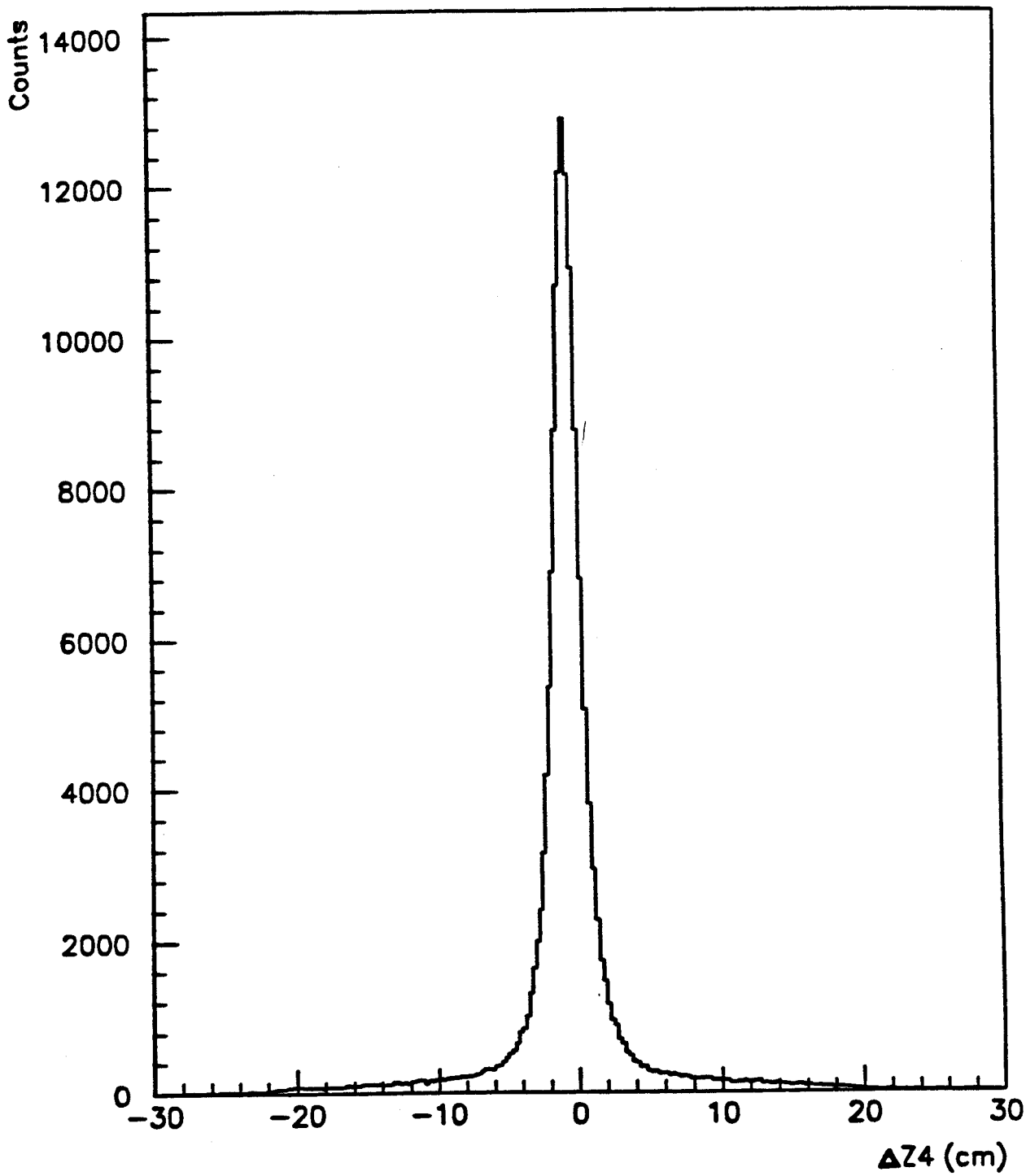

Figure IV.14: $\Delta Z4$ after the χ^2 test.

C Particle Identification

This section corresponds to box III on the flow chart at the beginning of this chapter.

As was mentioned in the first part of Chapter III, particle identification needed to be done using a combination of the time of flight, energy loss, and rigidity information. Due to the fact that S2 was not sufficiently segmented, the time of flight information was very poor. The problem arrises from the fact that S1 (Figure III.3) was too far away from the target. When a reaction occurs between the beam and the target, there are quite a few very fast particles which come out. These fast particles then pass through S1, where the timing is started. Because these are fast particles, they do not get bent through the spectrometer. Some time after the fast particle, a slower moving particle can come along and pass through S1. It is at this point that the timing should start; however, the timing has already been started. Because the second particle is slower moving, it is bent through the spectrometer, and crosses the AB array, which stops the timing. This timing is, of course, much longer then it should have been because it was started early by a faster moving particle. This problem caused a discrepancy, of up to a three nanoseconds and caused the time of flight vs rigidity bands to be much wider, and made any particle identification using TOF very limited. The upshot of this is that energy loss and rigidity were the two primary pieces of information which were available to do particle identification.

As you may remember, the reason for obtaining the time–of–flight information was the inability to separate ^{3}H and ^{3}He using just the energy loss and rigidity information (Figure III.2). Fortunately, the ADC response from a scintillator (related to energy loss) is quite particle dependent. Figure IV.15 [Good60] shows the light output produced in NE 102 scintillators as a function of total particle energy for various particle types. Since the ADC output is proportional to light output, it is

thus particle dependent; a plot of ADC output vs rigidity (Figure IV.16) actually separates all six particle types (π, H, ^{2}H, ^{3}H, ^{3}He, and ^{4}He). The ADC output shown in all the figures from now on is an ADC value which has been corrected for the path length inside of the scintillator.

Before continuing with the particle identification, it is necessary to deviate a bit and discuss the rigidity determination.

1 Rigidity

The equation used to calculate rigidity is

$$R = \frac{0.3\, B_o l}{\mid sin\theta_{in} - sin\theta_{out} \mid}, \tag{IV.6}$$

where B_o is the magnetic field in kiloGauss (kG), l is the effective edge width of the field (this is constant in meters), and θ_{in} and θ_{out} are the angles the in–coming and out–going tracks, make with the magnet. The 0.3 is the constant which will take the units of kG meters to GeV/c, it has units of (Coulombs GeV/c sec/meter) The derivation of equation IV.6 can be found in Appendix B of reference [Zajc82] and will not be repeated here. However, as a rough justification, one would expect that the measured rigidity would depend upon the field strength and the length of the field. Also, one would expect that the angles of the in– and out–going tracks are measures of the rigidity.

The important thing to notice is that the calculation of rigidity uses an effective edge approximation and needs to be corrected because this is only a good approximation to within 5%. This is where Chebyshev polynomials come into play. Because these polynomials are related to the Monte Carlo method, the explanation can be found in Appendix A. This corresponds to boxes IV, V, and VI in the flow chart at the beginning of this chapter.

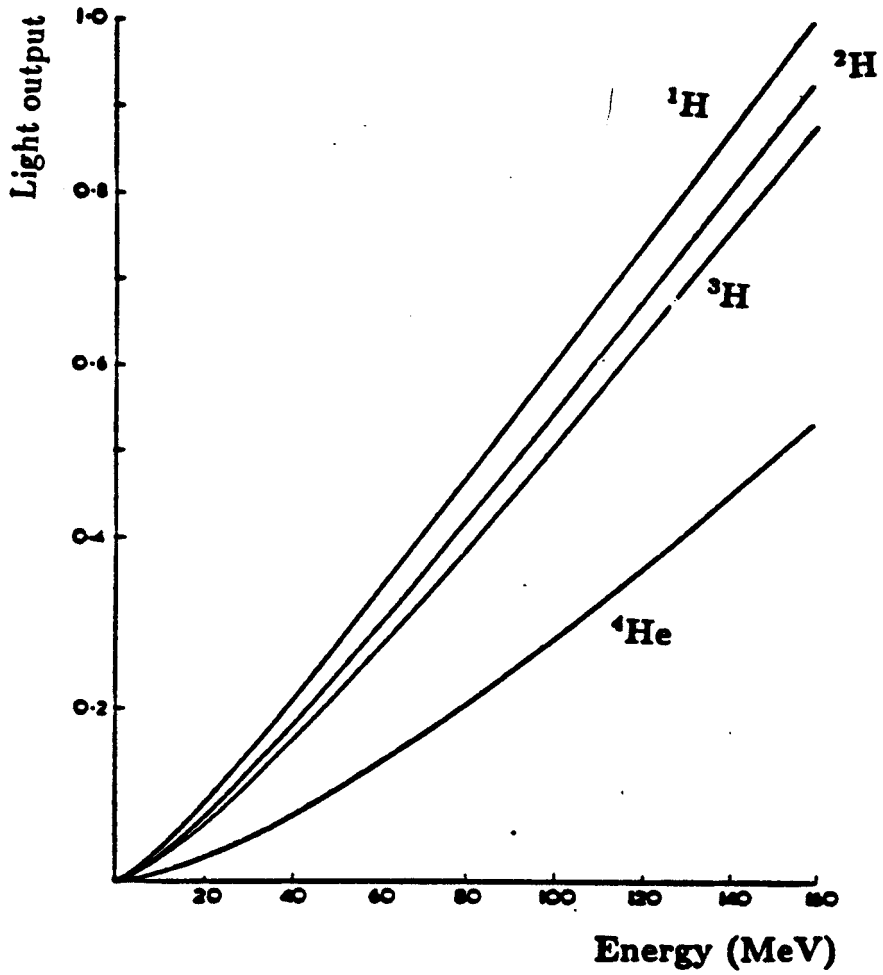

Figure IV.15: The responses of various particle types in NE 102 scintillator [Good60].

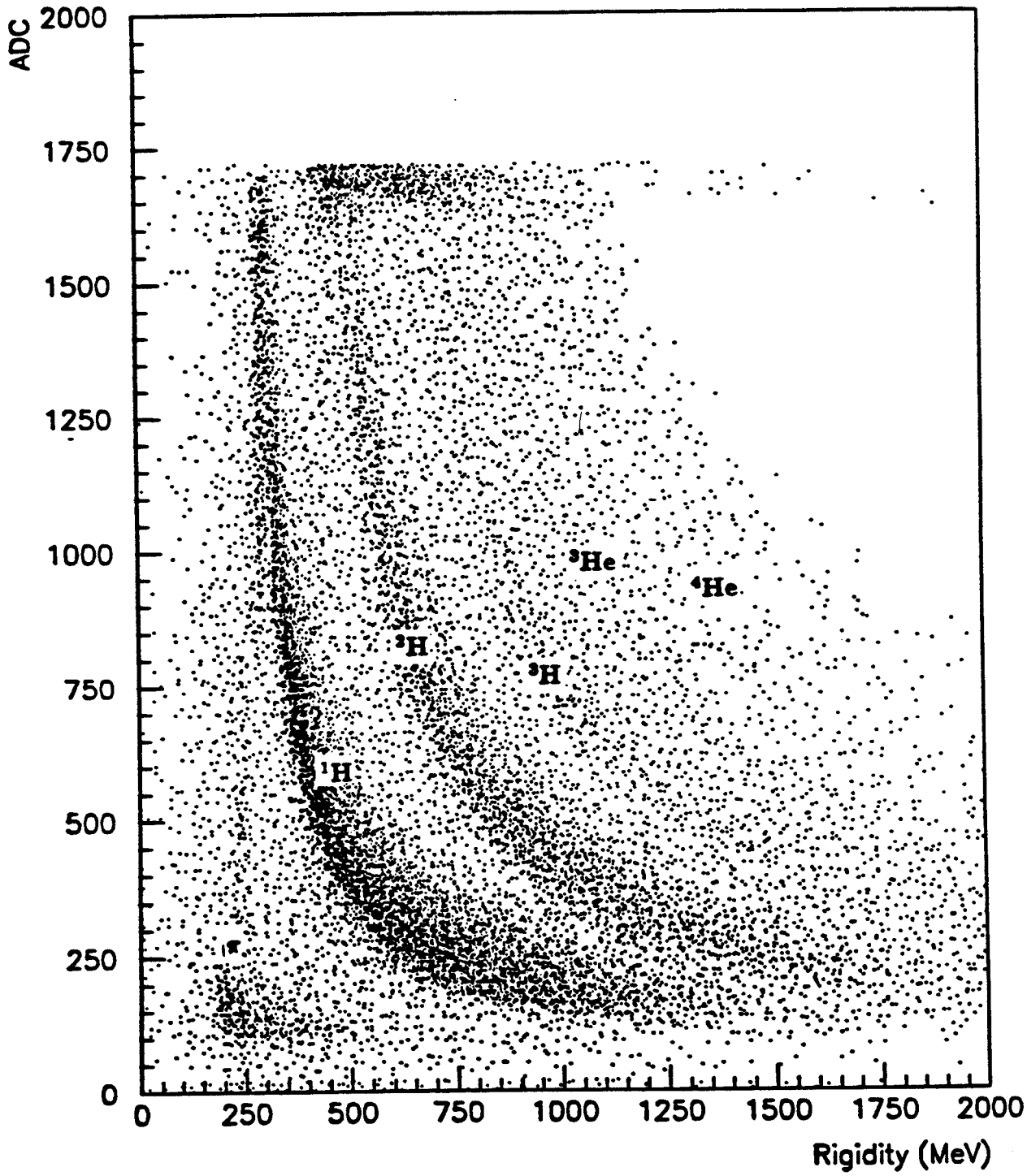

Figure IV.16: ADC output vs Rigidity. Each band represents a particle type.

2 Particle Identification

Now the problem is to find a quantitative way of separating these various particle types. From Figure IV.16 it is visually easy to separate the various particle types, where each dark band represents a particular particle. However, the separation has to be done by a relatively simple–minded computer. In order to separate the bands one would have to tell the computer where to place the cuts between the various dark bands, which could be quite arbitrary. The first thing to realize is that it is easier to place the above–mentioned cuts if the bands were made into straight lines instead of the present exponential shapes. With this in mind, let's take a look at the equations for energy loss:

$$ADC \propto \frac{dE}{dx} \propto \frac{Z^2}{\beta^2}. \tag{IV.7}$$

This is a restatement of equation III.3. Next, let's take equation III.1 and square it.

$$R = \frac{\gamma\, m\, v}{Z} \tag{IV.8}$$

$$R^2 = \frac{\gamma^2\, m^2\, v^2}{Z^2}\ . \tag{IV.9}$$

Next, divide through by c^2 and do a bit of algebra; this leads to

$$\frac{R^2}{c^2} = \gamma^2\, m^2\, \frac{\beta^2}{Z^2}\ , \tag{IV.10}$$

$$\frac{R^2}{\gamma^2\, m^2\, c^2} = \frac{\beta^2}{Z^2}. \tag{IV.11}$$

Combining equations IV.7 and IV.11 produces

$$\frac{dE}{dx} \propto \frac{\gamma^2\, m^2\, c^2}{R^2}\ , \tag{IV.12}$$

$$R^2\, \frac{dE}{dx} \propto \gamma^2\, m^2\, c^2\ . \tag{IV.13}$$

Thus, a plot of (R^2 dE/dx) vs R should produce straight horizontal lines which are dependent only upon the particle mass. The problem is that instead of dE/dx, the

only information available is the ADC output, which is related but not equivalent. By trial and error it was found that a plot of ($R^{1.75}$ ADC) vs R (Figure IV.17) produced the straightest lines.

It is now much easier to place the cuts between the bands (only two bands stand out, the others are suppressed due to the intensity of these first two) in order to separate the various particle types. However, there still remains the problem of the arbitrariness of where to place these cuts. The way to get rid of this problem is to take slices along the rigidity axis and look at the projections which are produced. For example, take the slice along the rigidity axis from 0.9 to 1 GeV (Figure IV.18). Now, let's take a look at the projection of this figure (Figure IV.19). The first peak in Figure IV.19 is the proton band, the second peak the deuterons, and so on all the way to ^{4}He. A cut is placed at the bottom of the valley of the first two peaks, and everything to the left is called a proton; this process can be repeated all along the X axis. When it is all done, the protons are separated (Figure IV.20). This process can be repeated for all particle types. The separations obtained is shown in Figure IV.21.

In Figure IV.16 there is a dark band which stretches horizontally at the top. This band is produced by overflow, which means that when the particle crosses through the scintillator it deposits a large amount of energy higher than the electronics capability to digitize. Such particles can be identified by doing the same process mentioned above, except instead of using the ADC output from the A array, the ADC output from the thinner B array is used. The energy resolution of the B array is not so good as that of the A array, but it is sufficient to resolve the overflows of the A array.

Now that particle types are separated, the cross sections can be determined. This is the last box in the flow chart at the beginning of this chapter. Before these cross sections can be calculated, the efficiencies of the various parts of this analysis must

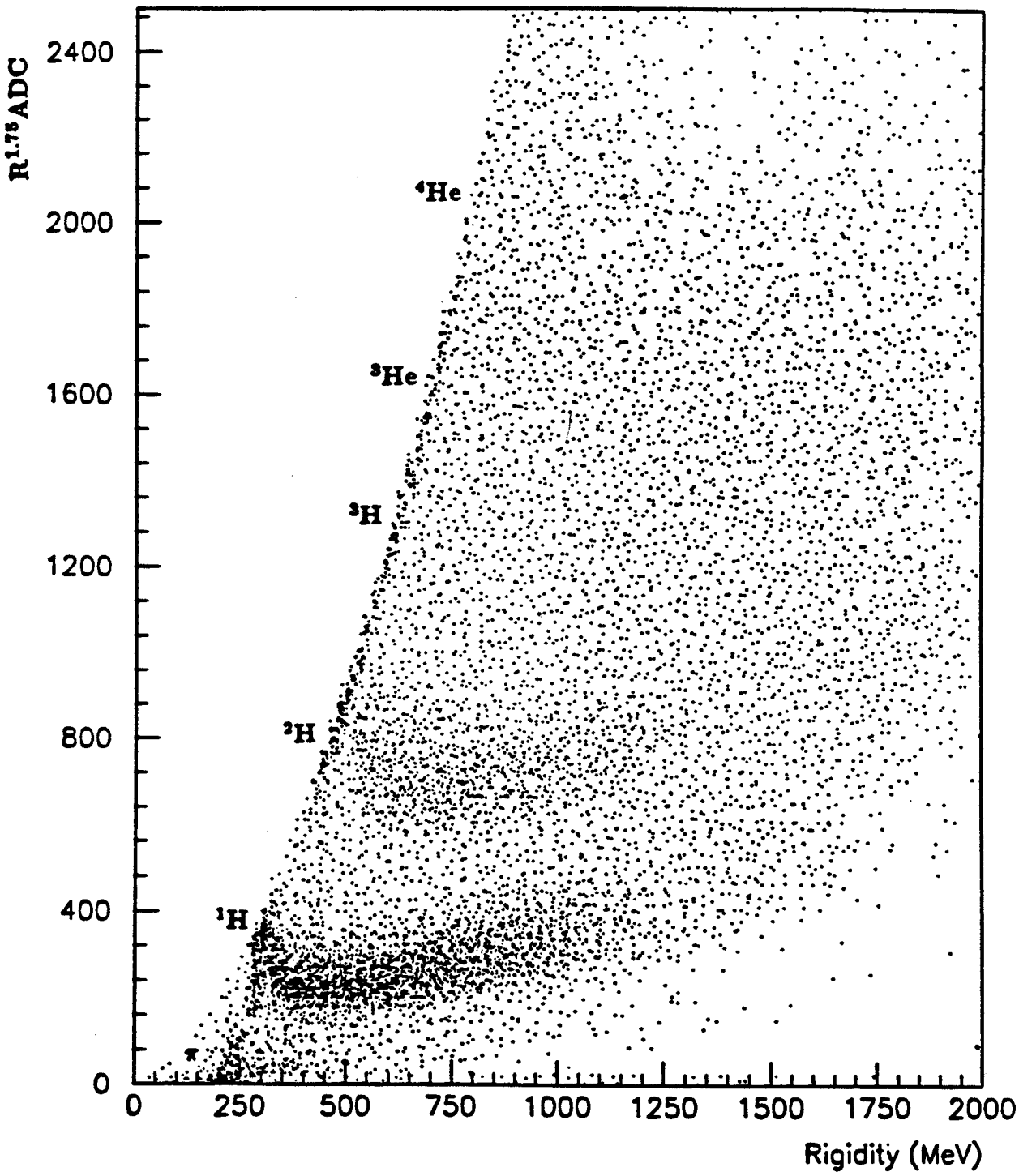

Figure IV.17: Plot of ($R^{1.75}$ ADC) vs. R. Each band represents a particular particle type.

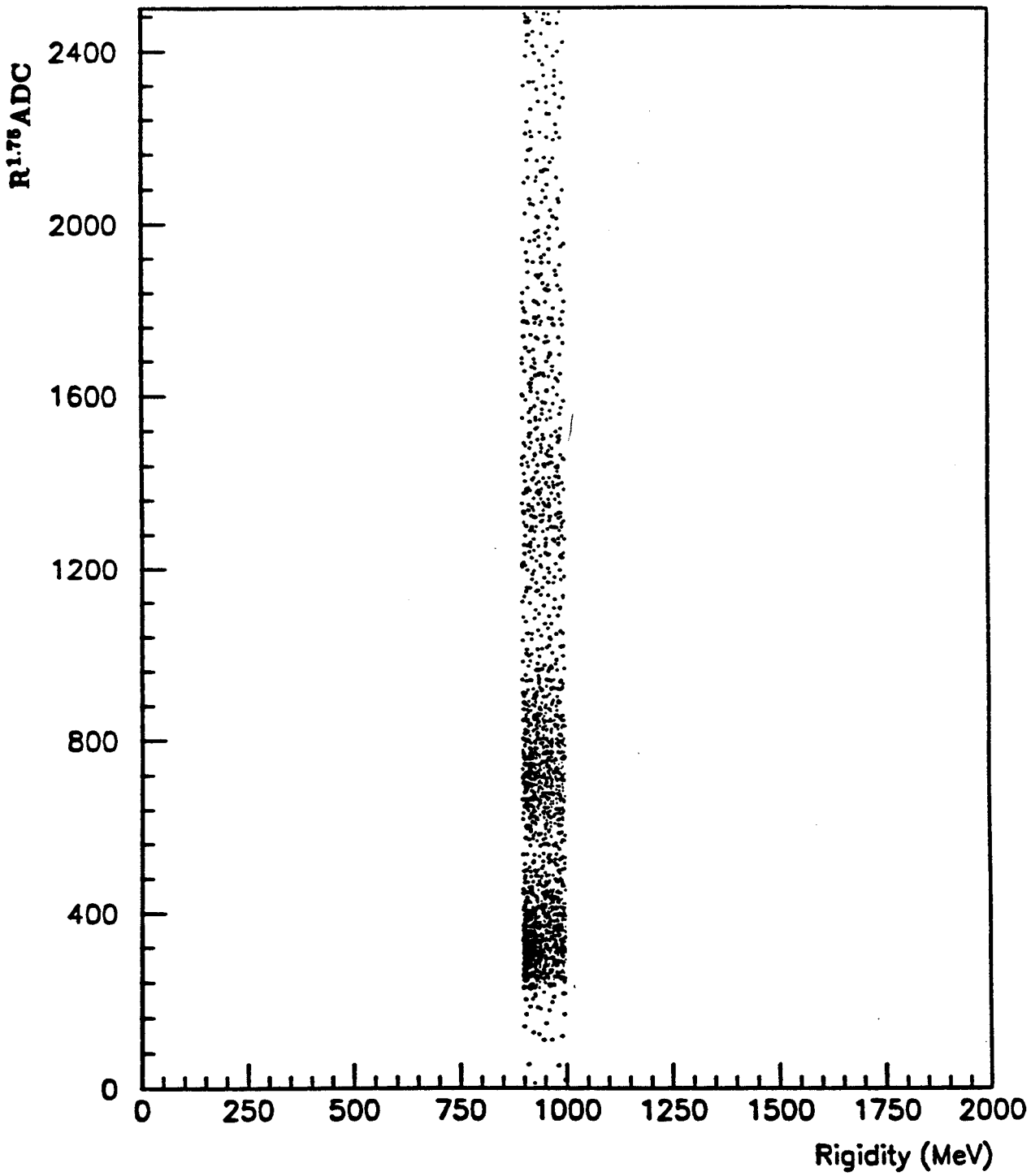

Figure IV.18: A slice on the rigidity axis of Figure IV.17

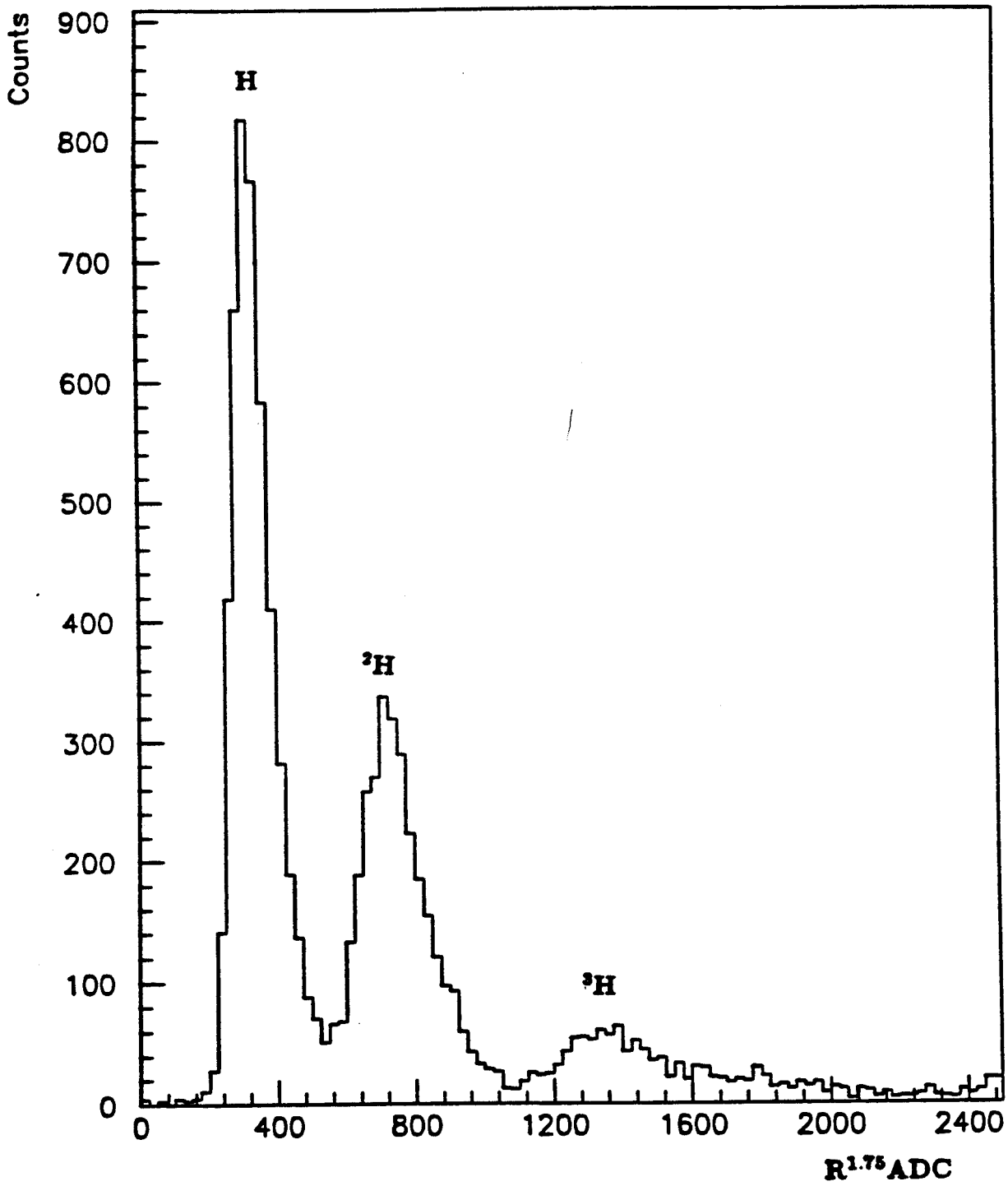

Figure IV.19: A projection of Figure IV.18 on to the $R^{1.75}$ ADC axis.

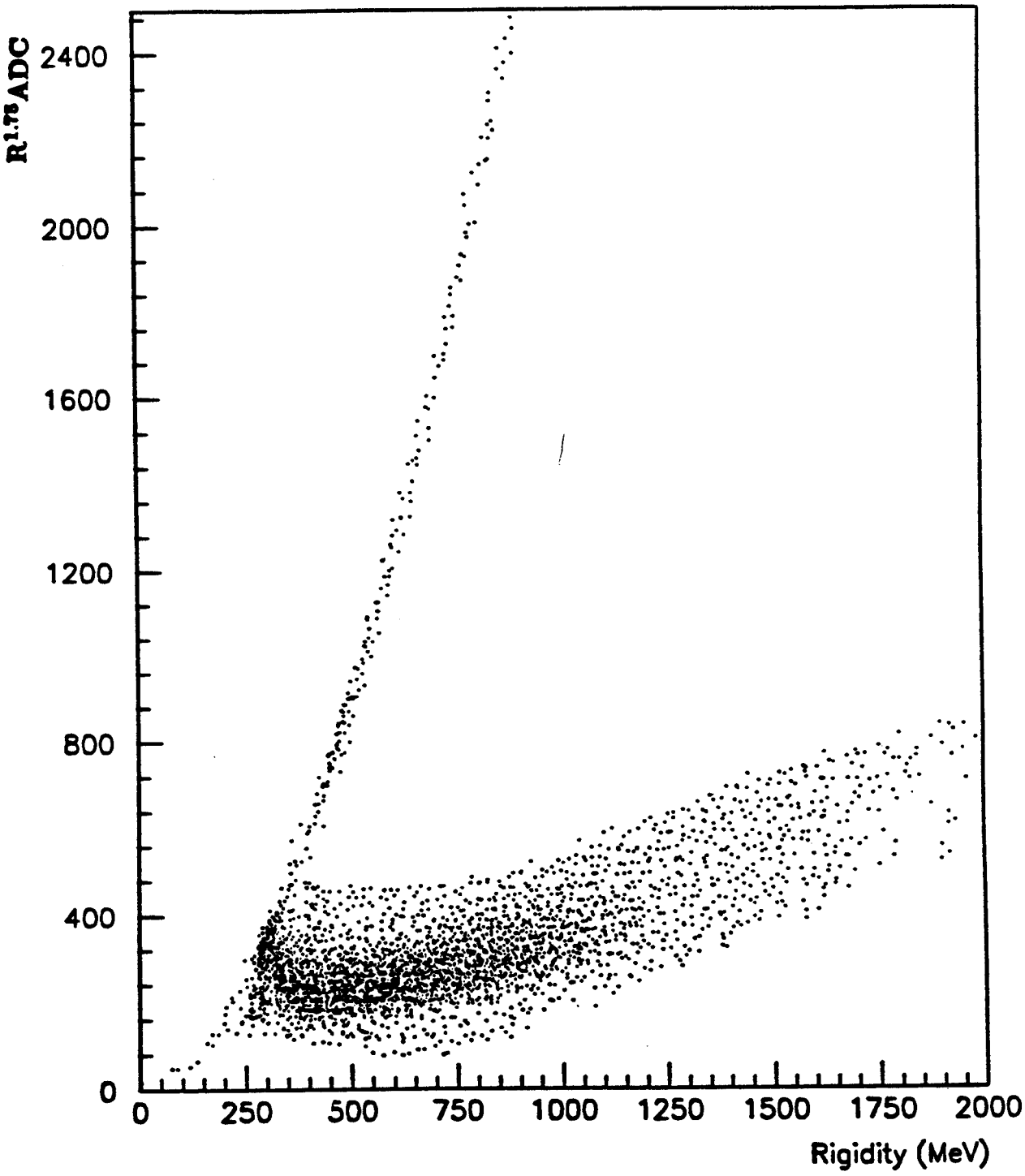

Figure IV.20: Separation of protons via projections.

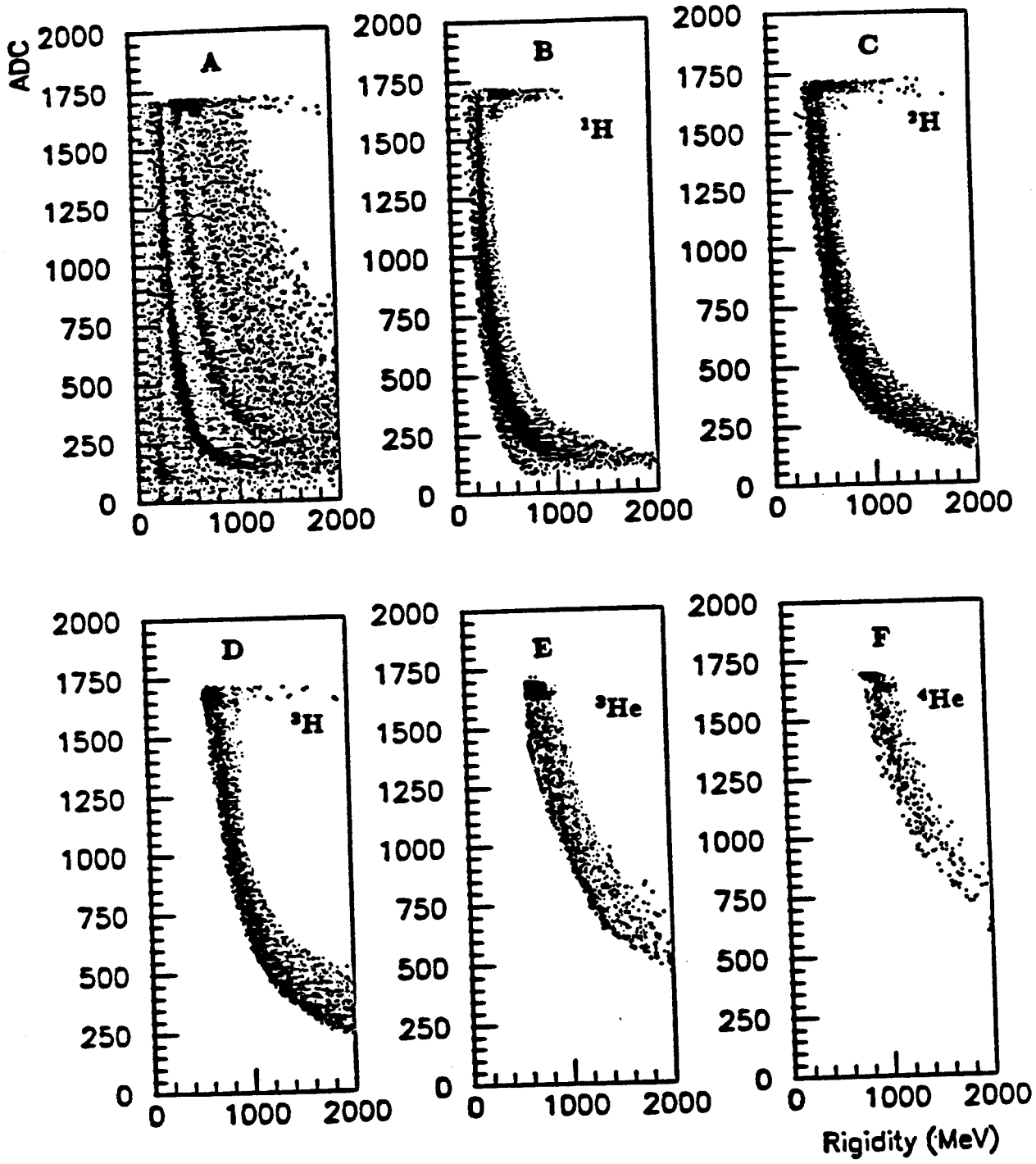

Figure IV.21: A) all the particle types; Figures B through F represent the separations obtained using projections.

be known. This is addressed in the next chapter.

One last thing needs to be addressed in this chapter before continuing: particle misidentification.

3 Particle Misidentification

The method of particle separation described above will misidentify some particles. It is important to know the amount of misidentification which will occur.

Going back to Figure IV.19, it can be seen that some misidentification will occur in the tails of each of the peaks. These tails are being cut at the lowest intersection point of the two peaks. The problem is to estimate how many particles are in the tails. A rough estimation can be accomplished by first assuming that these peaks are Gaussian and then visually measuring the full width at half maximum (FWHM) of each peak. The FWHM is roughly related to σ of that peak by

$$\sigma = 0.4246\, FWHM. \tag{IV.14}$$

At this point one can measure how far the cut lies from the peak in terms of the number of σ's. The number of σ's then in turn reveals the fraction of the curve which falls within the tail which has been cut off.

This procedure was performed for all particle types. The largest misidentification was a little over 1%, while the average misidentification was on the order of 0.25%.

Chapter V

Efficiencies

A Introduction

The overall efficiency of the spectrometer is about 25%. In this particular case "efficiency" of the spectrometer refers to the efficiency of the spectrometer at detecting p–like particles rather then its geometrical efficiency. For example, if the spectrometer only detects 90% of the particles, then the cross sections must be corrected for the 10% inefficiency.

The efficiency is always very experiment dependent. The efficiency of the Janus spectrometer was calculated by

$$\mathcal{E} = \mathcal{E}_{trigger}\mathcal{E}_{hits} , \tag{V.1}$$

where $\mathcal{E}$ is the overall efficiency. The rest of this chapter is spent on explaining and calculating the two factors, $\mathcal{E}_{trigger}$ and $\mathcal{E}_{hits}$.

$\mathcal{E}_{trigger}$ is the more complex of the two factors, so let's start with it. As was mentioned in Chapter III, a trigger had been set up to avoid taping useless information and to simplify the data analysis. The condition for the trigger was

$$Trigger = S * \Pi * FO \ . \tag{V.2}$$

This equation means that a electrical signal must be observed from each of the three

components within a specific time gate. Looking back at Figure III.3, the components correspond to the following:

$$\begin{aligned} S &\Longrightarrow & S1 * S2 \\ \Pi &\Longrightarrow & AB \text{ array} \\ FO &\Longrightarrow & \text{wire chambers 1 through 4} \end{aligned} \tag{V.3}$$

If there is a simultaneous signal from each of the above, it is likely that a particle went through the spectrometer. However, if any one of these components fails to give a signal, then such an event cannot be used, and whatever caused the other signals is completely discarded.

The problem is that one has to deal with inefficiencies in the various parts of the spectrometer, meaning that a particle could actually go through a wire chamber or a scintillator and not produce a signal, at which point the trigger would not be satisfied and the track would be discarded even though it was produced by a legitimate particle. It is therefore imperative to know the efficiency of each piece of the trigger so that the cross sections can be corrected for these inefficiencies. The efficiency of the trigger is

$$\mathcal{E}_{trigger} = \mathcal{E}_S \, \mathcal{E}_\Pi \, \mathcal{E}_{FO} \ , \tag{V.4}$$

where $\mathcal{E}_S$, $\mathcal{E}_\Pi$, and $\mathcal{E}_{FO}$ are the efficiencies of S, II, and FO, respectively. The following sections will describe the calculations for each of these three factors.

B Start Scintillator Efficiency

There are several reasons for which a scintillator may not produce a signal. First, when the particle passes through the scintillator, it may not deposit enough energy to produce a signal. Another reason is that the electronics which was set up for this

experiment may have been miscalibrated. In this experiment, time gates were set up such that if the signals did not fall within these gates, the data were discarded.

The first problem is negligible for several reasons: first, the particles that are being observed are massive and charged (equations III.3 and III.4), and second, these particles lie in a momentum range which is not quite minimum ionizing, meaning they deposit large enough amounts of energy to produce significant signals. This means that any significant inefficiency comes from the electronics of the spectrometer.

In order to measure the efficiency of S, it was removed from the trigger ($Trigger = \Pi * FO$). A comparison between the two runs, one with the normal trigger and one with S removed, was then performed. The comparison consisted of checking the abnormal trigger run for how many times S fired in the correct time range. The time of flight (TOF) was defined to be the time it took for the particle to travel from the S counters to the AB array. A measure of the time of flight would then be

$$\Delta(TDC) = TDC_{AB} - TDC_S\,. \tag{V.5}$$

Thus, one could look at the distribution produced by histogramming all the various $\Delta(TDC)$ values observed for both the normal trigger and the trigger without the S component (Figure V.1). As can be seen, the particles which register a value to the left of the dotted line in Figure V.1. C are particles which would under normal circumstances not be registered, even though they are legitimate. This is the inefficiency in S. As it turns out, S is (98.6±0.2)% efficient. This test on the TDC must be done for each AB paddle in the AB scintillator array.

C Thick Scintillator Efficiencies

As a reminder, Π is the symbol used to represent the AB array in the trigger logic. There are several reasons for the inefficiency of Π. First the particle may not deposit

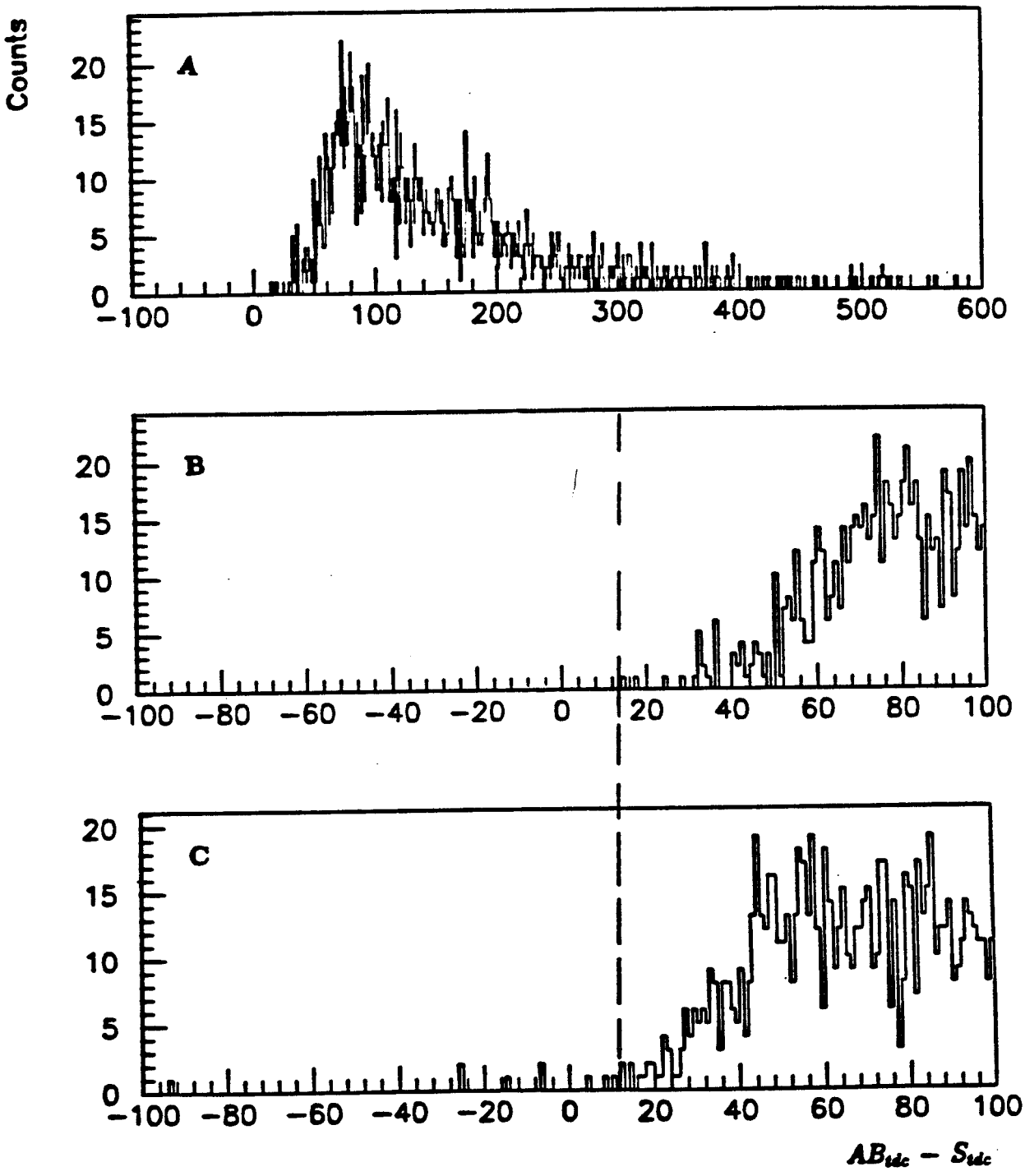

Figure V.1: A) shows the full TDC range for a normal trigger (100 ps/channel, offset of 3 ns). B) The TDC distribution is shown on an expanded scale for a normal trigger. C) A trigger without the S requirement. The dashed line corresponds to the timing efficiency.

enough energy as it passes through the scintillator. This explanation is discarded for the same reasons as for the S scintillators. Other reasons for the inefficiency are that the electronics may be miscalibrated and also the possibility that the particle passes through the small gaps between elements in the AB array, in which case no AB signal will be observed.

The efficiency of Π can be measured by removing Π from the trigger in a manner similar to S and using the equation

$$\mathcal{E}_{\Pi} = \frac{\#\text{ of tracks with }\Pi\text{ requirement}}{\#\text{ of tracks without }\Pi\text{ requirement}} \; . \tag{V.6}$$

The efficiency of Π was measured to be (99.16±0.04)%

D Fast–Out Efficiency

The Fast Out (FO) efficiency turns out to be beam–rate dependent. The extent of the dependence was not expected. This is the reason why it was stated at the beginning of the chapter that the overall efficiency is about 25%.

The FO electronics are very sensitive to the number of hits in the wire chambers. At higher beam rates there will be more hits, and the FO becomes less efficient. Unfortunately, this was not known at the beginning of the experiment, so only two points were obtained for a graph of beam rate vs FO efficiency. Thus, straight line was fitted for this curve, which will produce the dominant error for this experiment.

Before continuing with the Fast–Out efficiency, it is necessary to discuss beam rates.

1 Beam–Rate Determination

The beam rate is defined as the number of beam particles per some time period in some units. This can be determined by using the various scalers which have been set

up. By dividing the beam–counter master–gated scaler (Chapter III, Section E) by the master–gated time scaler a beam rate estimate is obtained. One can also take the counterpart run–gated scalers to obtain a beam rate. However, the two numbers are inconsistent because of the BEAM condition talked about in Chapter III, Section E.

The best way to explain the problem is through Figure V.2. The top curve shows the electronic beam gate, whose front edge starts the time gate (the middle curve). However, the real beam (last curve) is not so long as the beam gate. This causes the time scaler to start before the real beam and stop later than the real beam; the time is overcounted by

$$\Delta t = t_1 + t_2 . \tag{V.7}$$

The run–gated time scaler will count the time from t_{start} to t_{stop}, while the master–gated time scaler will only count the live time. Both, however, have overshot the timing by a time Δt. This extra time can be calculated and subtracted in order to obtain the real beam rate.

Whether the beam rate is calculated using the run–gated or master–gated scalers it should be the same, which allows us to calculate Δt. Thus, setting the two beam rates equal to each other,

$$\frac{IC2_{MG}}{T_{MG} - \Delta t} = \frac{IC2_{RG}}{T_{RG} - \Delta t} \tag{V.8}$$

where $IC2$ refers to the beam–counter scaler, T refers to the time scaler, and the subscripts MG and RG refer to whether the scaler is master–gated or run–gated. Δt can now be found and the beam rate can be calculated in units of scaler counts.

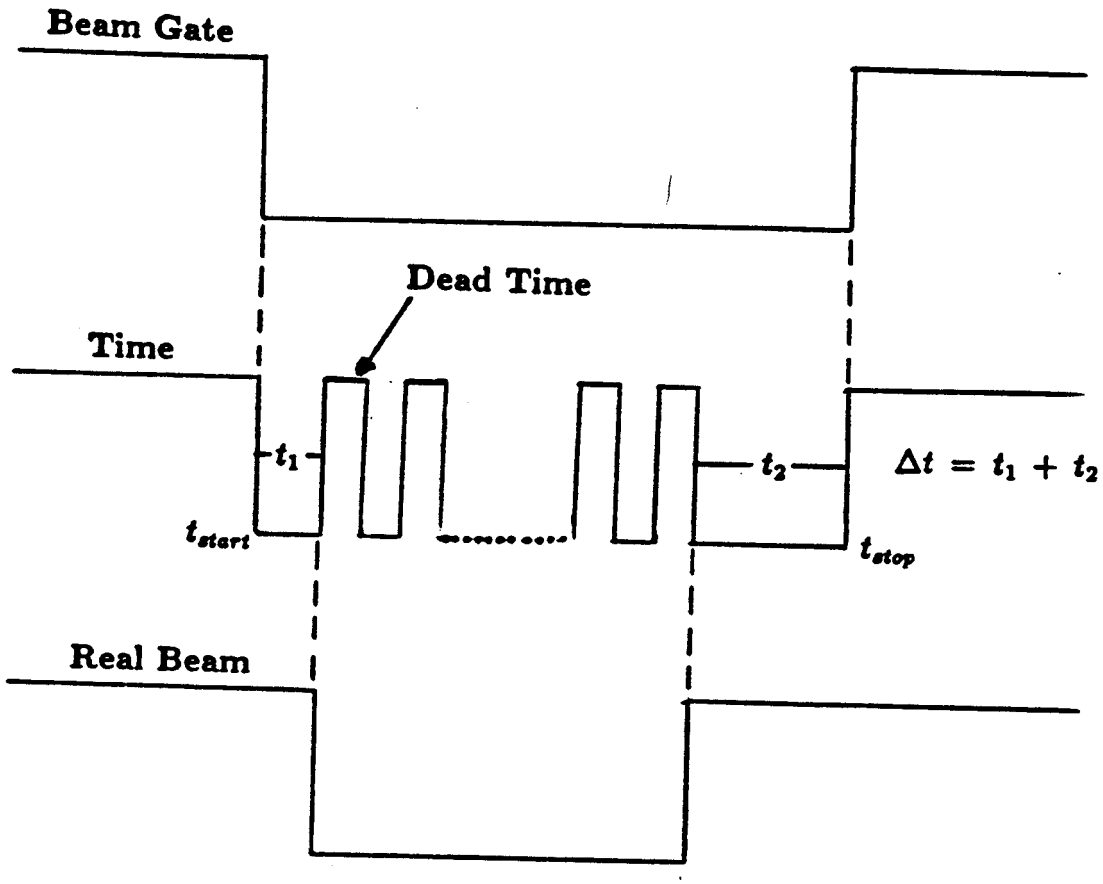

Figure V.2: Electronics logic diagram.

2 Fast–Out Efficiency Calculation

The FO efficiency was calculated by taking FO out of the trigger and using the formula

$$\mathcal{E}_{FO} = \frac{\#\text{ of tracks found per beam ion with FO in the trigger}}{\#\text{ of tracks found per beam ion with FO out of trigger}}. \qquad \text{(V.9)}$$

Basically, all that is being done is comparing the number of tracks found with and without the FO, which has to be done at the same beam rate. This is a problem because only two experimental runs were performed with the FO removed from the trigger; thus, the number of tracks found with FO out of the trigger have been measured for only two runs, both at different beam rates but neither at exactly the same beam rate as the other runs. This is handled by looking at plots of (# of tracks/IC2) versus beam rates (Figure V.3). The top line in Figure V.3 represents the line found using the two points from the runs with FO removed from the trigger. The lower line is from the run with FO in the trigger. As can be seen in Figure V.3, the runs with FO in the trigger were done at almost the same beam rates as the runs with FO removed from the trigger.

Now, the efficiency of each run can be calculated using equation V.9. Plotting the efficiency obtained for each run as a function of each of the beam rates, one obtains Figure V.4. Both Figures V.3 and V.4 are for the 65° configuration. Each of the three spectrometer configurations has its own curve. Table V.1 lists the slopes and the intercepts of the plots of Beam Rate vs FO Efficiency for the three configurations of the spectrometer. Given the beam rate, the efficiency of the FO can now be calculated.

One of the things to notice from Table V.1 is the fact that each of the three spectrometer configurations has a different curve. The difference possibly comes from two sources: The first is the proximity of the target to the wire chambers. If the target is closer to the wire chambers, a lot more hits will be registered in the wire

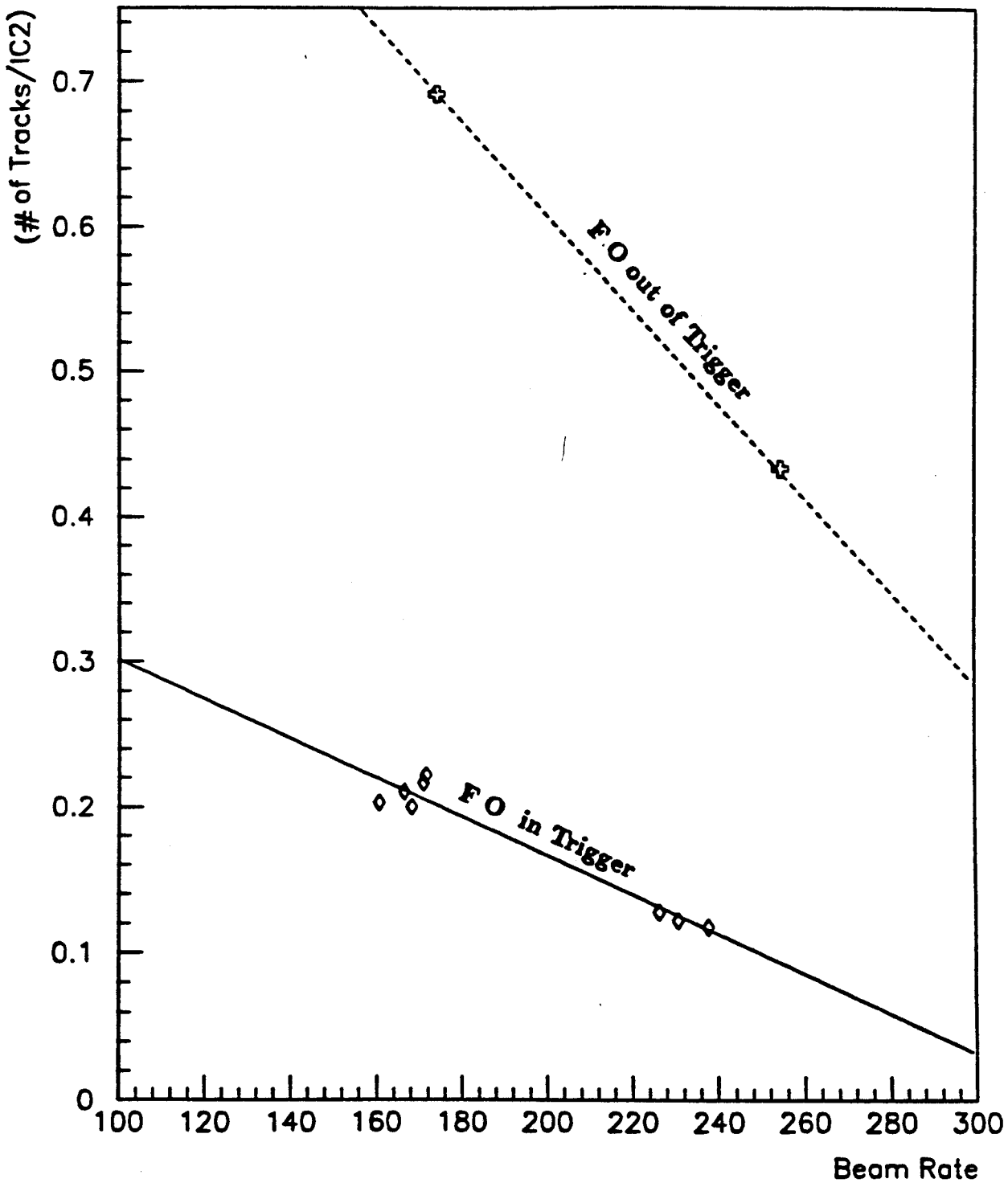

Figure V.3: Comparison of number of tracks as a function of beam rate between runs with the FO in and out of the trigger.

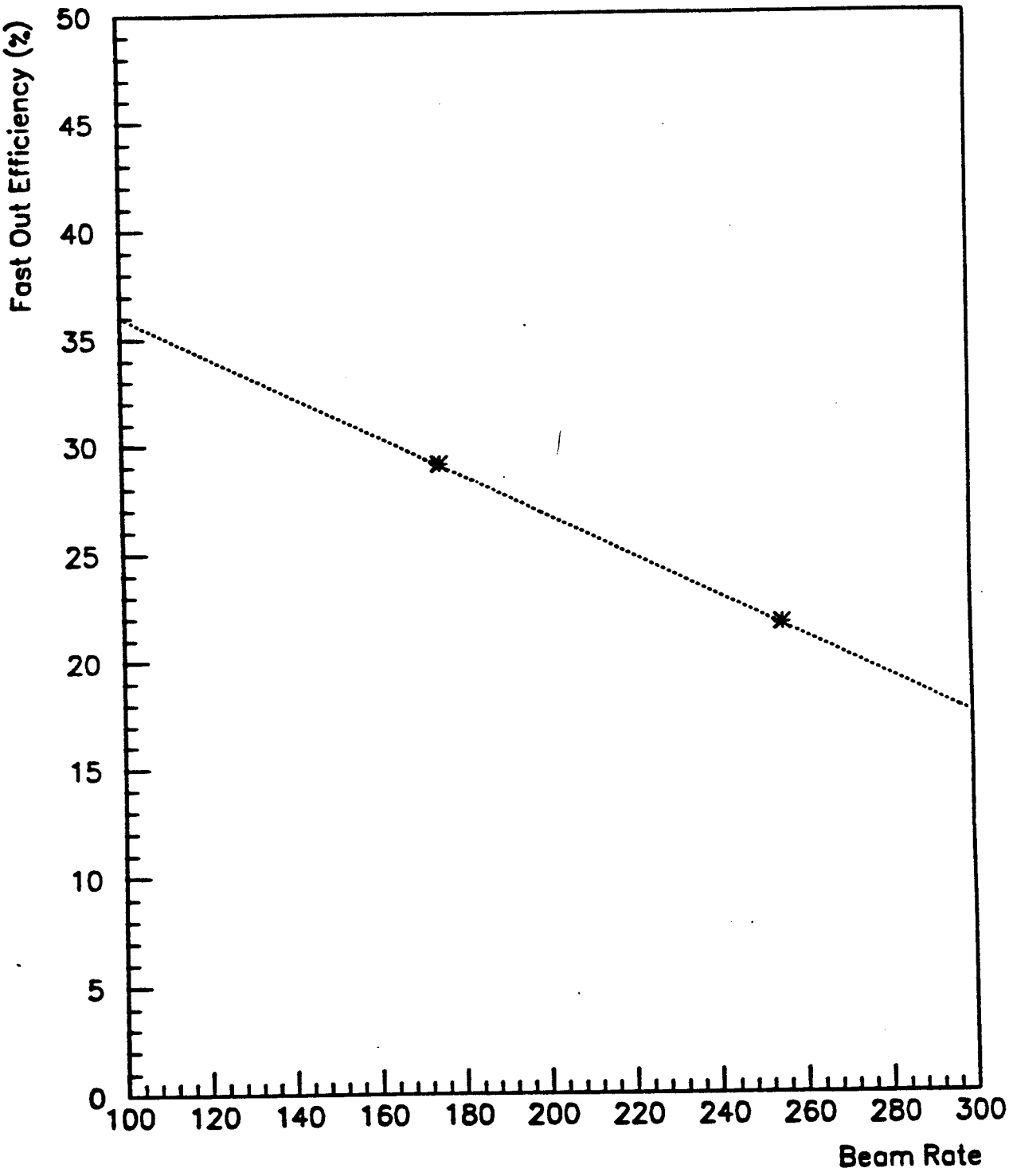

Figure V.4: Fast–Out efficiency as a function of beam rate.

Configuration	Slope±Error	Intercept±Error
35°	$-1.1\times10^{-3}\pm$ 10.5%	1.69±5.5%
45°	$-3.2\times10^{-5}\pm$ 8.5%	0.28±4.3%
65°	$-9.3\times10^{-4}\pm$ 9.6%	0.45±3.4%

Table V.1: Slopes and intercepts for the dependence of the Fast Out on beam rate.

chambers, which will decrease the FO efficiency. The second, is the fact that the true efficiency curve is unknown. In this experiment only two points of this curve are known. Let's imagine that the real efficiency curve looks like Figure V.5, where the Y axis is efficiency and the X axis is beam rate. In this experiment, if points 1 and 2 are measured and a line drawn through them, there is a specific slope and an intercept associated with this line. However, if points 1 and 3 are measured a different slope and intercept will be associated with the drawn line. Even though the same efficiency curve was used, because only two points are available at any one time, the slope and intercept are very different. This may seem to be a disaster, but it is not, because most of the runs were done at very similar beam rates as the FO efficiency runs, therefore only a small rate-dependent correction needs to be made.

E Multiwire–Proportional–Chamber Efficiency

The first factor ($\mathcal{E}_{trigger}$) of equation V.1 has been calculated. The following section will determine the second factor of this equation ($\mathcal{E}_{hits}$). This term corresponds to the efficiency of finding a track, given that the trigger was fired. To resolve a track, at least two planes from each wire chamber must have given a signal; if this does not occur, then even though there was a legitimate particle going through, its track will not be resolved, and the particle will be undetected.

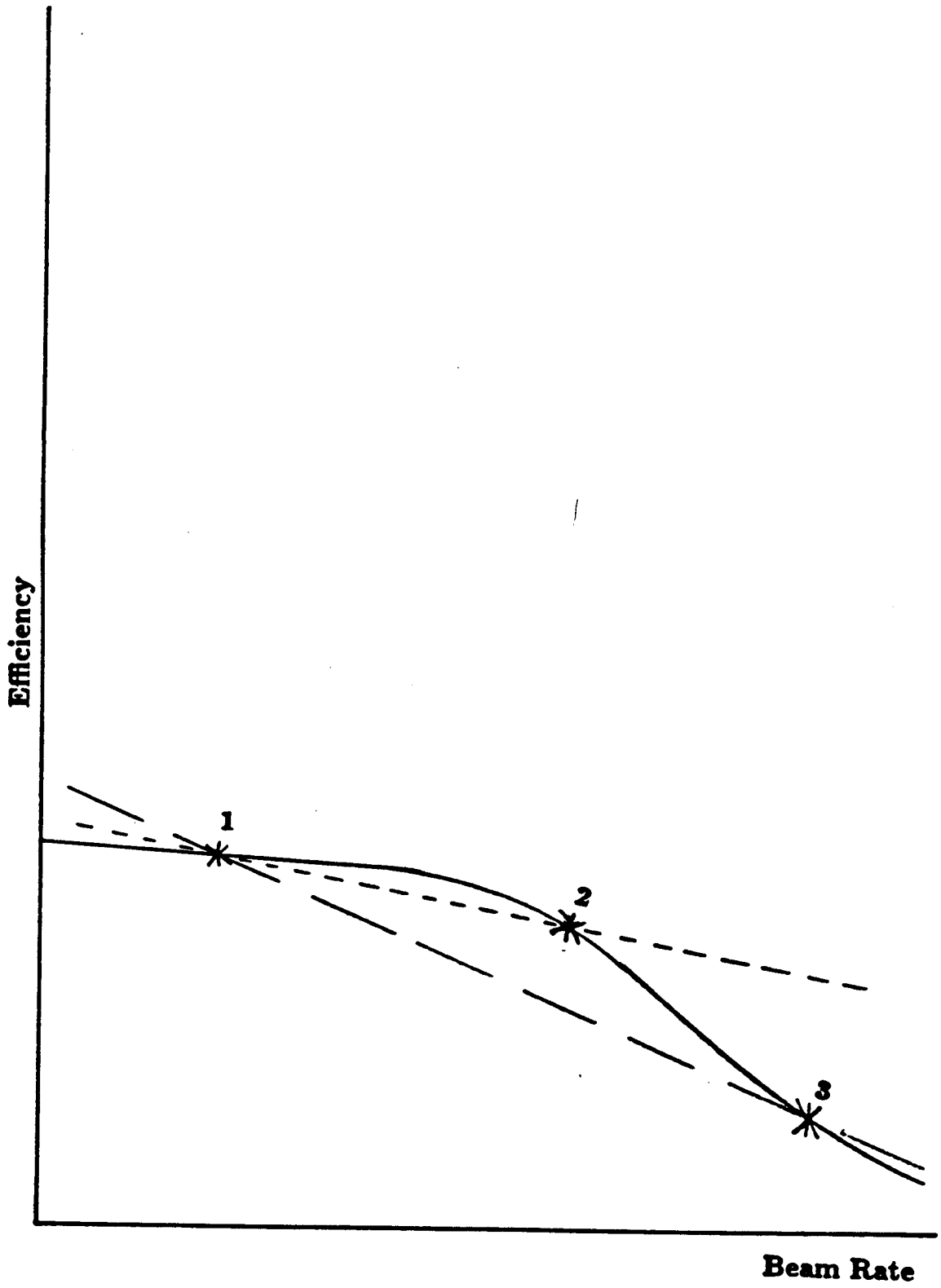

Figure V.5: A hypothetical curve of the Fast–Out efficiency as a function of beam rate.

A track is resolved if two planes out of three from each wire chamber fire. This means that the efficiency of finding a track, given that the trigger has fired ($\mathcal{E}_{hits}$) reduces to the product of the efficiency of the individual wire chambers.

$$\mathcal{E}_{hits} = \mathcal{E}_{mwpc_1}\,\mathcal{E}_{mwpc_2}\,\mathcal{E}_{mwpc_3}\,\mathcal{E}_{mwpc_4}\ , \tag{V.10}$$

where $\mathcal{E}_{mwpc_i}$ is the efficiency of the ith chamber. Finding the efficiency of each wire chamber then reduces to finding the efficiency of each plane of each wire chamber. The way in which the efficiency of each plane is recombined into the overall wire–chamber efficiency will be dealt with later.

To find the efficiency of each plane of wire chamber i, wire chamber i was removed from the Fast–Out. The efficiency of the first plane of wire chamber i would then be ($\mathcal{E}_{wp1_i}$),

$$\mathcal{E}_{wp1_i} = \frac{\#\text{ of tracks with 3 planes fired}}{\#\text{ of tracks with planes 2 and 3 fired}}\ . \tag{V.11}$$

The numerator of the fraction is equal to $R(\mathcal{E}_{wp1_i}\,\mathcal{E}_{wp2_i}\,\mathcal{E}_{wp3_i})$, while the denominator is $R(\mathcal{E}_{wp2_i}\,\mathcal{E}_{wp3_i})$, where $\mathcal{E}_{wp1_i}$,$\mathcal{E}_{wp2_i}$, and $\mathcal{E}_{wp3_i}$ are the efficiencies of the three planes for the ith chamber and R is some coefficient that embodies electronic effects. The value of R is irrelevant because it cancels out in equation V.11. This process can be repeated for each wire plane in each wire chamber. The efficiencies of each wire plane are listed in Table V.2. In this calculation there is the assumption that the plane efficiencies are uncorrelated. This is not necessarily true because of such things as quenching in the gas inside the wire chambers or power supply fluctuations. However, as can be seen from Table V.2 these effects are at the few percent level or less, which means that the assumption that the efficiencies of the planes are uncorrelated is acceptable.

Now that the efficiency of each wire plane is known, the efficiency of each wire chamber can be calculated. However, to find a track, only two out of three planes

	$MWPC_1$	$MWPC_2$	$MWPC_3$	$MWPC_4$
WP_1	0.932	0.946	0.965	0.941
WP_2	0.971	0.957	0.969	0.968
WP_3	0.929	0.788	0.969	0.943

Table V.2: Efficiency of each wire plane (WP) in each wire chamber (MWPC).

need to fire. This means that the efficiency of each wire chamber is slightly more convoluted than just the straight multiplication of the efficiency of each of its wire planes. The equation for the efficiency of a wire chamber is

$$\mathcal{E}_{wc_i} = A + B + C + D \tag{V.12}$$

where

$$A = \mathcal{E}_{wp_1}\,\mathcal{E}_{wp_2}\,\mathcal{E}_{wp_3}, \tag{V.13}$$

A is the probability that all three planes will fire. Also,

$$B = \mathcal{E}_{wp_1}\,\mathcal{E}_{wp_2}\,(1-\mathcal{E}_{wp_3})\ . \tag{V.14}$$

B is the probability that wire planes 1 and 2 will fire but not plane 3. Term C is the probability that wire planes 1 and 3 will fire but not plane 2.

$$C = \mathcal{E}_{wp_1}\,\mathcal{E}_{wp_3}\,(1-\mathcal{E}_{wp_2})\ . \tag{V.15}$$

Finally, term D is is the probability that wire planes 2 and 3 will fire but not plane 1.

$$D = \mathcal{E}_{wp_2}\,\mathcal{E}_{wp_3}\,(1-\mathcal{E}_{wp_1})\ . \tag{V.16}$$

Table V.3 shows the overall efficiency of each multiwire proportional chamber.

The final value calculated for $\mathcal{E}_{hits}$ (equation V.10) was found to be (95.3±0.6)%.

Wire Chambers	Efficiency (in %)	Errors (in %)
$MWPC_1$	99.3	$\pm$ 0.2
$MWPC_2$	97.0	$\pm$ 0.5
$MWPC_3$	99.7	$\pm$ 0.1
$MWPC_4$	99.2	$\pm$ 0.1

Table V.3: Overall efficiency of each of the four wire chambers (MWPC).

F Overall Efficiency

There is one other efficiency which must be taken into account, the software efficiency. This is discussed in Appendix A. At this point $\mathcal{E}$, the efficiency of the spectrometer (equation V.1) can be calculated, and the cross sections can then be corrected for the inefficiency of the spectrometer. The next chapter deals with the final calculations needed to obtain these cross sections.

Chapter VI

Results

A Target Frame of Reference

The p–like cross section is calculated as

$$\frac{E}{p^2}\frac{d^2\sigma_{inc}}{dpd\Omega} = \sum_{i=1}^{n} Z_i\, A_i^2\, \frac{E_i}{p_i^2}\frac{d^2\sigma_i}{dp_i\, d\Omega_i}\ , \qquad \text{(VI.1)}$$

This is just a repeat of equation II.5, except for the definition of the Lorentz invariant cross section ($d^2\sigma/dpd\Omega$). The $d\Omega$ does not represent the spherical coordinate equivalent $sin\theta\ d\theta\ d\phi$. In this experiment, the emission of fragment is assumed to be azimuthally isotropic. When the data is presented, it is as a $d\theta$ which has been integrated over $d\phi$, meaning that $d\Omega$ only represents $sin\theta\ d\theta$. For the moment let's ignore the sum in equation VI.1 and look at how the various terms are calculated. The practical equation becomes

$$ZA^2\frac{E}{p^2}\frac{d^2\sigma}{dp\, d\Omega} = Z\frac{(\frac{E}{A})}{(\frac{p}{A})^2}\frac{(\frac{N_{track}}{N_{beam}}) - (\frac{N_{back\ track}}{N_{back\ beam}})}{t\,\rho\,\frac{\Delta p}{A}\,\Delta\Omega}F, \qquad \text{(VI.2)}$$

where Z and A are the charge and the mass number of the particle, respectively. These two terms take into account the number of protons in a fragment, plus the momentum and energy distribution for each nucleon in that fragment. As an example, take a

^{4}He with momentum of 2 GeV/c (total energy of 4.2 GeV). It is assumed that each of the four nucleons in the ^{4}He will contain both a fourth of the momentum and a fourth of the energy, 0.5 GeV/c and 1.05 GeV respectively. This is the reason that the momentum and energy terms in equation VI.2 are divided by the mass number. In this ^{4}He there are two protons and two neutrons; however, only the two protons are of interest and this is where Z comes in, meaning that this ^{4}He will be counted as two protons with 0.5 GeV/c momentum and 1.05 GeV energy. The t term is the thickness of the target, a value that had to be estimated using Monte Carlo simulations (see Appendix A). The factor ρ is the density of the target. One cannot just take the density of lanthanum from a handbook. The problem is in the preparation of the target; depending on whether it has been rolled or electrodeposited, the density will be different. The density was measured to be 6.09 gm/cm^3. The F term in equation VI.2 is

$$F = \frac{M_{La}}{N_A}\mathcal{E}\ , \tag{VI.3}$$

where $\mathcal{E}$ is the efficiency of the spectrometer, obtained as described in the previous chapter, and M_{La}/N_A is the molecular weight of lanthanum divided by Avogadro's number.

The rest of the terms in equation VI.2 are related to bins, so a short explanation is necessary. Once a particle's momentum and acceptance are identified, it is placed inside a bin that corresponds to a momentum and angular range. The bin in momentum is 80 $\frac{MeV/c}{A}$ wide, for $\Delta p/A$, and the bin is 2° wide. $\Delta\Omega$ is the acceptance of the bin, and Appendix A explains how this number is obtained. E/A and $(p/A)^2$ are the energy per nucleon and the momentum per nucleon squared, respectively, of the specific bin at which one is looking. Each time a particle falls within a bin, the number in that bin increases by one. When all the particles have been processed, the number one gets is N_{track}, for a specific bin. N_{track} is then divided by N_{beam},

which corresponds to the number of incident beam particles. This is obtained from the beam counter, which was discussed in Chapter III.

The next problem which is encountered is the fact that the beam and the air will produce real particles which can go through the spectrometer. This background needs to be subtracted. Several runs were performed without the target, which gave us the background subtracted in equation VI.2 as $N_{back\,track}/N_{back\,beam}$. $N_{back\,track}$ is the number of tracks found in a bin for the background run and $N_{back\,beam}$ is the number of beam particles obtained from the beam counter for that background run.

B Projectile Frame of Reference

As was mentioned previously, in order to obtain the 20°, p–like cross sections, one had to transform into the projectile frame. The problem which arises from this is that the acceptance ($\Delta\Omega$) was determined in the target frame. This means that the transformation of a bin from the target frame to the projectile frame is by no means an easy task. In order to avoid possible mistakes which may occur during this transformation, a slightly different approach was taken. The process of determining the cross section in the projectile frame is effectively the same except for N_{track}. The acceptance is determined for each individual particle instead of determining it for the bin. The particle's values (energy and momentum) are transformed into the projectile frame and then binned. The Lorentz transformations used can be seen in Appendix B. When a particle falls within a bin, N_{track} is not increased by one, but by $1/\Delta\Omega$. This effectively weights each particle by its acceptance. This is also done for the background runs, so $N_{beam\,track}$ is also a sum of weights. The resulting equation is

$$ZA^2\frac{E}{p^2}\frac{d^2\sigma}{dp\,d\Omega} = Z\frac{(\frac{E}{A})}{(\frac{p}{A})^2}\frac{(\frac{N_{track}}{N_{beam}}) - (\frac{N_{back\,track}}{N_{back\,beam}})}{t\,\rho\,\frac{\Delta p}{A}}F, \qquad \text{(VI.4)}$$

where all the terms have the same meaning as previously except for N_{track} and $N_{beam\ track}$.

This same process can also be done in the target frame, and, if everything is done correctly, the two methods should reproduce each other. The difference between these two methods turned out to be about 0.5%.

Something else which needs to be mentioned is that the energy of each particle needs to be corrected for the energy loss in the target, which is done by assuming that the particles start in the middle of the target. This is a very small fraction (4% to 0.02%, energy loss is a function of momentum), but since it is not a complicated thing to do, it was done.

C Results and Errors

All the numerical data which will be presented in the following subsections are also given in tabular form in Appendix C.

In order to show that the normalization of the 35° and 45° configurations is correct, a comparison of the cross sections at 40° obtained from the 35° configuration with the 40° cross sections obtained from the 45° configuration should reproduce the same curve (Figure VI.1). As can be seen, the cross sections agree with one another within systematic error. These errors will be discussed further in subsection 3. The reason a similar plot of the 45° and 65° configurations is not shown is due to the fact the angular overlap between these two was not enough. The problems of this region are discussed more extensively in subsection 3.

Now various results will be shown. The first (Figure VI.2), shows the cross sections for the 40° and 60° angles. These results will be compared to both the previous data

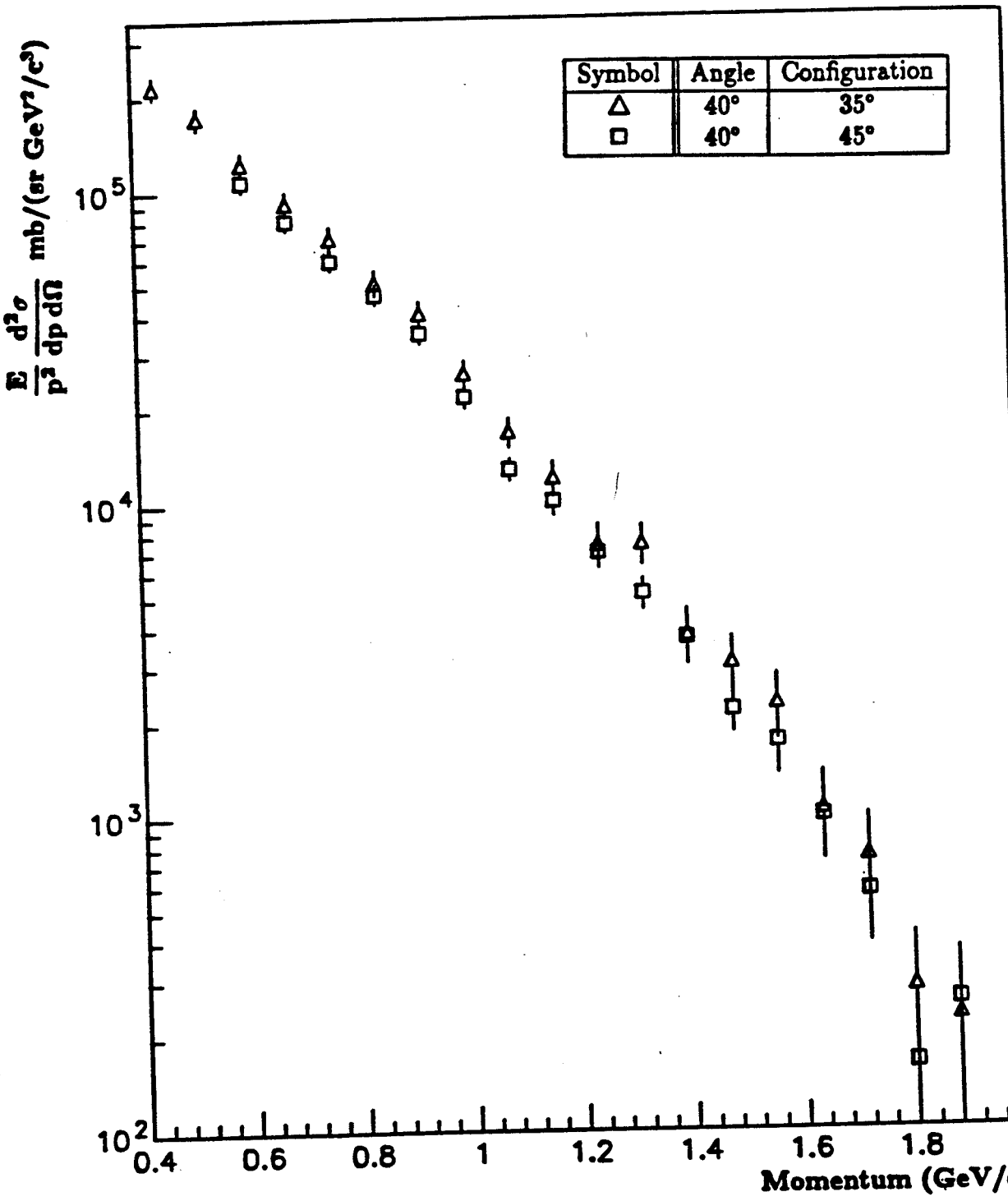

Figure VI.1: Production cross sections for p-like particles at 40°. The triangles are the cross sections from the 35° configuration, while the squares are the cross sections from the 45° configuration.

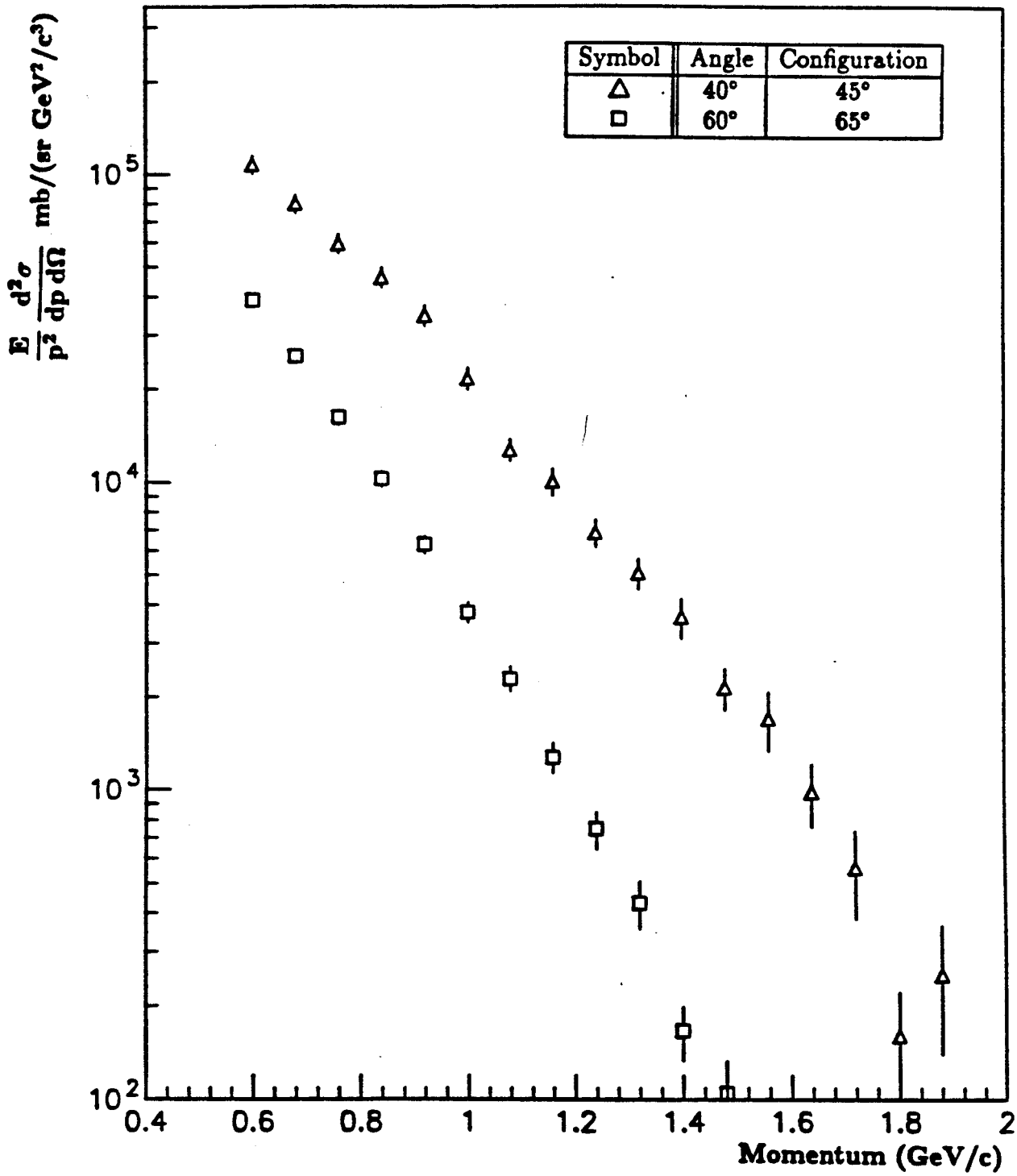

Figure VI.2: Production cross sections for p–like particles at 40° and 60°.

and the theory in the following sections.

Figure VI.3 shows the cross sections obtained for the 20° data; the errors bars are statistical. Systematic errors are discussed latter on. Each symbol on Figure VI.3 represents the particular configuration from which the data were obtained.

The data that were available also allowed the measurement of the cross sections at a 15° lab angle, also shown in Figure VI.3; however, this is at the edge of the geometrical acceptances, so the error bars are large.

1 Comparison to the Previous Data

The results most easily understood are the comparisons of production cross section versus momentum at 20°, 40°, and 60° (Figure VI.4) between the results from this experiment and Hayashi *et al.*'s results.

As can be seen from Figure VI.4 the results of Hayashi *et al.* cover a much wider momentum range. A quick discussion of their experiment is in order [Haya88]. They used a magnetic spectrometer with small acceptance ($\approx$ 0.01 sr) and a series of wire chambers and scintillators. The whole setup was on a rotating table which allowed them to measure lab angles directly. By varying the field strength in the magnet they were able to focus on small ranges of momenta. In this way they were able to measure angular ranges from 89° to 20° directly, and momenta ranges from 0.25 GeV/c to 2.0 GeV/c for particles ranging from pions to ^{4}He.

Something which needs to be mentioned is that Hayashi *et al.* presented individual particle cross sections only [Haya88] from which the proton–like cross sections have been inferred. The Hayashi *et al.* data presented in Appendix C are the inferred results.

At 40° and 60° the present results agree with the previously measured cross sec-

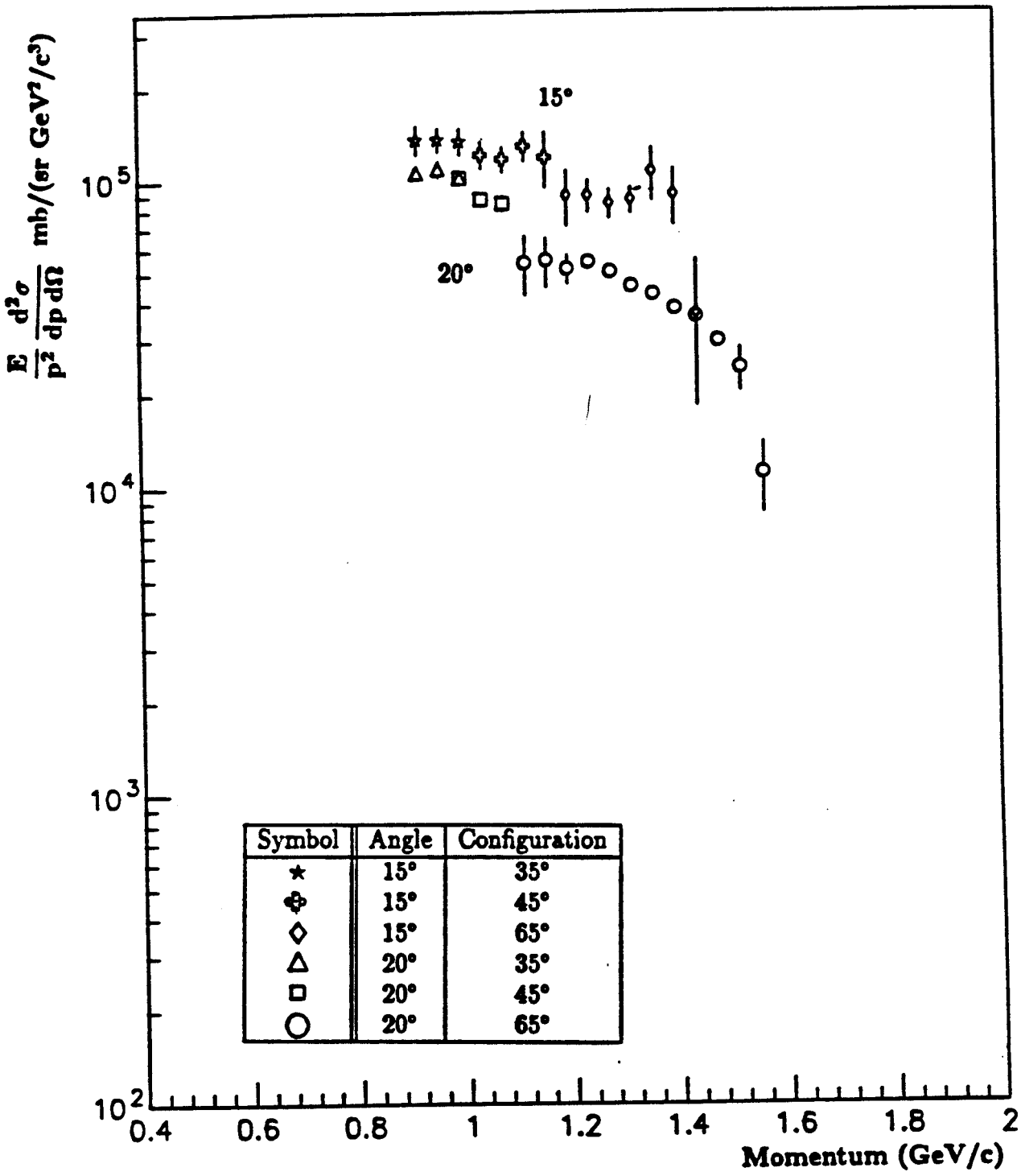

Figure VI.3: Production cross sections for p–like particles at 15° and 20° obtained from the three magnet–target configurations.

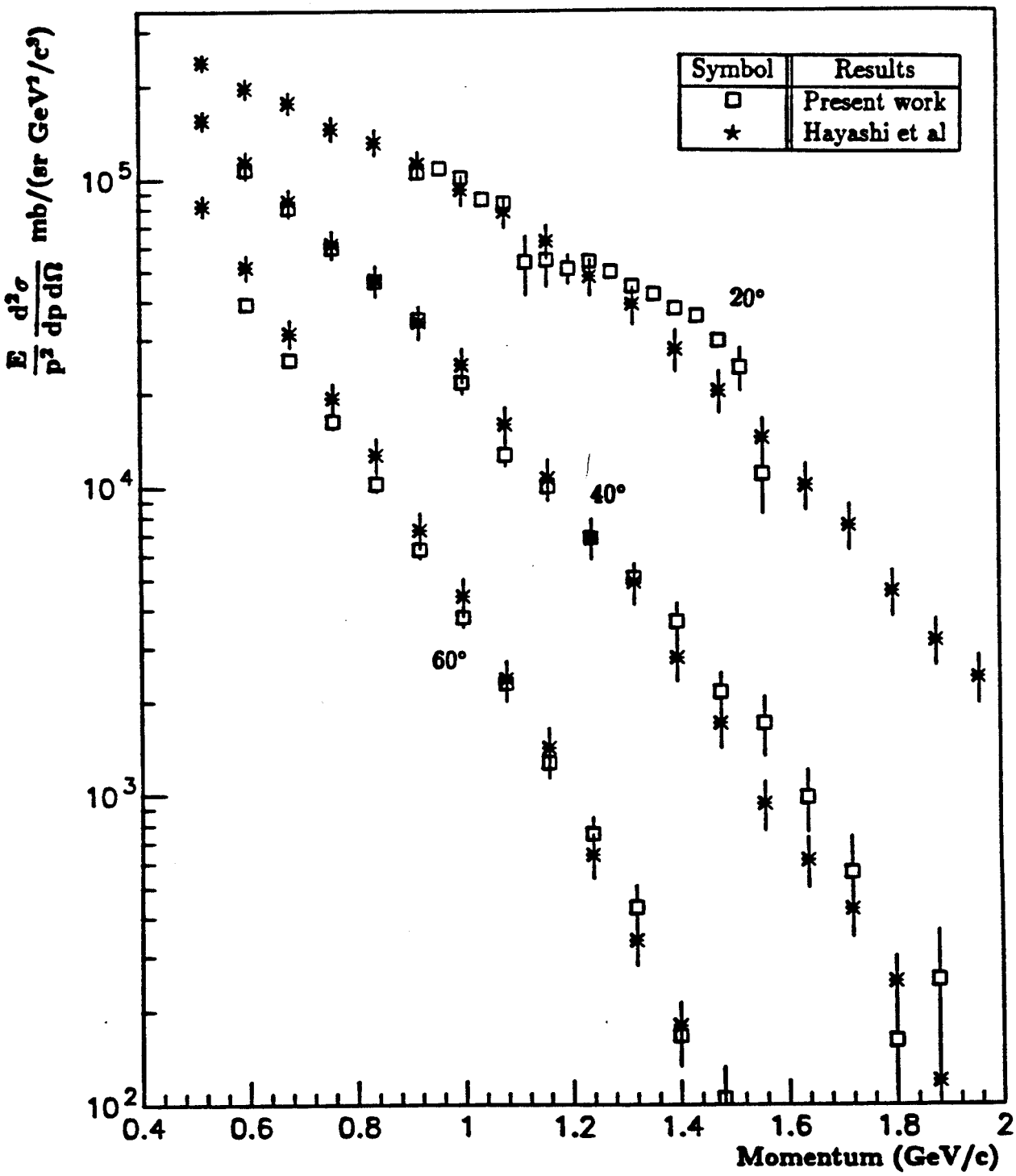

Figure VI.4: Comparison of the p–like production cross sections at 20°, 40°, and 60° . Hayashi's error bars encompass both statistical and systematic error. The error bars shown for the present experiment are statistical only.

tions of Hayashi *et al.* At 20°, where the largest discrepancy was observed between the theory and the experimental results, the present data seem generally to agree with the previous results. Even though part of the present cross sections may seem to be higher, the results agree within systematic errors; these errors will be discussed in subsection 3. One might be tempted to conclude that the error is not in the previous data of Hayashi *et al.*, and that therefore the error lies in the theoretical models. However, this conclusion is premature. Between the Bevatron and the experimental area the operators placed scintillators and other material in the beam line in order to monitor it. This degraded the beam from 0.8 GeV/n to 0.76 GeV/n for Hayashi *et al.* [Jian91] and to about 757 MeV/n for this experiment. This includes the energy loss of the beam through half of the target thickness. The theoretical models were calculated assuming 0.8 GeV/n. This means that the comparison between theory and experiment is not a legitimate one. This was first suggested by Jiang *et al.* [Jian91] in 1991 as the possible explanation for the discrepancy.

2 Comparison to Theoretical Calculations (VUU)

The VUU theory code was rerun ([Batk92], [Cass90]) at a beam energy of 757 MeV/n, in order to compare to the data obtained for this experiment. The values of A, B, and α inputed for the mean field (equation II.4) were -143.3, 167.9, and 4/3, respectively. This corresponds to a compressibility K of 238 MeV. Figure VI.5 shows the comparison of the present results and the ones obtained from the VUU theory model at a beam energy of 757 MeV/n for the 15°, 20°, 40°, and 60° cross sections.

The cross sections at 40° and 60° are well reproduced; however, the VUU model seems to overpredict the cross sections at 15° and 20°. This overprediction is better seen in Figures VI.6 and VI.7. It seems that the discrepancy is slightly worse at smaller angles, although this is somewhat of a judgment call because of the raggedness

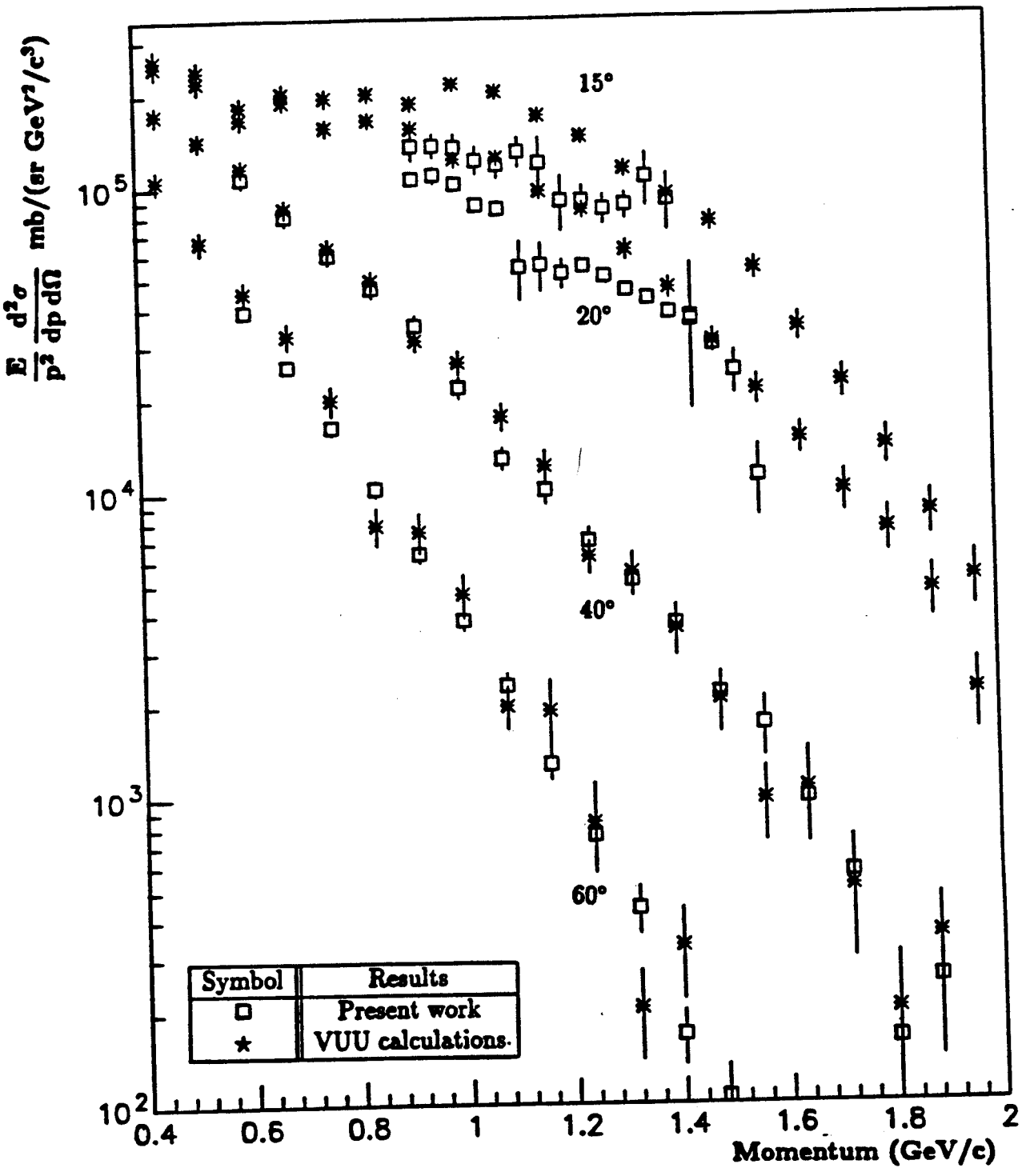

Figure VI.5: Comparison of the p–like production cross sections at 15°, 20°, 40°, and 60° from the present results and the VUU model.

of the information available at 15°.

Since the present results confirm those of Hayashi *et al.*, it would be interesting to compare their results with the VUU model (Figure VI.8). Again, at 40° and 60° the model reproduces the cross sections, while at 20° the model is systematically higher, even after taking into account the energy loss of the beam.

The discrepancy between theory and data has decreased since the first comparison (Figure I.1). Since there are various methods available to obtain cross sections from the VUU codes, it is important to specify the method used in this case. The VUU code produced a phase–space distribution of particles as a function of impact parameter. From these distributions, multiplicities at various momenta and angles were calculated, still as a function of impact parameter. In the next step the probability of an impact parameter was folded into the multiplicities, which gives the final distribution, again as a function of impact parameter. This last distribution was integrated over impact parameter to obtain the final cross sections. A numerical integration was used; the specific integration is a higher order Simpson's method called Bode's rule [Koon86]. This method overestimates the cross sections by about 4% by comparison to a Gaussian, which is not enough to account for the discrepancy.

3 Errors

There are two types of errors involved, statistical and systematic. The next subsections will deal with each of these individually.

Systematic Errors

Table VI.1 shows the systematic errors involved with each part of the spectrometer. Combining all the errors in quadrature, one gets an overall systematic error of 12%.

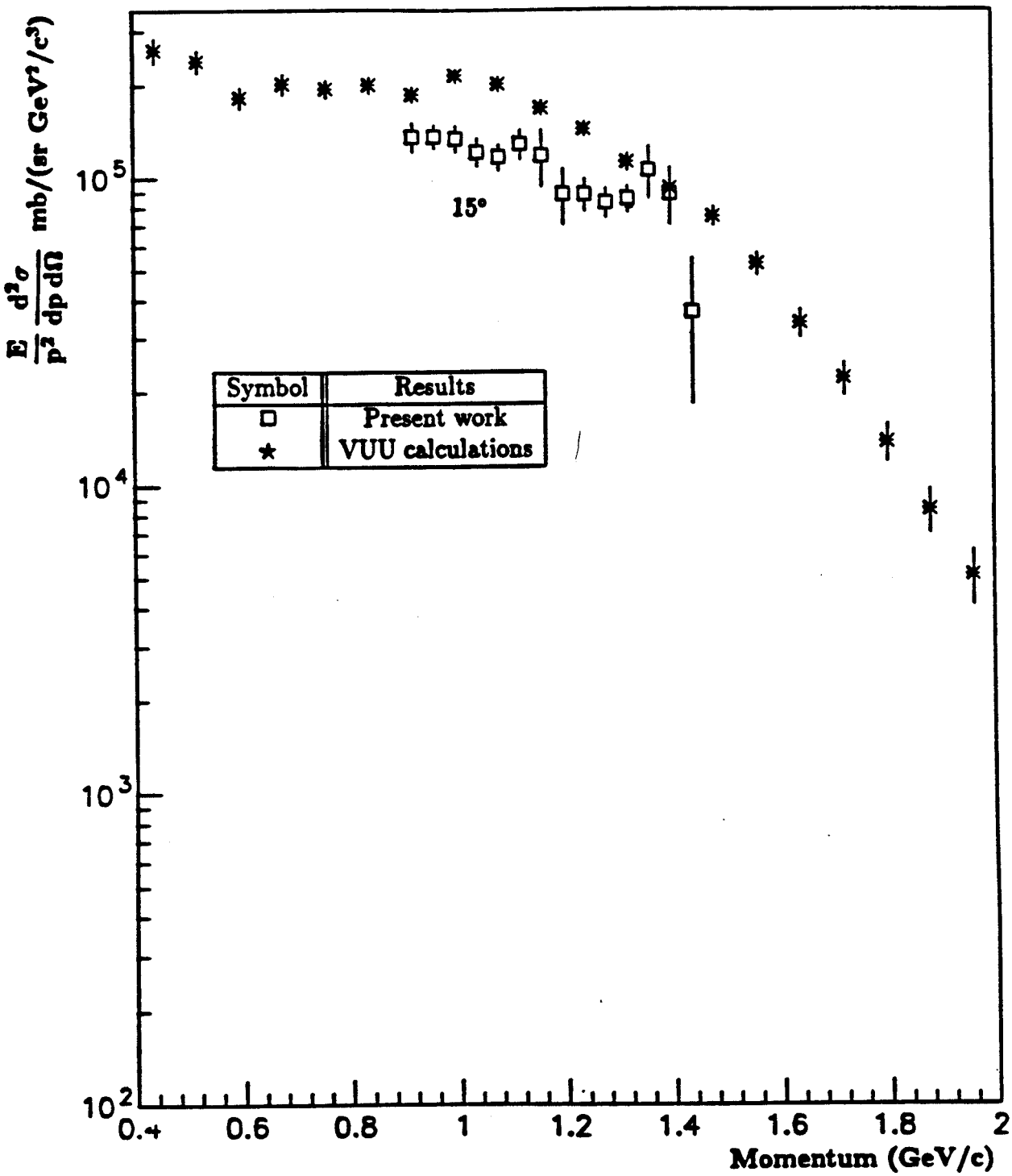

Figure VI.6: Comparison of the p-like production cross sections at 15° from the present results and the VUU model.

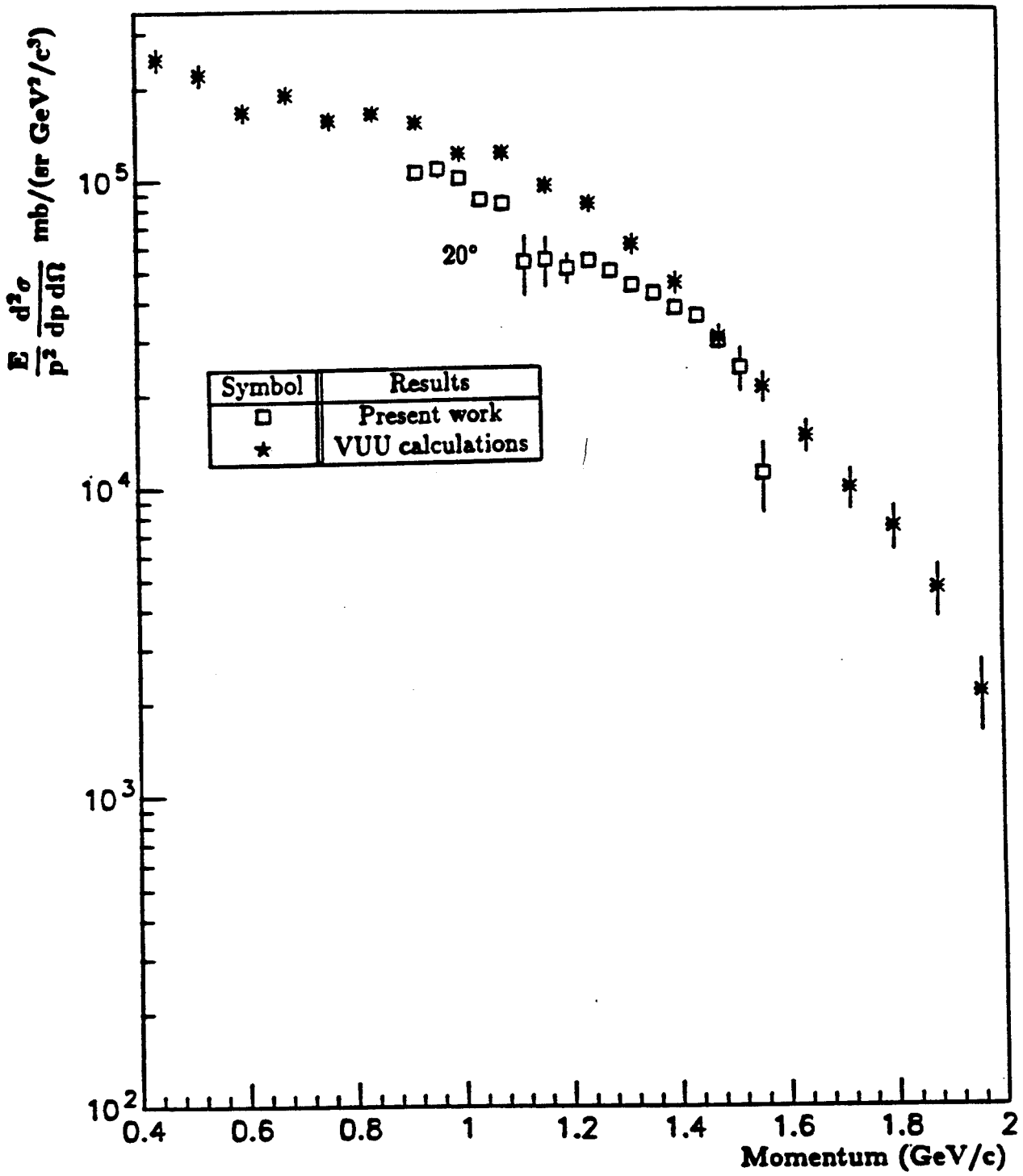

Figure VI.7: Comparison of the p-like production cross sections at 20° from the present results and the VUU model.

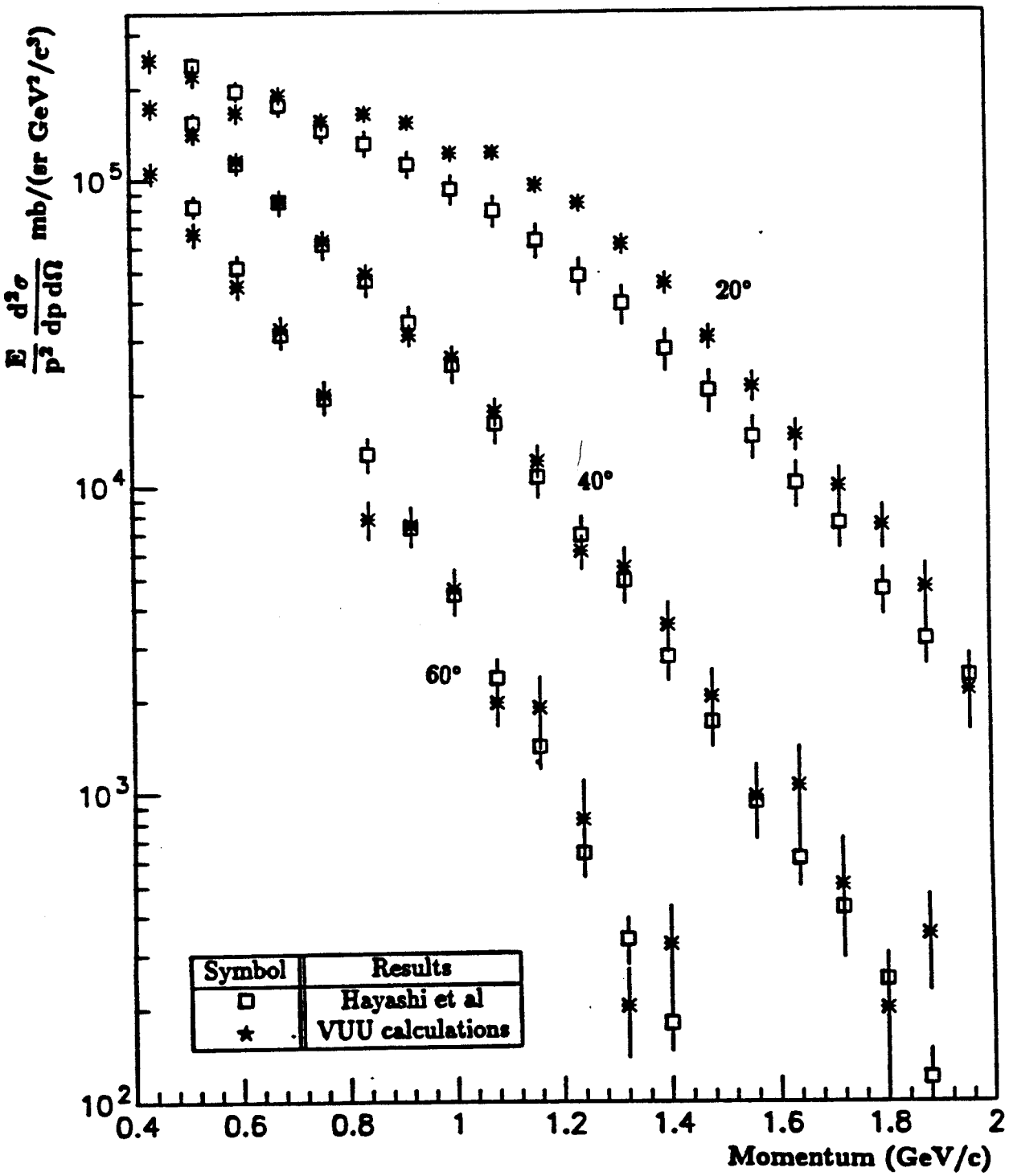

Figure VI.8: Comparison of the p–like production cross sections at 20°, 40°, and 60° from Hayashi *et al*'s results and the VUU model.

Component	Systematic Error (%)
Π	0.04
S	0.20
MWPC 1	0.17
MWPC 2	0.50
MWPC 3	0.11
MWPC 4	0.12
IC2 Calibration	0.8
$t\rho$	4.3
Particle Misidentification	≤ 1
Acceptance	4.25
Fast Out	10.

Table VI.1: The systematic errors associated with each component of the spectrometer.

This systematic error is not quite the same for each of the three configurations because the Fast–Out error varies from configuration to configuration. However, the errors themselves have 10% uncertainties; so, assigning a 10% error to the Fast Out for all three angles is acceptable. One thing which should be mentioned is that the systematic errors from one configuration are independent of the other configurations, therefore, the systematic error may move the data from the 35° configuration of Figure VI.3 up, while moving the data from the 45° configuration down. The $t\rho$ term in Table VI.1 needs a small explanation: there is an error of 0.75% in the combined physical measurement of target thickness t and target density ρ. However, there is also a 4.2% uncertainty in the Monte Carlo simulation of the target thickness. Combining these two errors in quadrature one gets 4.3%.

Statistical Errors

The statistical error was calculated using

$$\sigma = C\sqrt{\sum_{j}^{n}(w_j^2 + \sigma_{w_j}^2)}\ , \tag{VI.5}$$

where C is a multiplication factor. This factor encompasses all the factors used in equations VI.2 (target thickness, density, efficiencies, etc.), w_j is the weight of each event (which turns out to be $1/\Omega$), and σ_{w_j} is the error in the weight. The error in the weight, which is the error in the acceptance, was calculated by measuring the error in the Monte Carlo acceptance at a variety of angles. In the central part of the spectrometer the error is roughly 4%, while at the edges the error becomes drastically larger. This translates to the large error bars seen at the edge of the 65° configuration data set in Figure VI.3. Actually, all edges of the three data sets have similar large error bars, but since there was sufficient angular overlap between the data from the 35° configuration and the 45° configuration, the points with these large error bars were dropped. There was not enough angular overlap between the data from the 45° configuration and the 65° configuration; the points which do exist are the ones at the edge of the acceptance, and therefore, the error bars are large.

The large error at the edge of the acceptance results from the inaccuracy of the simulation. At the edge of the acceptance, whether a particle is accepted in the spectrometer or not depends on the position from which it started on the target. The starting position of the particle is, of course, beam–spot size dependent. Since each run had slightly different beam–spot sizes, it was not possible to simulate each one exactly; therefore, the edge of the acceptances are not as well known.

If the probability of a particle making it through the spectrometer depends on the starting position on the target, an interesting problem arises in the determination of the target thickness. In Appendix A the target thickness is determined as an average

over the whole beam spot; however, those particles which are position sensitive will come from one specific position on the target, which may have a different target thickness than the average value. This means that the bins at the edge of the 65° configuration were calculated using an inaccurate target thickness.

Another error is caused by the beam–spot size dependence. A real particle which traverses the spectrometer may have a Monte Carlo acceptance value of 0 because the Monte Carlo did not simulate its starting position on the beam spot. When this particle is transformed into the projectile frame and falls into one of the bins, it is discarded because there is an infinite weight attached to this particle (remember the weight for a particle is $1/\delta\Omega$). In the outer bins about 10% of the particles are thrown away because of this. This will have a net effect of decreasing the measured cross sections. Because in reality the acceptance is very small, the weight of this 10% corresponds to more than 10% of the cross sections; estimating the real amount would involve simulating each beam spot for each run. The cross sections in Figure VI.3 from the edge of the 65° configuration have not been corrected for this, nor do the error bars include this effect.

D Conclusion

The production cross sections for p–like particles from 757 MeV/n La on La collisions were measured. The results obtained in this experiment agree with the previously measured data by Hayashi *et al.* (Figure VI.4). Also, the data agree with the theoretical models at the larger polar angles; however, the discrepancy originally observed at the smaller angles is still present but decreased once the smaller beam energy was taken into account. Since the cross sections are overpredicted at the lower angles, they may be underpredicted some place else; it would be interesting to find out where. If

the cross sections are not underpredicted anywhere, the problem may just be one of normalization. Another possibility is that there is a physical effect which is not being taken into account.

There are a few things which could be done to reduce the error bars, such as a more extensive study of the beam rate dependence on the efficiency of the Fast Out. Further testing of the theoretical models could be done by varying the beam energy from, for example, 400 MeV/n to 1.3 GeV/n for a La beam. This unfortunately will not be performed at LBL because of the likely shutdown of the Bevalac.

Appendix A

Monte Carlo Simulation

A Introduction

A Monte Carlo simulation had to be developed for the following reasons: first, to measure the efficiency of all the software; second, to correct for the effective–edge calculation of the rigidity; third, to measure the acceptance of the spectrometer; and fourth, to estimate the average thickness of the target. Each of these things will be explained in the following sections. However, first a discussion of Monte Carlo simulations is necessary.

B Basic Method

A Monte Carlo simulation is nothing more then just trying to replicate series of events as closely as possible; these can be any events such as various sized balls falling from a roof, football scores, a chemical reaction, particle decay, and so on. These simulations are accomplished by a random sampling method. A number from 0 to 1 (or any other range) is chosen, which is then assigned to represent some variable. In the case of the falling ball, a small range in the random number (e.q. 0.1 to 0.2) may represent its mass. As another slightly more complicated example, let's try to predict the fraction of particles with a half life t_1 and with a range of momentum from A to B one would

observe after they had gone thru a 100 meter tube. The simulation would start by taking a random number and assigning it to the momentum. The time for this particle to travel the tube can then be derived. The next step is to figure out the fraction of particles which survive after this amount of time, this is done with

$$\frac{N}{N_o} = e^{-kt}, \tag{A.1}$$

where N and N_o are the present number of particles and the starting number of particles, respectively, k is the decay constant, and t is the time. Now a random number is chosen again, if it is less then or equal to the above fraction, then the particle made it through the 100 meter tube. This method has to be repeated many times in order to obtain the average that would be observed.

Obviously, extensive calculations will require many random numbers and would become very bothersome to perform by hand. This is where computers come in. The computer will create a random number which will be assigned to a variable, in our case, for example, as the momentum of a particle or the energy loss of a particle in some substance. This is the basis of the Monte Carlo method, the use of random numbers as physical variables.

In this experiment the computer was given the shape and materials of the various parts of the Janus spectrometer. The various physical processes were then simulated, such as energy loss in various materials, scattering, and absorption. To program all of this into the computer correctly would take several years. Since simulations are very important for these kinds of experiments, a software package called GEANT [Brun86] has been developed by a group of physicists. GEANT allows one to tell it the shape and materials of the various parts of the spectrometer, and by a series of flags, one can tell GEANT which physics should be performed on which type of particles. GEANT also allows one to tell it the position and components of the magnetic fields; through

this option the real field map of the Janus magnet was entered into the simulations. The rest is then taken care of by the software.

C Software Efficiency

The first thing mentioned at the beginning of this appendix was the efficiency of the software. Once the track–finding software has been produced, it is important to know how well it works, i.e. its efficiency. The efficiency can be estimated by simulating a large number of tracks and the wire numbers which accompany these tracks, then asking the software to find these tracks using the wire numbers. During the experiment some of the wires in each of the four wire chambers were either dead or partially working. This effect can also be incorporated into the simulation. It turns out that the software is 99.3% efficient at finding tracks.

D Geometrical Acceptance

Geometrical acceptance refers to the geometrical space which the particles will be able to traverse and be detected in the spectrometer. Under normal circumstances, if the center of a sphere is known and a small area is taken at some distance R, it is simple to figure out the percentage of the sphere this small area occupies. However, outside of the magnet the magnetic field is non–uniform, which causes effects such as vertical focusing. For a low–momentum particle this is a significant effect, whereas at high momentum the effect is much less pronounced, complicating the geometrical acceptance. It would be an incredible chore to calculate the geometrical acceptance of each particle, depending on its momentum and angle of ejection. To solve this problem, a Monte Carlo method was again used. The spectrometer was simulated as well as possible in software. Simulated particles were then tracked through the

spectrometer at specific angles and momenta. The number of particles which traverse the spectrometer successfully will reveal the acceptance of the spectrometer at the specific angles and momenta. If 3000 particles were sent into the spectrometer over a solid angle of 0.05 steradians and only 2000 were detected, the acceptance of the spectrometer is $\Omega = (2000/3000)\,0.05 = 0.033$ steradians. This procedure had to be done for various particle types and the three angle/target configurations (Figure III.8). The acceptance was then folded into the cross sections. The way in which this was accomplished is explained in Chapter VI.

E Principal Component Analysis and Chebyshev Polynomial Fit

The effective edge approximation was very effective in finding tracks and determining the rigidity of these tracks; however, this approximation can cause a $\pm$ 5% error in the momentum. This error can be corrected by using a combination of "principal component analysis" [Wind83] and Chebyshev polynomials.

A particle with a specific momentum will fire a specific set of wires in each of the wire chambers. In essence the Chebyshev polynomials connect the twelve fired wires to a momentum. In order to do this the coefficients of the polynomials must be determined, which can be accomplished with computer simulations. In the simulation both the initial momentum and the twelve wires are known, so one can produce the coefficients which will connect the twelve wires to the momentum. Once the coefficients are known, the real data (the twelve wires) can be plugged in and the expected value of momentum can be obtained. This then allows us to correct the effective edge momentum.

The above is an over-simplification compared to what was actually done. It

Angular configuration	Acceptance Range	Target Angle	Target Thickness (cm)
35°	30° - 43°	32.5°	0.096
45°	37° - 54°	46.5°	0.118
65°	50° - 80°	25.5°	0.090
65°	50° - 80°	45.0°	0.115

Table A.1: The angle and effective thickness of the target in the various configurations of the spectrometer.

is possible to reduce the twelve–dimensional fit to a five–dimensional one. Given the initial position (X,Y) at the target and the three momentum components, one can predict the particle path. So, with five pieces of information (five degrees of freedom) one can predict almost everything about the track (this is not entirely true due to effects such as scattering or decay). This means that, although one may have twelve measured variables, only five independent variables describe the track. Using a method called "principal component analysis," the problem was reduced from twelve to five dimensions, using a computer code called ERIKA written by H. Von Fellenberg of SIN now PSI. These reduced dimensions are then fit to the Chebyshev polynomials.

F Target Thickness

The target was placed at a variety of angles, depending on the rotation of the magnet. The reason for this was to minimize the amount of material that a particle had to go through once it was formed. Table A.1 lists the target angles for the various magnet configurations. The target angle (θ) is the angle between the incoming beam and the target (Figure III.3). The fact that the target is at an angle to the beam means that the beam will traverse a longer distance through the target compared to when

the target is perpendicular to the beam. The effective thickness follows a $1/sin\theta$ dependence. Under normal circumstances the target thickness would now be known; however, there was some curvature to the target. Depending on the position of the beam, the average path length through the target could vary. This problem was resolved by using a Monte Carlo method. The curvature of the target was measured, and the beam position for each experimental run is known. This information, plus the target angle, was programmed into the computer, and 10,000 particles were randomly thrown at the simulated target within the beam spot, and the path length through the target was calculated. An average value was then determined, and this was used as the target thickness, shown in the third column in Table A.1.

Appendix B

Lorentz Transformations

The energy and momentum transform as follows (see for example [Grif87])

$$\begin{aligned} E' &= \gamma\,(E - \beta\,p_z) \\ p'_z &= \gamma\,(p_z - \beta\,E) \\ p'_x &= p_x \\ p'_y &= p_y \end{aligned} \tag{B.1}$$

Here E, p_x, p_y, and p_z are the energy and the three momentum components. The prime indicates the projectile frame, while the nonprime variables are in the target frame. γ and β are

$$\begin{aligned} \beta &= \frac{v}{c} \\ \gamma &= \frac{1}{\sqrt{1-\beta^2}}\ , \end{aligned} \tag{B.2}$$

where v is velocity.

The first step is to calculate γ and β. This can be accomplished by using the relationships

$$\begin{aligned} E &= \gamma\,m\,c^2 \\ \gamma &= \frac{E}{m\,c^2}\ , \end{aligned} \tag{B.3}$$

where E is the mass of the projectile plus its kinetic energy, and m is the mass of the projectile. Both the mass and the kinetic energy of the beam are known, so γ can be calculated; using the second part of equation B.2, β can be derived.

Now one can go back to equation B.1 and calculate what the energy and momentum would be in the projectile frame for each of the individual particles.

Appendix C

Tables

The data presented in the following tables are the results from the present experiment (Tables C1, C2, C3, and C4), inferred results Hayashi *et al.* (Tables C5, C6, and C7), and the VUU calculations [Batk92] (Tables C8, C9, C10, and C11). All the cross sections listed below are in units of [mb/(sr GeV^2/c^3)]

Momentum (GeV/c)	(p–like cross sections ± Statistical Error)$\times 10^5$
0.92	1.35 ± 0.15
0.96	1.35 ± 0.12
1.00	1.33 ± 0.13
1.04	1.20 ± 0.13
1.08	1.15 ± 0.11
1.12	1.27 ± 0.14
1.16	1.17 ± 0.25
1.20	0.88 ± 0.18
1.24	0.88 ± 0.11
1.28	0.829 ± 0.091
1.32	0.853 ± 0.084
1.36	1.06 ± 0.21
1.40	0.89 ± 0.19
1.44	0.36 ± 0.18

Table C.1: Invariant cross sections as a function of momentum at 15° from the present results.

Momentum (GeV/c)	(p–like cross sections ± Statistical Error)$\times 10^5$
0.92	1.052 ± 0.053
0.96	1.081 ± 0.070
1.00	1.013 ± 0.043
1.04	0.856 ± 0.042
1.08	0.835 ± 0.047
1.12	0.53 ± 0.12
1.16	0.544 ± 0.097
1.20	0.510 ± 0.056
1.24	0.538 ± 0.003
1.28	0.498 ± 0.003
1.32	0.446 ± 0.003
1.36	0.421 ± 0.003
1.40	0.378 ± 0.003
1.44	0.356 ± 0.002
1.48	0.295 ± 0.002
1.52	0.242 ± 0.038
1.56	0.111 ± 0.028

Table C.2: Invariant cross sections as a function of momentum at 20° from the present results.

Momentum (GeV/c)	(p–like cross sections ± Statistical Error)$\times 10^5$
0.60	1.074 ± 0.074
0.68	0.804 ± 0.055
0.76	0.599 ± 0.042
0.84	0.465 ± 0.034
0.92	0.351 ± 0.027
1.00	0.218 ± 0.018
1.08	0.128 ± 0.011
1.16	0.101 ± 0.010
1.24	0.068 ± 0.007
1.32	0.050 ± 0.006
1.40	0.0364 ± 0.005
1.48	0.0214 ± 0.003
1.56	0.0169 ± 0.004
1.64	0.0098 ± 0.0022
1.72	0.0055 ± 0.0018
1.80	0.0016 ± 0.0006
1.88	0.0025 ± 0.0011

Table C.3: Invariant cross sections as a function of momentum at 40° from the present results.

Momentum (GeV/c)	(p–like cross sections ± Statistical Error)×10^4
0.60	3.92 ± 0.19
0.68	2.59 ± 0.13
0.76	1.638 ± 0.089
0.84	1.032 ± 0.064
0.92	0.630 ± 0.042
1.00	0.379 ± 0.030
1.08	0.229 ± 0.022
1.16	0.127 ± 0.014
1.24	0.075 ± 0.010
1.32	0.043 ± 0.008
1.40	0.017 ± 0.003
1.48	0.011 ± 0.003

Table C.4: Invariant cross sections as a function of momentum at 60° from the present results.

Momentum (GeV/c)	(p–like cross sections ± Statistical Error) $\times 10^5$
0.52	2.39 ± 0.14
0.60	1.97 ± 0.14
0.68	1.77 ± 0.14
0.76	1.46 ± 0.13
0.84	1.31 ± 0.13
0.92	1.12 ± 0.11
1.00	0.92 ± 0.11
1.08	0.783 ± 0.093
1.16	0.627 ± 0.079
1.24	0.481 ± 0.065
1.32	0.390 ± 0.055
1.40	0.279 ± 0.043
1.48	0.204 ± 0.032
1.56	0.144 ± 0.023
1.64	0.101 ± 0.017
1.72	0.075 ± 0.013
1.80	0.0456 ± 0.0080
1.88	0.0315 ± 0.0056
1.96	0.0238 ± 0.0044

Table C.5: Invariant cross sections as a function of momentum at 20° from the Hayashi data.

Momentum (GeV/c)	(p–like cross sections ± Statistical Error) $\times 10^5$
0.52	1.56 ± 0.11
0.60	1.136 ± 0.093
0.68	0.843 ± 0.079
0.76	0.613 ± 0.064
0.84	0.469 ± 0.054
0.92	0.343 ± 0.042
1.00	0.249 ± 0.032
1.08	0.160 ± 0.022
1.16	0.107 ± 0.016
1.24	0.069 ± 0.011
1.32	0.0488 ± 0.0077
1.40	0.0276 ± 0.0046
1.48	0.0169 ± 0.0029
1.56	0.0093 ± 0.0017
1.64	0.0061 ± 0.0012
1.72	0.0042 ± 0.0008
1.80	0.0025 ± 0.0005
1.88	0.0012 ± 0.0003
1.96	0.0006 ± 0.0002

Table C.6: Invariant cross sections as a function of momentum at 40° from the Hayashi data.

Momentum (GeV/c)	(p–like cross sections ± Statistical Error) $\times 10^4$
0.52	8.19 ± 0.65
0.60	5.17 ± 0.48
0.68	3.16 ± 0.33
0.76	1.95 ± 0.22
0.84	1.28 ± 0.16
0.92	0.730 ± 0.099
1.00	0.442 ± 0.063
1.08	0.236 ± 0.036
1.16	0.141 ± 0.023
1.24	0.064 ± 0.011
1.32	0.0336 ± 0.0059
1.40	0.0179 ± 0.0034
1.48	0.0057 ± 0.0013
1.56	0.0050 ± 0.0012
1.64	0.0023 ± 0.0007
1.72	0.0012 ± 0.0005
1.80	0.0007 ± 0.0004

Table C.7: Invariant cross sections as a function of momentum at 60° from the Hayashi data.

Momentum (GeV/c)	(p–like cross sections ± Statistical Error) $\times 10^5$
0.44	2.61 ± 0.25
0.52	2.40 ± 0.20
0.60	1.82 ± 0.14
0.68	2.01 ± 0.15
0.76	1.95 ± 0.13
0.84	2.00 ± 0.12
0.92	1.86 ± 0.11
1.00	2.14 ± 0.11
1.08	2.01 ± 0.11
1.16	1.800 ± 0.093
1.24	1.435 ± 0.081
1.32	1.123 ± 0.070
1.40	0.926 ± 0.061
1.48	0.751 ± 0.054
1.56	0.525 ± 0.044
1.64	0.336 ± 0.035
1.72	0.221 ± 0.027
1.80	0.137 ± 0.019
1.88	0.083 ± 0.014
1.96	0.051 ± 0.011

Table C.8: Invariant cross sections as a function of momentum at 15° from VUU calculations.

Momentum (GeV/c)	(p–like cross sections ± Statistical Error $\times 10^5$
0.44	2.49 ± 0.21
0.52	2.21 ± 0.19
0.60	1.67 ± 0.12
0.68	1.90 ± 0.12
0.76	1.56 ± 0.10
0.84	1.643 ± 0.095
0.92	1.537 ± 0.087
1.00	1.215 ± 0.073
1.08	1.220 ± 0.071
1.16	0.950 ± 0.057
1.24	0.826 ± 0.052
1.32	0.606 ± 0.045
1.40	0.454 ± 0.037
1.48	0.304 ± 0.027
1.56	0.210 ± 0.023
1.64	0.146 ± 0.017
1.72	0.099 ± 0.015
1.80	0.074 ± 0.012
1.88	0.0464 ± 0.0091
1.96	0.0215 ± 0.0057

Table C.9: Invariant cross sections as a function of momentum at 20° from VUU calculations.

Momentum (GeV/c)	(p–like cross sections ± Statistical Error) $\times 10^5$
0.44	1.74 ± 0.13
0.52	1.422 ± 0.096
0.60	1.158 ± 0.077
0.68	0.851 ± 0.059
0.76	0.628 ± 0.046
0.84	0.490 ± 0.037
0.92	0.312 ± 0.025
1.00	0.263 ± 0.024
1.08	0.175± 0.018
1.16	0.120 ± 0.015
1.24	0.0609 ± 0.0076
1.32	0.0539 ± 0.0085
1.40	0.0350 ± 0.0065
1.48	0.0204 ± 0.0046
1.56	0.0097 ± 0.0026
1.64	0.0105 ± 0.0036
1.72	0.0050 ± 0.0021
1.80	0.0020 ± 0.0010
1.88	0.0035 ± 0.0012
1.96	0.0002 ± 0.0002

Table C.10: Invariant cross sections as a function of momentum at 40° from VUU calculations.

Momentum (GeV/c)	(p–like cross sections ± Statistical Error) $\times 10^5$
0.44	1.056 ± 0.088
0.52	0.665 ± 0.061
0.60	0.451 ± 0.042
0.68	0.328 ± 0.032
0.76	0.200 ± 0.022
0.84	0.078 ± 0.011
0.92	0.074 ± 0.011
1.00	0.0460 ± 0.0077
1.08	0.0196 ± 0.0031
1.16	0.0188 ± 0.0050
1.24	0.0082 ± 0.0028
1.32	0.0020 ± 0.0007
1.40	0.0032 ± 0.0010
1.48	0.0004 ± 0.0004

Table C.11: Invariant cross sections as a function of momentum at 60° from VUU calculations.

LIST OF REFERENCES

[Aich89] J. Aichelin, J. Cugnon, Z. Fraenkel, K. Frankel, C. Gale, M. Gyulassy, D. Keane, C. Ko, J. Randrup, A. Rosenhauer, H. Stocker, G. Welke, and J. Wu, Phys. Rev. Lett. **62**, 1461 (1989).

[Banf68] A. Banford, The Transport of Charged Particle Beams, E. & F. N. Spon Ltd., London, 1966.

[Batk92] G. Batko, private discussions.

[Bert88] G. Bertsch, S. Das Gupta, Phys. Rep. **160**, 189 (1988).

[Brun86] R. Brun, F. Bruyant, M. Maire, A. McPherson, and P. Zanarini, GEANT3, CERN Report No. DD/EE/841 (unpublished) (1986).

[Butl63] S. Butler, C. Pearson Phys. Rev. **129**, 836 (1963).

[Cass90] W. Cassing, V. Metag, U. Mosel, K. Niita, Phys. Rep., 188, 363 (1990).

[Fano63] U. Fano, Ann. Rev. Nuc. Sci., **13**, 1 (1963).

[Good60] T. Gooding, H. Pugh, Nucl. Inst. and Methods 7, 189 (1960).

[Grif87] D. Griffiths, Introduction to Elementary Particles, John Wiley & Son Inc., New York, 1987.

[Gutb76] H. Gutbrod, A. Sandoval, P. Johansen, A. Postkanser, J. Gosset, W. Meyer, G. Westfall, and R. Stock, Phys. Rev. Lett. **37**, 667 (1976).

[Harr81] J. Harrison, T. Kozlowski, R. Floyd, J. Amann, G. Anderson, M. Oothout, and D. Perry, I. E. E. E. Transactions on Nuclear Science **NS-28**, 3724 (1981).

[Haya88] S. Hayashi, Y. Miake, T. Nagae, S. Nagamiya, H. Hamagaki, O. Hashimoto, Y. Shida, I. Tanihata, K. Kimura, O. Yamakawa, T. Kobayashi, and X. Bai, Phys. Rev. C **38**, 1229 (1988).

[Jian91] J. Jiang, D. Keane, J. Cogar, G. Fai, S. Hayashi, C. Hartnack, and H. Stocker, Phys. Rev. C **45**, 2353 (1991).

[Jaca85] B. Jacak, D. Fox, and G. Westfall, Phys. Rev. C **31**, 704 (1985).

[Koon86] S. Koonin, Computational Physics, Benjamin/Cummings Pub. Co., Menlo Park, 1986.

[Lema79] M. Lemaire, S. Nagamiya, S. Schentzer, H. Steiner, and I. Tanihata, Phys. Lett. **85B**, 38 (1979).

[Naga81] S. Nagamiya, M. Lemaire, E. Moeller, S. Schentzer, G. Shapiro, H. Steiner, and I. Tanihata, Phys. Rev. C **24**, 971 (1981).

[Part92] Particle Data Group, Phys. Rev. D **45**, III14 (1992).

[Schw63] A. Schwarzschild, C. Zupancic, Phys. Rev. **129**, 854 (1963).

[Wind83] H. Wind, Formulae and Methods in Experimental Data Evaluation, European Physical Society, Geneva, 1983.

[Zajc82] W. Zajc, Ph.D Thesis, The University of California, Berkeley (1982), LBL-14864, (unpublished).